DOKUZ EYLÜL UNIVERSITY

GRADUATE SCHOOL OF NATURAL AND APPLIED SCIENCES

COMPARISON OF KINEMATIC ANALYSIS RESULTS OBTAINED FROM UNMANNED AERIAL VEHICLE DATA AND SCAN-LINE DISCONTINUITY MEASUREMENTS IN THE GNEISS ROCK SLOPES

by

Melikhan KARAKAŞ

August, 2021

İZMİR

COMPARISON OF KINEMATIC ANALYSIS RESULTS OBTAINED FROM UNMANNED AERIAL VEHICLE DATA AND SCAN-LINE DISCONTINUITY MEASUREMENTS IN THE GNEISS ROCK SLOPES

A Thesis Submitted to the
Graduate School of Natural and Applied Sciences of Dokuz Eylül University
In Partial Fulfillment of the Requirements for the Degree of Master of Science
in Geological Engineering, Applied Geology Program

by

Melikhan KARAKAŞ

August, 2021

İZMİR

M.Sc THESIS EXAMINATION RESULT FORM

We have read the thesis entitled **"COMPARISON OF KINEMATIC ANALYSIS RESULTS OBTAINED FROM UNMANNED AERIAL VEHICLE DATA AND SCAN-LINE DISCONTINUITY MEASUREMENTS IN THE GNEISS ROCK SLOPES"** completed by **MELİKHAN KARAKAŞ** under supervision of **ASSOC. PROF. DR. CEM KINCAL** and we certify that in our opinion it is fully adequate, in scope and in quality, as a thesis for the degree of Master of Science.

…….

Assoc. Prof. Dr. Cem KINCAL

Supervisor

……..

Prof. Dr. Ali Bahadır YAVUZ

Jury Member

.....……

Assoc. Prof. Dr. Alper SEZER

Jury Member

Prof. Dr. Özgür ÖZÇELİK

Director

Graduate School of Natural and Applied Sciences

ACKNOWLEDGEMENT

I would like to thank my esteemed professor, Associate Professor Dr. Cem KINCAL, who helped me work in engineering geology and remote sensing and contributed to this study with his consultancy.

Within the scope of field studies; I would like to thank S. Deniz KARAGÖZ, M.Sc. Geology Engineer, who helped in many areas such as transportation, work permits, equipment support and shared his knowledge and experience.

I would like to thank "Sibelco Turkey Madencilik Sanayi ve Ticaret A.Ş" for sharing this open-source data and supporting the studies within the scope of this thesis.

I would like to thank Prof. Dr. M Yalçın Koca, Dr Tümay Kadakçı KOCA and Lecturer Semih ESKİ, who made valuable contributions to the study with their opinions, advice and resource assistance throughout this study, and to my family and friends who did not withhold their financial and moral support during my study.

I would like to thank MKA GEOPHYSIC company for providing the opportunity to use the Unmanned Aerial Vehicle within the scope of this thesis.

I would like to thank my friend Enes KALHAN, who helped me during my undergraduate education between 2015-2019 and graduate education between 2019-2021 and added value to my studies.

I would like to thank my dear family and my professors in the Department of Geological Engineering, who have always supported me financially and morally throughout my education life.

Melikhan KARAKAŞ

COMPARISON OF KINEMATIC ANALYSIS RESULTS OBTAINED FROM UNMANNED AERIAL VEHICLE DATA AND SCAN-LINE DISCONTINUITY MEASUREMENTS IN THE GNEISS ROCK SLOPES

ABSTRACT

Slope failures due to mass movements can cause occupational accidents and result in loss of life and property. In order to prevent these possible accidents, the slopes should be designed to remain safe for both the continuity of production and work safety. As in all open pit mines, these slopes should be designed as vertical as possible for the economic continuity of the enterprises. However, high angle slopes designed in this way carry a considerable risk in terms of mass movements and slope failures. In this case, some engineering geology studies are required to determine the safest possible slope angle. Discontinuity-controlled slope failures occurred in this albite (feldspar) quarry, which was opened in the gneisses in the Menderes Massif and produced by the open pit mining method. In these rock slopes located in the gneiss unit, it has been determined that in addition to the discontinuities formed by the effect of tectonism, foliation planes also cause planar sliding failures. The number of wedge type failures is quite high due to the presence of many discontinuity sets overlapping each other in the study area, and it has also been determined that toppling type failures are dominant due to the high angle of these discontinuities. Activities such as production, excavation and blasting in the eastern part of this mine, where slope instabilities are more dominant, were stopped by the company's authorized engineer. With these studies, the mass movements in the eastern part of the albite quarry were classified and the regions where these movements were intense were determined. 140 observations were made in 10 stages in total. Unmanned Aerial Vehicle has been used in areas where discontinuity measurement cannot be made in terms of speeding field work and occupational safety in this mine where the working area is so large and the number of discontinuities is high.

Keywords: Albite, Gneiss, mass movements, Menderes Massif, open pit, unmanned aerial vehicle

GNAYS KAYA ŞEVLERİNDEKİ HAT ETÜDÜ ÖLÇÜMLERİYLE İNSANSIZ HAVA ARACI VERİLERİNİN KİNEMATİK ANALİZLERİNİN KARŞILAŞTIRILMASI

ÖZ

Kütle hareketlerine bağlı meydana gelen şev yenilmeleri iş kazalarına sebep olup can ve mal kayıpları ile sonuçlanabilir. Bu olası kazaların önüne geçmek için hem üretimin devamlılığı hem de iş güvenliği için şevlerin güvenli kalacak biçimde tasarlanması gerekir. Bütün açık ocak işletmelerinde olduğu gibi, işletmelerin ekonomik devamlılığı için bu şevlerin mümkün mertebe dik olarak tasarlanması gereklidir. Ancak, böyle tasarlanan yüksek açılı şevlerde kütle hareketleri ve şev yenilmeleri açısından oldukça risk taşımaktadır. Bu durumda olabilecek en güvenli şev açısını belirlemek için bazı mühendislik jeolojisi çalışmaları gereklidir. Menderese Masifi'ndeki gnayslarda açılmış, açık ocak işletme yöntemiyle üretim yapılan bu albit (feldspat) ocağında süreksizlik kontrollü şev yenilmeleri meydana gelmiştir. Gnays biriminde yer alan bu kaya şevlerinde, tektonizma etkisi ile oluşmuş süreksizliklerin yanı sıra foliasyon düzlemleri de düzlemsel kayma yenilmelerine sebebiyet verdiği belirlenmiştir. Çalışma bölgesinde birbiri ile kesişen birçok süreksizlik takımının bulunması nedeni ile kama türü yenilmelerin sayısı oldukça fazladır ve aynı zamanda bu süreksizliklerin yüksek açılı olmasından dolayı devrilme tipi yenilmelerin baskın olduğu belirlenmiştir. Bu madenin şev duraysızlıklarının daha baskın olduğu doğu kısmındaki üretim, kazı ve patlatma gibi faaliyetler şirketin yetkili mühendisi tarafından durdurulmuştur. Üretime ara verilen bu dönemde, albit ocağının doğu kısmında bir dizi mühendislik jeolojisi çalışmaları yapılmıştır. Yapılan bu çalışmalarla albit ocağının doğu kısmındaki kütle hareketleri kinematik analiz tekniği ile belirlenip sınıflandırılmış ve bu hareketlerin yoğun olduğu bölgeler belirlenmiştir. Toplam 10 kademede 140 adet gözlem yapılmıştır. Çalışma sahasının bu denli büyük olması ve süreksizliklerin sayıca fazla olduğu bu ocakta saha çalışmalarını hızlandırmak ve iş güvenliği açısından süreksizlik ölçümü yapılamayan bölgelerde İnsansız Hava Aracı kullanılmıştır.

Anahtar kelimeler: Albit, gnays, kütle hareketleri, Menderes Masifi, açık ocak, insansız hava aracı

CONTENTS

Page

M.Sc THESIS EXAMINATION RESULT FORM ii

ACKNOWLEDGEMENT iii

ABSTRACT iv

ÖZ v

LIST OF FIGURES ix

LIST OF TABLES xiii

CHAPTER ONE - INTRODUCTION 1

1.1 Purpose And Scope 1

CHAPTER TWO - WORKING AREA 3

2.1 Business Location and Transportation 3

2.2 Mining Activities 3

2.3 Geology 4

2.4 Geomorphology 4

2.5 Climate 6

CHAPTER THREE - STRUCTURAL GEOLOGY 7

3.1 Foliation Planes 9

3.2 Joints 12

CHAPTER FOUR - ENGINEERING GEOLOGY 14

4.1 Properties of Discontinuities 16
4.2 Orientation of Discontinuities 16
4.3 Aperture of Discontinuities and Filling Material Condition 16
4.4 Roughness and Waviness of Discontinuity Planes 19
4.5 Water Condition on Discontinuity Surfaces 21
4.6 Frequency of Discontinuities 22
4.7 Persistence of Discontinuities 23
4.8 Strength of Discontinuity Walls 24
4.9 Ground-Water 27
4.10 Drillhole Data and İnclonometer Surveying 28

CHAPTER FIVE - WEATHERING AND ALTERATION 35

5.1 Weathering Status 36
5.2 Alteration 38

CHAPTER SIX - SLOPE STABILITY ASSESSMENTS 42

6.1 Kinematic Analysis 42
6.1.2 Planar Sliding Failure 45
6.1.2.1 Planar slidings caused by foliation planes 45
6.1.2.2 Planar sliding caused by discontinuities (joints) 48
6.1.3 Wedge Type Sliding Failure 50
6.1.4 Toppling Type Failure 55
6.1.4.1 Flexural Toppling 58
6.1.4.2 Direct Toppling 60

CHAPTER SEVEN - REMOTE SENSING 64

7.1 UAV Survey 64
7.1.1 Photogrammetry and Process 65
7.1.2 Kinematic Analysis 72

7.1.2.1 Planar Sliding Failure 73
7.1.2.2 Wedge Type Sliding Failure 75
7.1.2.3 Toppling Type Failure 76
7.2 GIS Applications 77

CHAPTER EIGHT - ASSESSMENTS 80

CHAPTER NINE - CONCLUSIONS AND RECOMMENDATIONS 83

REFERENCES 86

APPENDICES 90

LIST OF FIGURES

Page

Figure 2.1 Location map of the study area (Frame with red arrow) 3
Figure 2.2 Old topography of the study area and stream beds (Bottom transparent layer; current Google Eart image) 5
Figure 2.3 Annual Temperature-Precipitation Chart of Aydın Province 6
Figure 3.1 The structural elements 7
Figure 3.2 Displacement of the 70/040 oriented quartz vein at the observation point 52 in the study area 8
Figure 3.3 Active faults around the working area 9
Figure 3.4 The field view of foliation planes that change (folds) due to deformation 10
Figure 3.5 Foliation planes forming a planar sliding mechanism and causing sliding 11
Figure 3.6 Rose diagram of the foliation planes observed in the open pit (A), the angular distribution graph of the dip angles of the foliation planes (B), the angular distribution graph of the dip directions of the foliation planes (C) 11
Figure 3.7 Contour diagram and rose diagram of all discontinuity (1820 pc.) measurements obtained 13
Figure 4.1 Engineering geology map of the study area 14
Figure 4.2 Slope geometry of Open Pit 15
Figure 4.3 The effect of filling material thickness on shear strength 17
Figure 4.4 Weathering product filling material observed between discontinuity walls on slopes near weathering zones 18
Figure 4.5 Discontinuity planes with different apertures observed in slopes at different investigatşon locations 19
Figure 4.6 Roughness comb measurement on the discontinuity plane 20
Figure 4.7 Roughness in slopes; (A) Slightly rough surface, (B) Very rough surface 20
Figure 4.8 Seepage point seen on the slope at the observation location 116 at 470 m elevation 21

Figure 4.9 Varying distances between discontinuity walls on slopes at different observation points 22
Figure 4.10 Persistence of discontinuities on different slopes; (A) Discontinuities with approximately 1-3 meters of persistence, (B) Discontinuities with approximately 5-10 meters of persistence. (Slope height: ~10m) 23
Figure 4.11 L-Type Schmidt hammer test on slopes 24
Figure 4.12 Histogram graph of UCS Values 25
Figure 4.13 Thematic map of UCS Values created using the IDW method 26
Figure 4.14 Overlaying the thematic map of the interpolated UCS values on the 3D model 27
Figure 4.15 The inclonometer hole located at 540 elevation in an open pit and its survey 28
Figure 4.16 Stress crack and failed zone located in front of the inclonometer well .. 29
Figure 4.17 Anomaly observed between 14.12.2020 and 29.01.2021 between approximately 28 and 31 meters 30
Figure 4.18 The probable sliding circle drawn between the stress cracks observed between the 540th and 512th elev, based on the drilling and inclinometer data 32
Figure 4.19 The probable sliding circle drawn between the stress cracks observed between the 540th and 512th elev, based on the drilling and inclinometer data 34
Figure 5.1 Map of the study area showing the weathering zones and block debris... 35
Figure 5.2 The weathering and loss of rock feature observed on the slope at the 111th Observation Point 36
Figure 5.3 Block debris due to weathering seen at observation points 47 and 101 ... 37
Figure 5.4 Dendritic traces formed by the hydrothermal fluid located in the alteration zone and exposed due to faulting 38
Figure 5.5 Rock slopes with oxidized surfaces 39
Figure 5.6 Oxide zones seen from angled aerial photographs 40
Figure 6.1 Presentation of kinematic analysis results in pie chart format 43

Figure 6.2 Thematic map of planar sliding failures determined by the kinematic analysis technique in the study area and the factors caused by these failures. 46
Figure 6.3 Planar sliding failure caused by foliation planes; (A) Field view, (B) Kinematic analysis (Lower hemisphere). 47
Figure 6.4 Graph showing the angular distribution of the orientation of foliation planes causing planar sliding 48
Figure 6.5 Planar sliding failure caused by joints; (A) The view of the sliding in the field and the direction of the sliding, (B) The block and sliding plane that is likely to sliding, (C) Kinematic analysis of the planar failure..... 49
Figure 6.6 Graph showing the angular distribution of the orientation of discontinuity planes (joints) causing planar sliding 50
Figure 6.7 The safety factor calculated using the analytical method of wedge-type failures, their stability and their relationship with old stream beds..... 52
Figure 6.8 Wedge type sliding failure, (A) View of planes forming the wedge in the field, (B) Kinematic analysis of wedge type sliding failure 53
Figure 6.9 Kinematic analysis of wedge type sliding using all planes forming the wedge and mean slope orientation..... 55
Figure 6.10 Generally the directions of high persistence and high angle discontinuity planes that caused toppling failures 56
Figure 6.11 Distribution of types of toppling failure in the working area 57
Figure 6.12 Flexural toppling failure; (A) High angle discontinuities and possible toppling blocks in the field view, (B) Kinematic analysis of flexural toppling failure..... 59
Figure 6.13 Direct toppling field view; (A) High angle discontinuity planes, (B) Sets of discontinuities perpendicular to each other (front view of A) 60
Figure 6.14 Direct toppling type failure; (A) Blocks formed by sets of joints perpendicular to each other, (B) Kinematic analysis of direct (block) toppling type failure..... 61
Figure 6.15 Angular scatter plot of discontinuity planes that cause toppling failures63
Figure 7.1 Flight plan of the worksite in the GS RTK app on the Phantom 4 RTK's onboard display controller..... 64

Figure 7.2 The "Dense Point Cloud" data model with 144,786,888 points and its detailing 68
Figure 7.3 Textured mesh model created with 7,000,000 triangles and details from close-up view 69
Figure 7.4 Digital elevation models (DEM) presented with different color palettes . 70
Figure 7.5 Proof of true orthophoto and digital elevation model fit on Google Satellite Hybrid image and positional accuracy 71
Figure 7.6 Planar sliding failure by remote sensing; (A) Foliation plane orientation, (B) Slope orientation (C) Kinematic analysis of planar sliding 74
Figure 7.7 Wedge sliding failure with remote sensing; (A) Orientation of planes in the wedge block, (B) Orientation of the slope, (C) Kinematic analysis of wedge-type sliding 75
Figure 7.8 Toppling type failure (Flexural Toppling) with remote sensing; (A) Orientation of planes, (B) Orientation of the slope, (C) Kinematic analysis of flexural toppling type failure 77
Figure 7.9 Concentrations of mass movements detected in the eastern part of Open Pit, produced using the heat map (Kernel Density) technique 79
Figure 7.10 The difference seen in the region where the production and excavation activities continue, according to the topographic cross-sections taken from the DEM obtained from the flights on the first and last day 81
Figure 7.11Topographical cross-sections taken from the regions where mass movements are concentrated by means of the Digital Elevation Model . 81

LIST OF TABLES

Page

Table 3.1 Results found by different researchers working in the same region……12
Table 3.2 Angular distributions of discontinuity sets……..12
Table 4.1 The rebound numbers at some observation points and the UCS values obtained using Equation 1…….26
Table 4.2 Consistency of open pit drilling with geotechnical log results and anomaly range in inclonometer (indicated in red)……31
Table 5.1 The results of the Schmidt hammer test on the altered slopes at the observation locations……..41
Table 6.1 Kinematic analysis results (-: Discontinuity measurement could not be taken for various reasons., K.Stable: Kinematically stable slopes., P:Planar Failure., W:Wedge Failure., FT:Flexural Toppling., DT:Direct Toppling)……44
Table 6.2 K factor and FoS calculated using Equation 1……51
Table 7.1 Parameters and details used in measurements made with the Phantom 4 RTK …….65
Table 7.2 GCPs accuracy……67
Table 7.3 Details of data generated during and/or after the photogrammetric process……67
Table 7.4 Comparison of slope orientations measured with Brunton type geologist compass and Cloudcompare program Compass plugin……..73

CHAPTER ONE

INTRODUCTION

1.1 Purpose and Scope

In order to the production in the mining sector to proceed smoothly and economically, some parameters must be taken into account. One of the parameters that should be considered is the issues that may cause possible work accidents such as slidings, landslides or slope stability problems due to geological, geomechanically and geotechnical parameters in the mining quarry. In order to prevent these accidents, the stability of the slopes in the production quarry should be evaluated and examined in detail and an economical solution should be reached. Therefore, a series of field studies should be carried out for the design of the slopes in the production quarry and for the evaluations. For these field researches and observations, the use of many software and hardware has become almost mandatory in terms of both time and economic solutions with the technology that has developed out of the classical methods. Production activities, which were disrupted in the eastern part of the albite quarry due to slope instability, were completely stopped by the authorized engineer of the company at the end of 2019 and possible work accidents were prevented. It was aimed to evaluate the stability of this mine with the engineering geology studies carried out in this period when production was suspended. In this open pit mine opened in the gneisses in the Menderes Massif, the weakening of the rock mass due to weathering effects, the planar sliding mechanisms due to the foliation planes in the gneiss unit being parallel to the slope surface, the weakening of the rock mass due to the presence of many buried stream beds and their branches, and the Yarenalan Fault in the region. Many geological factors such as the fault have created stability problems. At the same time, in addition to the discontinuities and joint sets formed by the tectonic factors that occurred previously in the region, controlled blasting for production increased the number of discontinuities in the quarry. Within the scope of this thesis, potential mass movements in 10 benches were determined with the kinematic analysis technique performed in the first stage to make slope stability evaluations in the Albit Quarry. The orientations of the discontinuity planes and slopes required for the kinematic analysis were measured with the classical method, the geologist compass, and then compared with the point

cloud data created using the UAV. At the same time, as in this study area, in problematic areas where measurements cannot be taken in terms of occupational safety, using this method has increased the research efficiency and increased the number of data available, allowing for more detailed analysis. After the mass movements were determined and classified at these inspection points made at 141 points, they were visualized with GIS programs. These classification and visualization processes are intended to provide a guide to the authorized persons of this open pit mine.

CHAPTER TWO

WORKING AREA

2.1 Business Location and Transportation

The Albit Quarry is located approximately 25km southwest of the Cine district of Aydın province (Figure 2.1). Aydın is located within the borders of 1:25,000 scale topographic map with sheet number N19-b1 and is approximately 40 km away from Aydın city center. The closest settlement to the quarry is Karpuzlu district, which is the smallest district of the Aegean Region and is connected to Aydın Province.

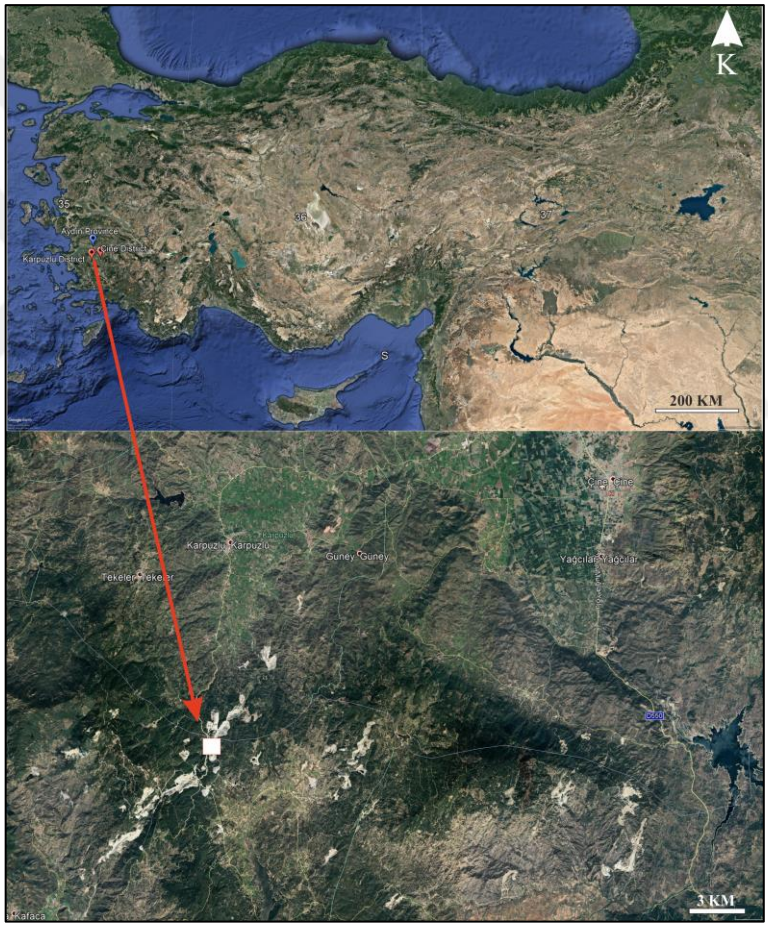

Figure 2.1 Location map of the study area (Frame with red arrow)

2.2 Mining Activities

The subject of the thesis is feldspar (albite) quarries, which are opened in the Çine Sub-massif and produce with the open pit operation method, and these quarries have

been operated since 1995. With the increasing production figures over the years, 250.000-300.000 tons of ore is produced.

2.3 Geology

The study area is located within the Menderes Massif formation, which is one of the tectonic zones of the Anatolides outcropping in Western Anatolia. This open pit mine in the study area is located within the meshed leucocratic (felsic) gneisses called the core series in the Çine Sub-massif within the Menderes Massif (Karagöz, et al., 2016). These leucocratic gneisses, which are light colored due to their low ferromagnesian mineral content, form the main lithological unit of this quarry. The sub massive is represented by coarse-grained gneiss and fine-grained mica-rich orthogneisses (Kadakçı Koca, et al, 2014). Mineralogically, the Na-feldspar composition ore zone has developed along the NE-SW shear zone (Karadere Shear Zone) in the quarry. Bounded by the probable Quaternary fault to the northeast and the Holocene fault to the southwest, this mine appears to contain gneiss as an ore body and wall rock. The direction of the ore deposit is in the direction of 55-60/117 with a length of approximately 650-660 m, which develops along the shear zone in the mine (Koca, et al., 2020). NE-SW extension shear zones, which are formed due to the extensional tectonics in the NNE-SSW direction affecting the Aegean Region, are observed in the Menderes Massif as common geological structures (Şengör, 1987; Candan et al., 2005).

2.4 Geomorphology

The study area is located on a passageway between two hills approaching 570 m at their highest point, and the altitude varies between 408-550 m. The previous topography of the study area (1959) is in the form of a valley at 430-580 m elevations. The contour lines produced from the N19-b1 sheet of the region and the previously found stream beds are shown in the map in Figure 2.2.

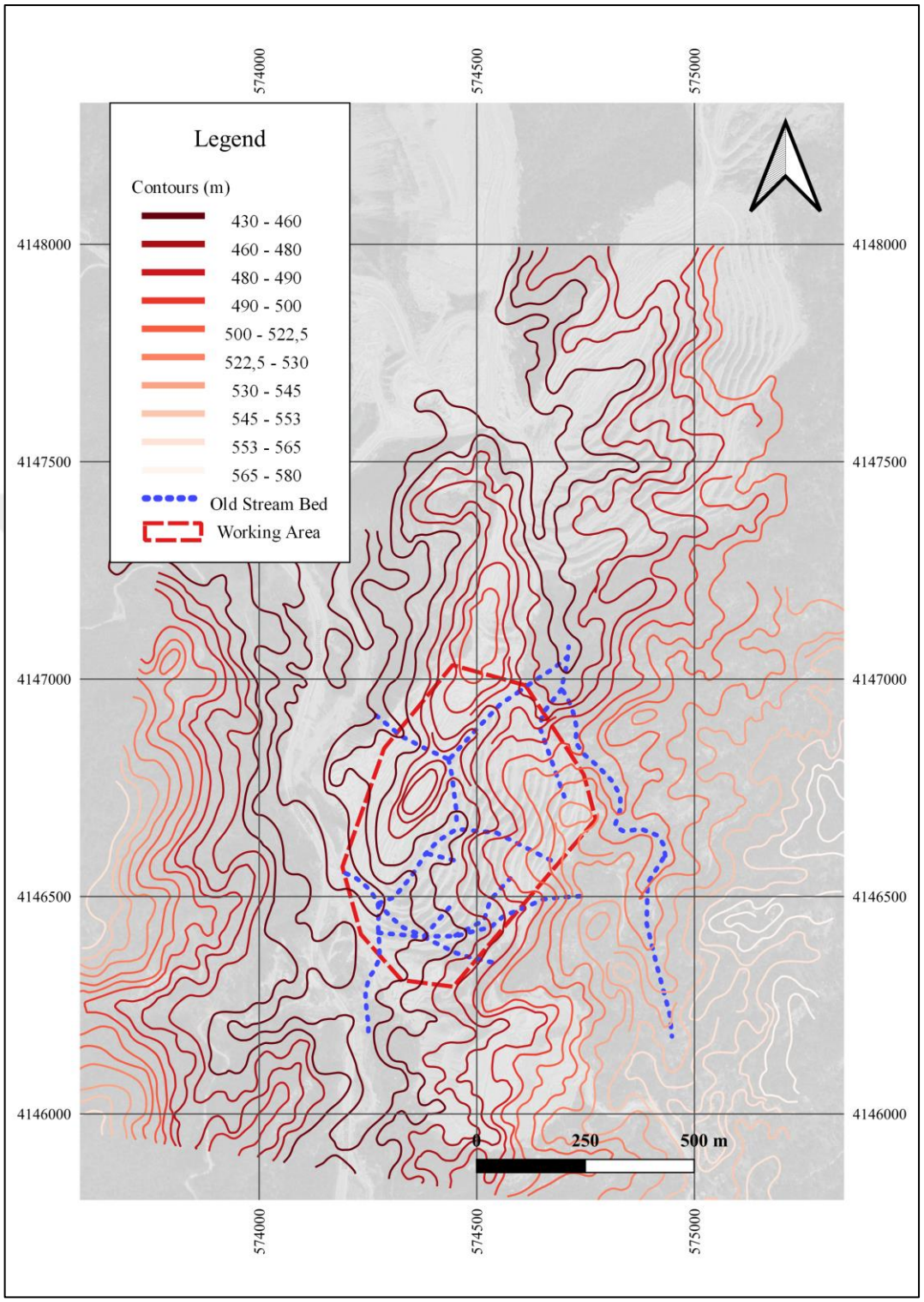

Figure 2.2 Old topography of the study area and stream beds (Bottom transparent layer; current Google Earth image)

2.5 Climate

The Mediterranean climate, which is hot in the summer months and warm and very rainy in the winter months, is effective in the region (Figure 2.3). Due to the topographic structure in this climate type, two different types of plants have been formed in and around Aydın province. These are vegetation in maquis and forest types. Due to the climatic effect in the region, snowfalls are rarely seen. According to the data of the General Directorate of Meteorology and the Ministry of Forestry and Water Affairs, the prevailing wind direction of Aydın in the region is East, and depending on seasonal changes, the secondary prevailing wind direction is west-Northwest. The fact that the region receives excessive precipitation during the winter months has adversely affected the rock units in the study area in terms of weathering and caused stabilization problems. The effect of precipitation on weathering is explained in detail in Chapter 5.

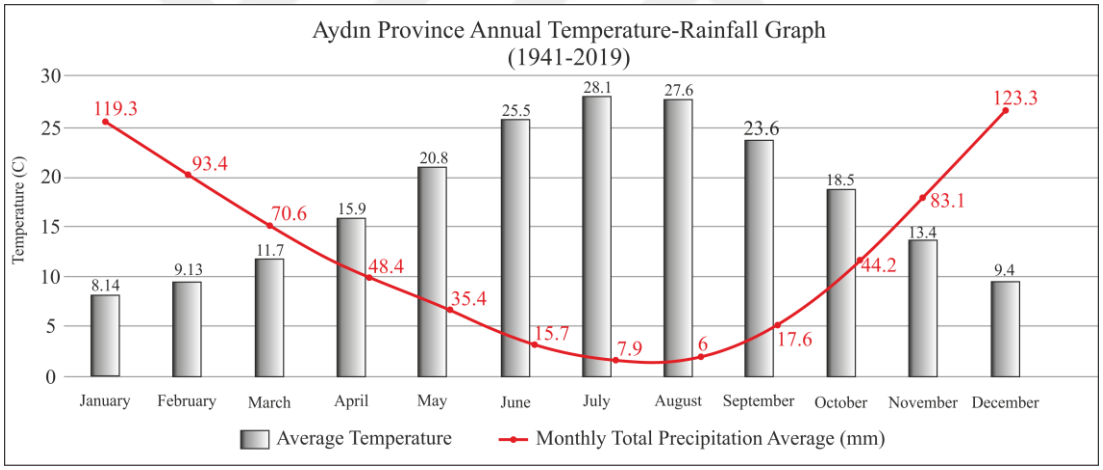

Figure 2.3 Annual Temperature-Precipitation Chart of Aydın Province

CHAPTER THREE

STRUCTURAL GEOLOGY

It is extremely important for slope stability design to examine and evaluate these structural elements in detail, since failures in the study area are discontinuity-controlled. For this reason, the structural elements in the study area have been carefully studied in detail. Detailed explanations of the discontinuity measurements are given in Chapter 4. Apart from the Yarenalan Fault (70/336; Koca et al., 2020) in the study area, structural factors such as the probable Quaternary fault located approximately 18 km northeast of the enterprise and the Holocene fault located 16 km southwest of the open pit indicate that this open pit is also under the influence. (MTA, 2021) (Figure 3.3). (Uygun & Gümüşçü 2000) in their study on albite deposits stated in their maps that there are factors such as shear zone, fault and main fracture near the study area. These structural elements are shown in Figure 3.1. At the same time, the presence of these structural factors can clearly show the displacements due to the small-scale shear (faulting) zone in the study area where it controls the study area (Figure 3.2).

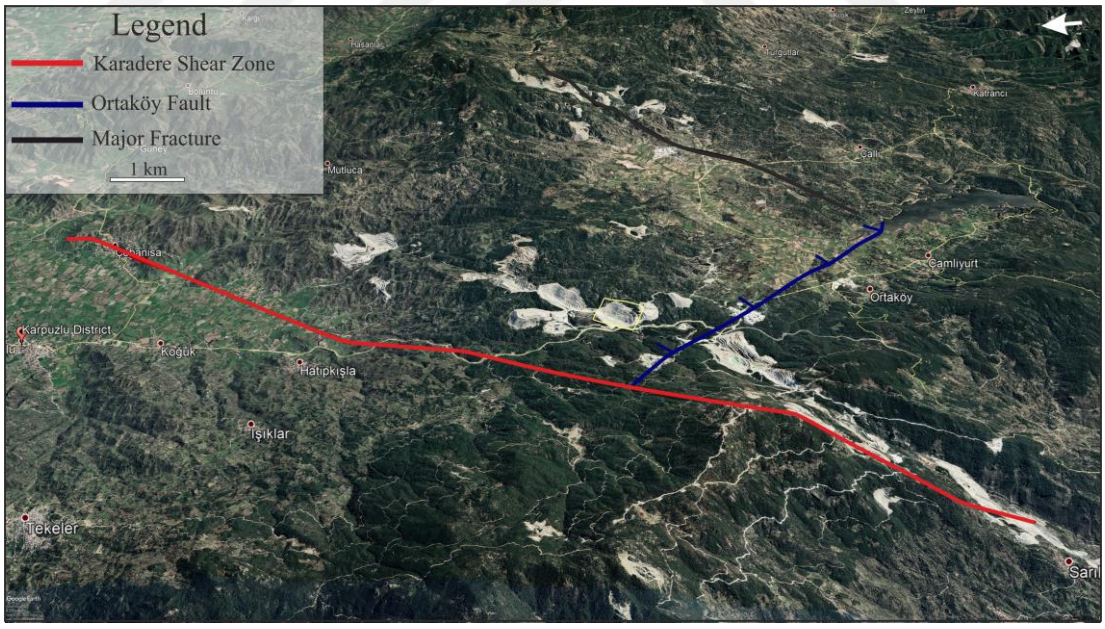

Figure 3.1 The structural elements found in the work of (Uygun & Gümüşçü, 2000)

Figure 3.2 Displacement of the 70/040 oriented quartz vein at the observation point 52 in the study area (Personal archive, 2021)

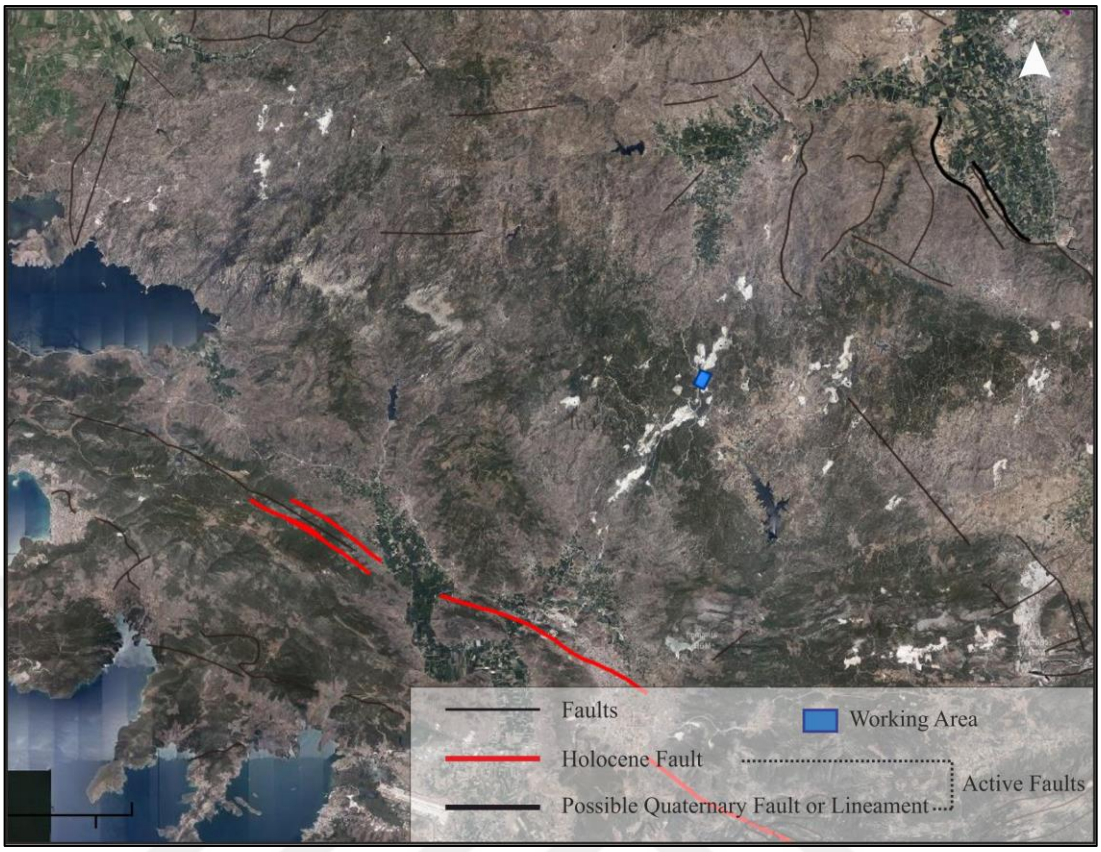

Figure 3.3 Active faults around the working area (MTA, 2021)

3.1 Foliation Planes

In the measurements made in the eastern part of the Albite Quarry to determine the discontinuity orientations, it is seen that the foliation planes in the gneiss masses show a very wide changing orientation depending on the deformation. It was determined that some of the inclination directions of the foliation planes at the observed research points were inclined towards the slope and some were directed out of the slope. The fact that these foliation planes, whose slope directions are oriented in and out of the slope, were found in the same way in another open pit of the same company, showed that this region was deformed and this study is compatible with the literature. (Karagöz, et al., 2016). At the same time, in the study of Karagöz, et al., (2016), the directions of foliation planes are NS or NW-SE oriented, and Tanyas., (2011) who did his master's thesis in the same region, determined these directions as NNE-SSW. proved that it has foliation planes that change by being subjected to deformation (Table 3.1). These deformation traces can be clearly seen in the study area (Figure 3.4). It was determined that foliation planes with high persistence oriented out of slope form a planar sliding

mechanism and cause slope sliding in the quarry (Figure 3.5). Determination of planar slidings caused by foliation planes by kinematic analysis technique is presented in detail in Chapter 5. The average orientation of the foliation planes measured in this thesis was determined as 26/179, and the rose diagram and angular distribution of these 129 foliation planes are given in Figure 3.6.

Figure 3.4 The field view of foliation planes that change (folds) due to deformation (Personal archive, 2021)

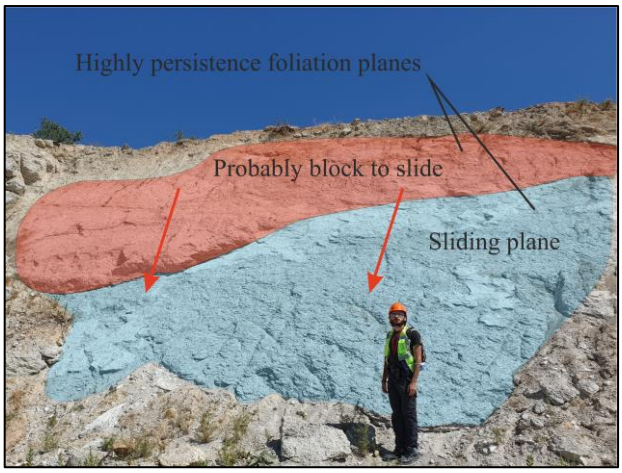

Figure 3.5 Foliation planes forming a planar sliding mechanism and causing sliding (Personal archive, 2021)

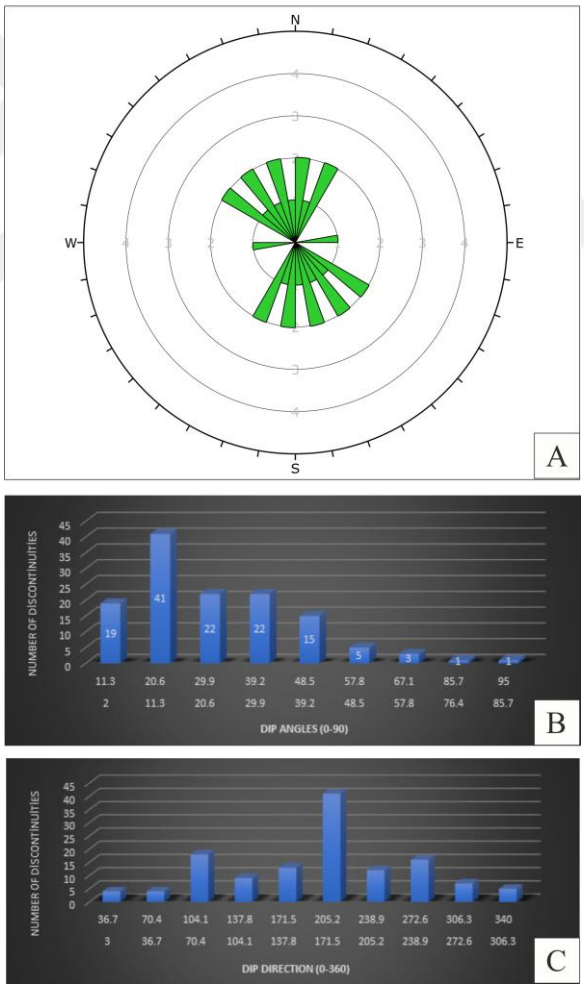

Figure 3.6 Rose diagram of the foliation planes observed in the open pit (A), the angular distribution graph of the dip angles of the foliation planes (B), the angular distribution graph of the dip directions of the foliation planes (C)

Table 3.1 Results found by different researchers working in the same region.

References	Directions of Foliation Planes
Tanyas., (2011)	NNE-SSW
Kadakçı Koca, et al., (2014)	NW-SE
Karagöz, et al., (2016)	NS or NW-SE
This publication (2021)	NW-SE or NW and NE-SW

3.2 Joints

The discontinuity sets were examined in detail in the observations on the benches in the study area. The stereonet image and rose diagram of these discontinuities presenting many different orientations are shown in Figure 3.7. It has been determined that the inclination angles of these discontinuity planes, which offer different orientations, are generally between 70-90 degrees. By looking at this result, it was supported that the dominant mass movement in the quarry was the toppling type failures. The dominant joint sets of these discontinuities were determined with the Dips V7.06 program. These joint sets are determined as 5 pieces and each set has a different number of discontinuities. The angular relations of the dominant joint sets obtained and the angular distributions obtained without being dependent on the discontinuity sets (all discontinuity planes) are given in Table 3.2.

Table 3.2 Angular distributions of discontinuity sets.

	Number of Discontinuities	Dip Angle	Dip Direction
Set 1	151	70-88	69-100
Set 2	244	60-90	320-356
Set 3	182	58-88	144-165
Set 4	43	10-22	148-205
Set 5	202	58-89	249-280
All Disc.*	**1820**	**05-90**	**003-358**

*: Number of all discontinuities before sets are determined.

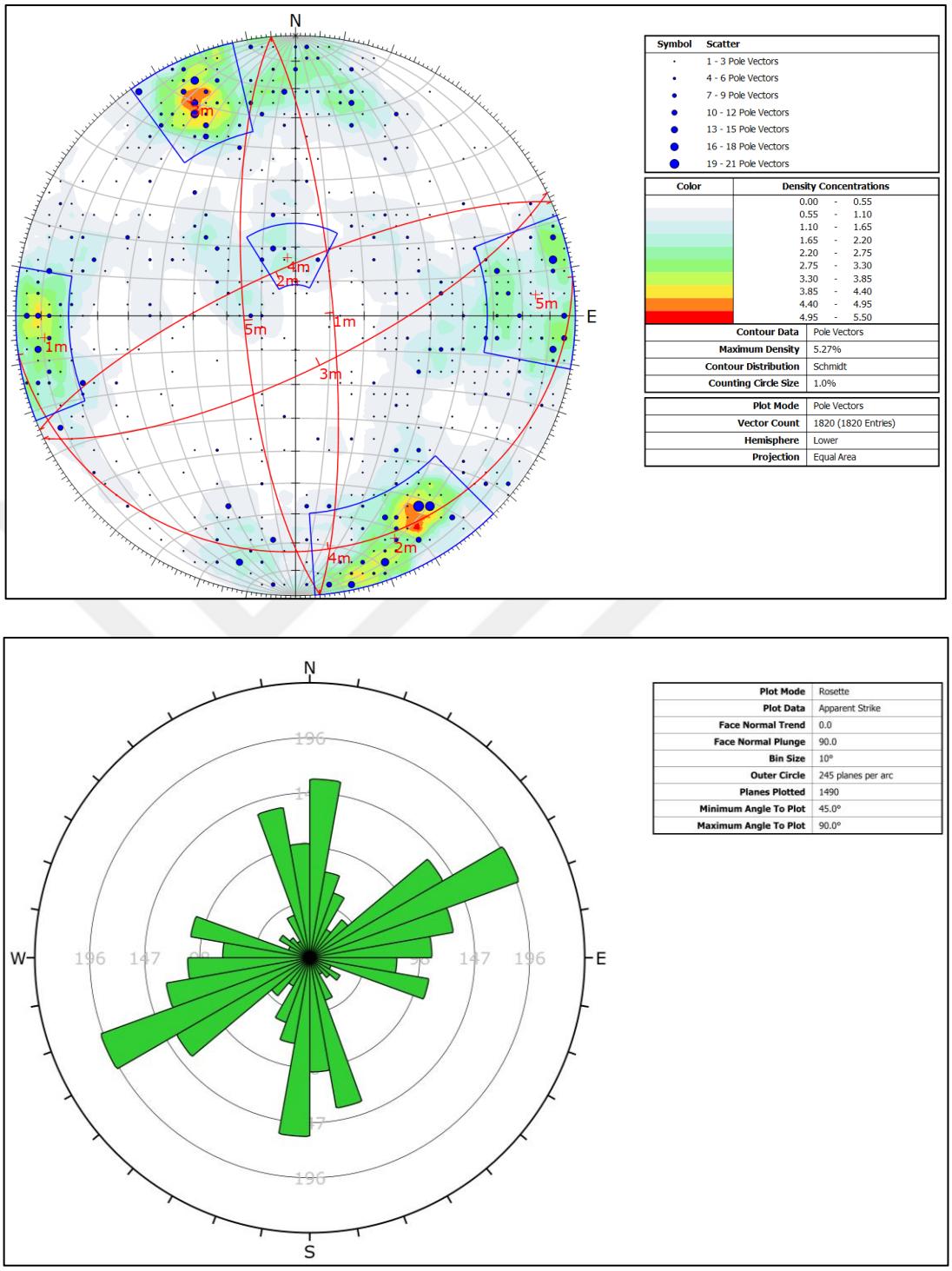

Figure 3.7 Contour diagram and rose diagram of all discontinuity (1820 pc.) measurements obtained

CHAPTER FOUR

ENGINEERING GEOLOGY

In this thesis, a series of field studies were carried out in the problematic part (eastern part) of the open pit within the scope of engineering geology. The following studies were carried out in the observations made at a total of 10 benches and 141 points (Figure 4.1).

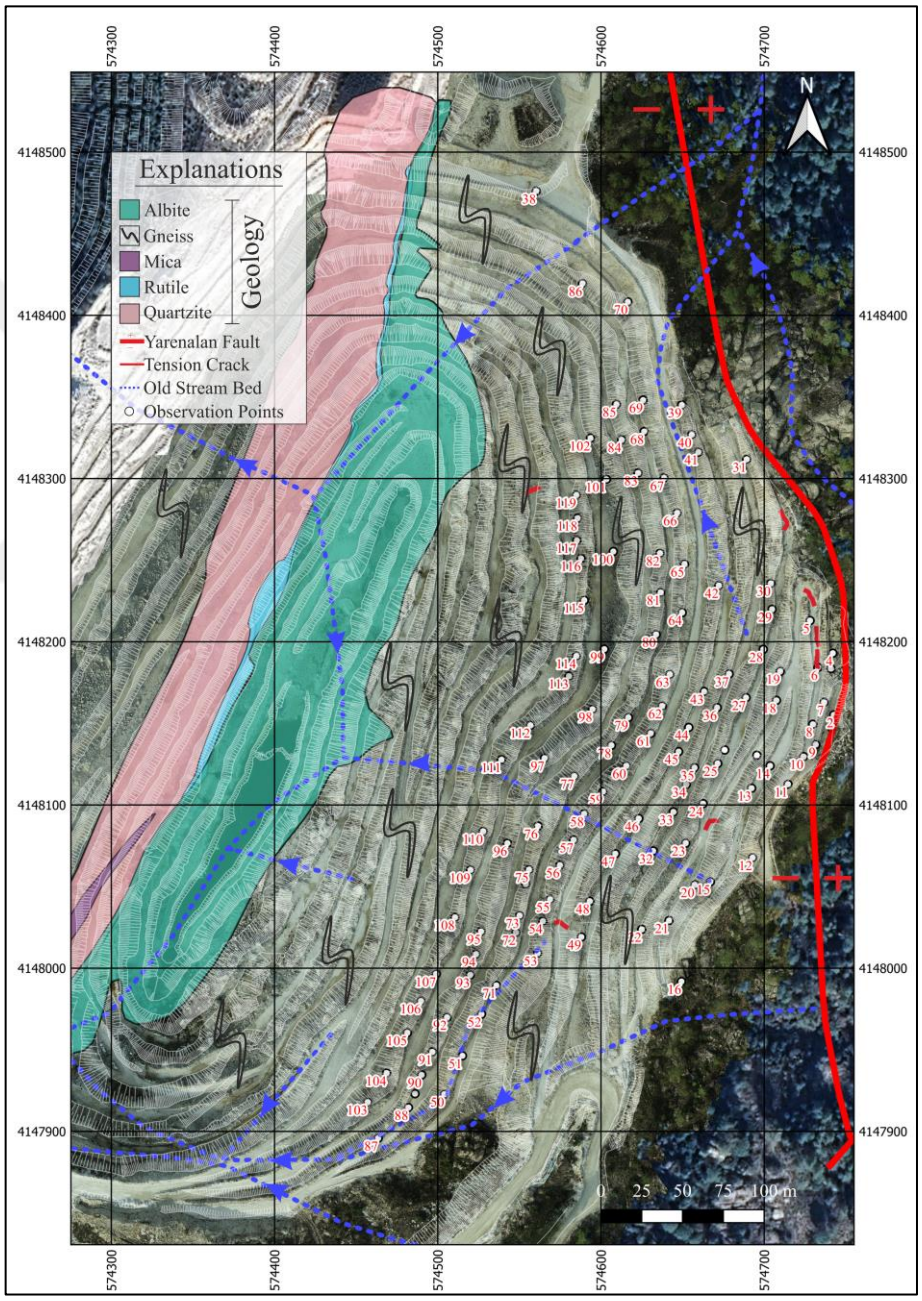

Figure 4.1 Engineering geology map of the study area

1. Measuring discontinuity planes

2. Schmidt hammer experiment

3. Roughness comb measurements

4. Recording some data of discontinuities (continuity, clearance, water condition, determination of discontinuity spacing, etc.)

This Open Albite Pit is an open pit with 16 benches in its eastern part and presenting a geometry with a slope angle of approximately 50-65 degrees and an overall slope angle of approximately 26 degrees (Figure 4.2). With these studies, it was aimed to determine the characterization of the problematic part of the quarry in terms of discontinuities (more structural factors) and to analyze and evaluate the stability of the slope. Schmidt hammer tests, roughness measurements and discontinuity measurements could not be made in some of these 141 observation points (12) made in the operational stages, since the slopes at these points lost their rock feature and/or did not contain a dominant discontinuity plane, as moderate to moderate-high degree of weathering was dominant. These segregated regions are explained in detail in a sub-title in this section.

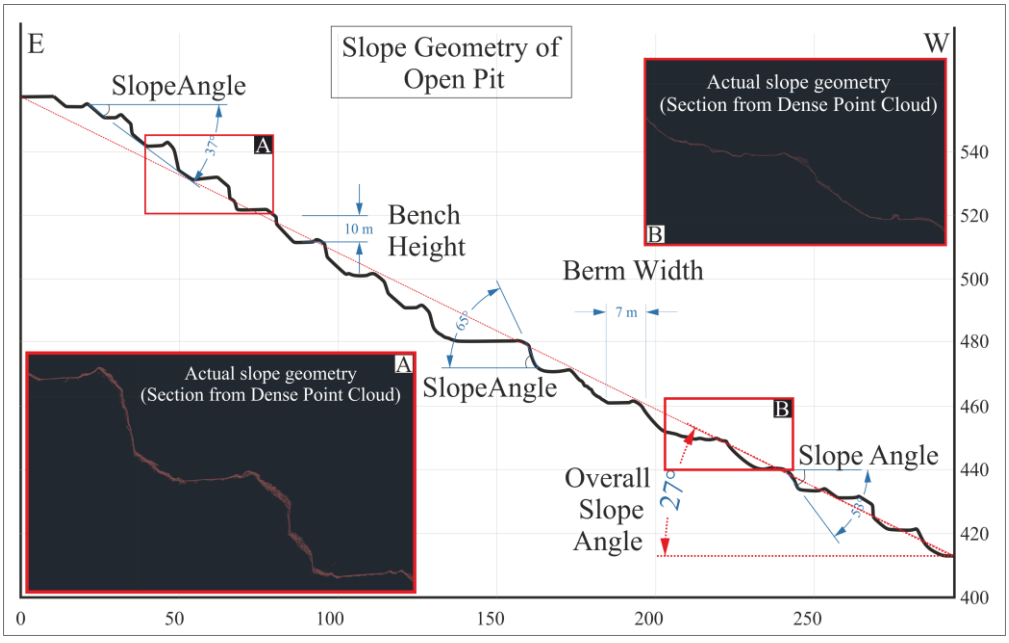

Figure 4.2 Slope geometry of Open Pit

4.1 Properties of Discontinuities

In the observations made in the eastern part of the open pit, the features of the discontinuity planes were made with the Scan-Line method in accordance with the standards recommended by ISRM (2007). Scan-Line was carried out at 141 points selected at regular intervals as conditions allowed. At the points where the weathering zones exist, only the properties of the weathered rock mass were examined and Scan-Line measurements could not be made. In some slopes observed, the orientation of the discontinuity planes was obtained by remote sensing method due to occupational safety (the discontinuity planes being close to the top of the slope, areas where rockfalls are found, etc.). This method is explained in detail in another sub-section in this section.

4.2 Orientation of Discontinuities

A total of 129 foliation planes and 1820 discontinuity measurements were taken in the eastern part of the open pit. Contour diagram and rose diagram of foliation planes and discontinuity planes are given in CHAPTER THREE. Due to the previous deformation of the region, the faults in the vicinity of the operation area and the controlled blasting for production, the rocks were broken along the weakness planes and formed discontinuity sets, which further increased the number of discontinuities. Joint sets developed perpendicular to the NW-SE trending Holocene and Quaternary faults (Çine Fault) in the northeast and southwest of the study area are dominant. In general, joint sets developed due to tectonism constituted the main subject of this study.

4.3 Aperture of Discontinuities and Filling Material Condition

The condition of the infill material between the walls of the discontinuity planes (infill thickness, type of infill material, etc.) directly influences the shear strength of the discontinuity plane. For example, if the fill thickness between the discontinuity planes is greater than the roughness amplitude of the surface, the shear stress is directly controlled by the fill (Figure 4.3).

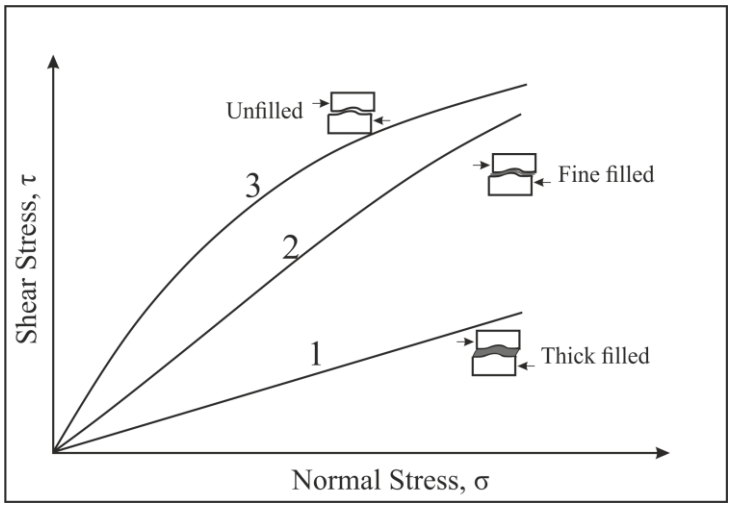

Figure 4.3 The effect of filling material thickness on shear strength (Hoek & Bray 1981)

In the examinations made at some observation points in the open pit, it was observed that there was a small amount of filling between the discontinuity walls (Figure 4.4). The thickness of this filling material varies between 0.5 cm and 5 cm. In addition, gneiss weathering product and quartz in some places were observed as filling material in the slopes near the weathering zones. The openings of the discontinuities in the slopes studied in the study area differ from region to region (Figure 4.5). Since the amount of clearance between the discontinuity walls will affect the deformability of the rock, it is also an important parameter in terms of stability. The first factor that has a direct impact on openness; It is the opening between the vibration and energy created by the controlled blasting (presplitting) made due to production in the quarry and the discontinuity walls with less opening. In regions where blasting is not performed, this clearance is relatively less than in other regions and varies between 0.2 cm and 1 cm. Another factor affecting the opening in the study area is that the force acting on the discontinuity walls is eliminated due to the removal of the load, and the planes of weakness such as cracks and fractures pass to the release mechanism, leading to an increase in this opening.

Figure 4.4 Weathering product filling material observed between discontinuity walls on slopes near weathering zones (Personal archive, 2021)

Figure 4.5 Discontinuity planes with different apertures observed in slopes at different investigation locations (Personal archive, 2021)

4.4 Roughness and Waviness of Discontinuity Planes

Roughness can be defined as the deviation of the discontinuity plane from flatness on a small scale. The waviness is defined as the deviation of the discontinuity plane

from the planeness on a large scale. Roughness and Waviness are also an influencing component on shear stress, just as in the case of infill. These parameters are in two different components. 1.Parameter; roughness 2. Parameter is used to define waviness. In this study, the roughness of the discontinuity planes on the slopes at the observed observation points was determined by using a profile comb (Figure 4.6).

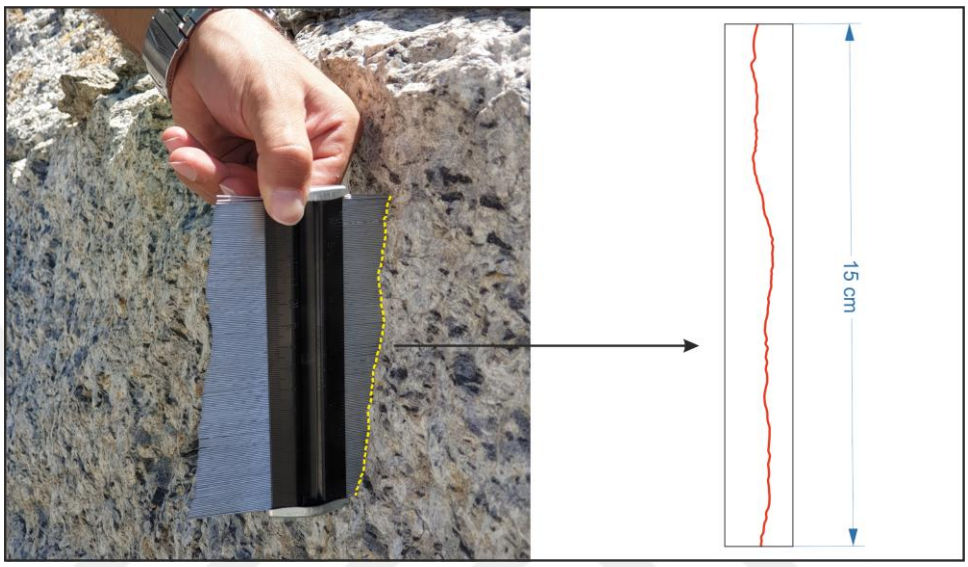

Figure 4.6 Roughness comb measurement on the discontinuity plane

In the observations in the study area, the surface roughness of the rock slopes varies from region to region, but it has been seen that it has a medium and very rough structure in general (Figure 4.7). Roughness measurements were made in almost all of the discontinuity planes in the investigated slopes. Since the slopes in the weathering zones lost their rock feature, roughness measurement could not be made at the x point.

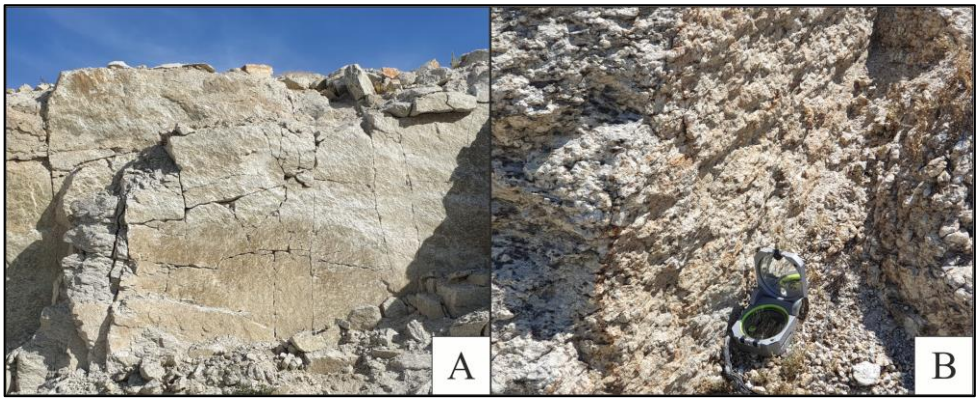

Figure 4.7 Roughness in slopes; (A) Slightly rough surface, (B) Very rough surface (Personal archive, 2021)

4.5 Water Condition on Discontinuity Surfaces

Almost all of the 141 inspection points of the open pit were made during the summer months. In the observations made in the study area, the water outlet and leakage points could not be determined in detail. In the period when the working period approached the winter months (November and December), water outflow was observed in the cracks of the slopes at some stages due to the increase in the groundwater level with a slight increase in precipitation (Figure 4.8). Since the study was generally carried out in the dry period, the water condition of the discontinuity walls was evaluated as "dry" and this situation was taken into account in the stability analyses. As seen in Figure 2.3, the months with the most precipitation are November, December and January. The effect of water on failures in this quarry is great, since water infiltrates the walls of discontinuity, weakens the rock strength and creates stability problems. The fact that the production activities of the enterprise were stopped in November-December 2019 due to the failures in the eastern part of this open pit supports this phenomenon. Although not much water outflow could be detected in the discontinuity planes of the slopes, it was determined that the ground between 400 and 550 elevations in the operational stages is partially wet-moist.

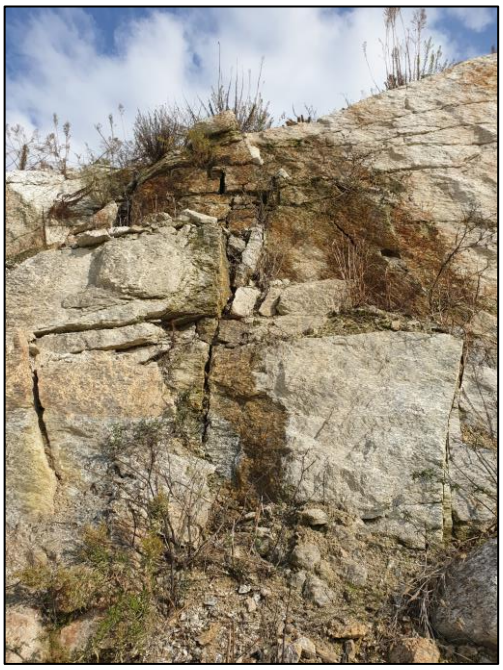

Figure 4.8 Seepage point seen on the slope at the observation location 116 at 470 m elevation (Personal archive, 2021)

4.6 Frequency of Discontinuities

The frequency of discontinuities affects the strength of the rock mass as well as a factor that causes instability problems. In this thesis study, the distance between the discontinuities and the number of repeating discontinuities were recorded by measuring the tape measure taken perpendicular to the discontinuities in the slopes at the observation points (Figure 4.9). Since there are discontinuities with many different orientations in the eastern part of this quarry, the frequency of these discontinuities also varies (Figure 4.9). The distance between the discontinuities, which varies from region to region, varies between 1 cm and 1 meter. The distances between these discontinuity walls, which vary widely, formed a parameter that directly affects the instability mechanism in this quarry where discontinuity-controlled failures occur. Since these distances between the discontinuity walls are also effective in the formation of blocks, it has been determined that as the distance between the discontinuities decreases, the probability of failure increases and creates a danger.

Figure 4.9 Varying distances between discontinuity walls on slopes at different observation points (Personal archive, 2021)

4.7 Persistence of Discontinuities

The continuity of the discontinuities on the slopes at the observation points were also recorded in the Scan-Line measurements made in this open field. These discontinuity planes, which offer continuity in a wide range as in the frequency of discontinuity, are an element that should not be ignored in stability problems. It was determined that the continuity of the discontinuities in the examined slopes exceeded the bench length by 1 meter and reached 25-30 meters. The field view of these discontinuity planes that offer continuity at many different distances is given in Figure 4.10. For this reason, considering the classification suggested by ISRM (2007), the continuity of these discontinuities was determined as "very high continuous".

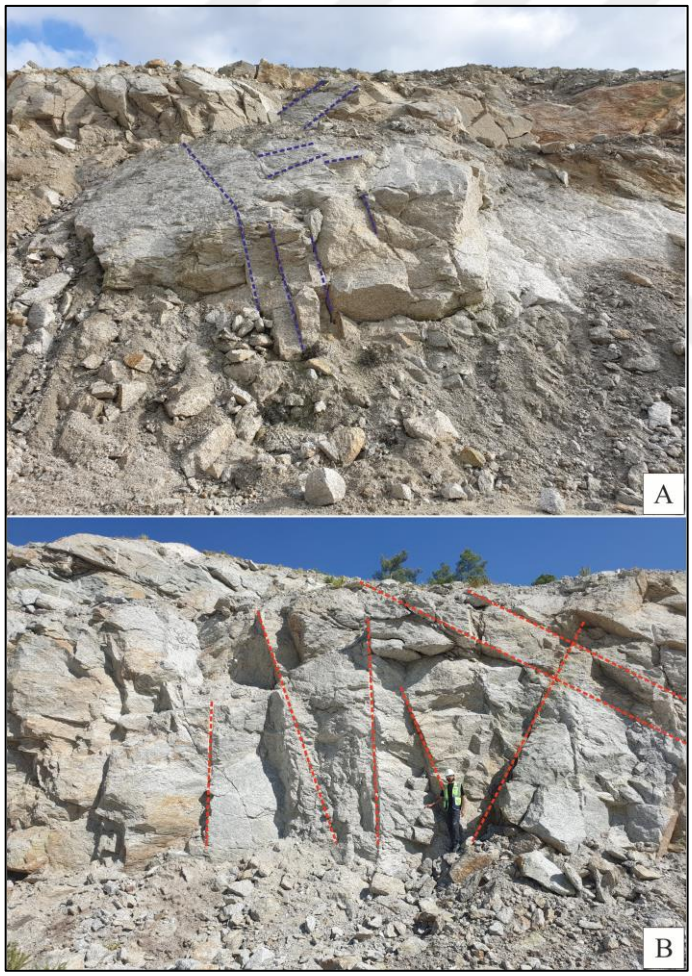

Figure 4.10 Persistence of discontinuities on different slopes; (A) Discontinuities with approximately 1-3 meters of persistence, (B) Discontinuities with approximately 5-10 meters of persistence. *(Slope height: ~10m)* (Personal archive, 2021)

4.8 Strength of Discontinuity Walls

L-Type Schmidt hammer was used on the slopes in the observed benches as much as possible (in Unweathered slopes with rock features) (Figure 4.11). By using Schmidt hammer rebound values (Barton and Choubey 1977), the uniaxial compressive strength of the discontinuity planes was found using Equation 1 proposed by. When the rebound values obtained are examined, these values vary between 11 and 55. The UCS values obtained from the rebound values also vary in a wide range, with these values between a minimum of 17 MPa and 61 MPa. Despite these varying UCS values, these values are predominantly around 17 MPa to 41 MPa (Figure 4.12).

Figure 4.11 L-Type Schmidt hammer test on slopes (Personal archive, 2021)

The average of all UCS values obtained in the Schmidt hammer test results on gneisses at 125 points was determined as 32,713 MPa. In the laboratory test results he conducted on 15 gneiss samples (Tanyas, 2011), who conducted a thesis study in another open pit mine located in a very close region belonging to the same enterprise in the previous years, he stated the average UCS value as 33.4 MPa. It can be seen from here that the UCS values obtained from the Schmidt hammer test results maintain

their consistency. Since the strength of the rock material is accepted as an important criterion in the instability evaluations, these values are also taken into account in the slope instability evaluations in this study.

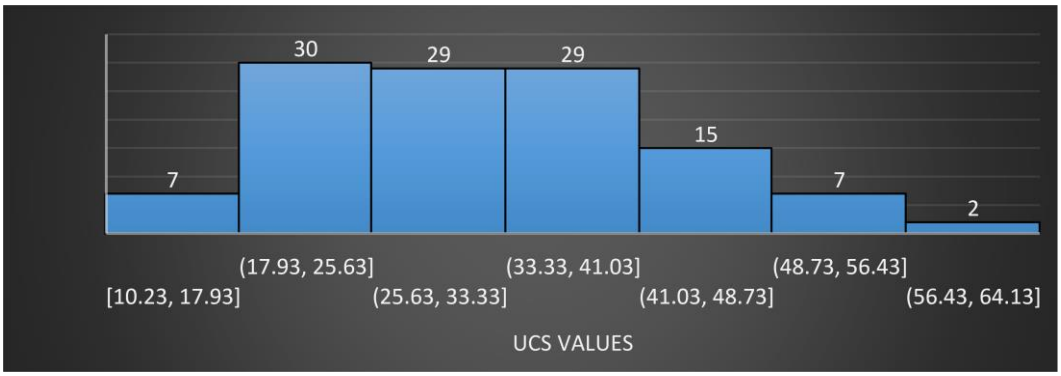

Figure 4.12 Histogram graph of UCS Values

$$Log10\ (\sigma_c) = 0.00088\ \gamma R + 1.0l \qquad (4.1)$$

Here, σ_c: Uniaxial compressive strength value (MN / m^2), γ*: dry unit weight of the rock (kN/m^3), R: rebound number

* This value was taken as 26 kN/m^3 from (Kadakçı, K. 2014).

As explained in the sub-title "Kinematic Analysis" in CHAPTER FIVE, the characteristics of the rock material (internal friction angle) are taken into account as well as the geometric relationships of the discontinuity orientations. Since the engineering properties of the rock material will also affect the rock mass, the strength value in terms of failures also comes to the fore at this stage. Some of the UCS values obtained using Equation (4.1) are given in Table 4.1.

All obtained UCS values are presented in Appendix 2. At the same time, these point UCS values obtained were interpolated by selecting “Distance Coefficient Power” value of 2 in the “Continuous Mode” range in the “Linear Interpolation” method using the Inverse Distance Weighted (IDW) raster analysis in the QGIS software (Figure 4.13). The interpole map of the UCS values and the 3D model of the study area are given in Figure 4.14.

Table 4.1 The rebound numbers at some observation points and the UCS values obtained using Equation (4.1)

Location	Rebound Number										Sum	Mean	LOG(JCS)	UCS(MPa)
1	24	25	28	27	24	33	28	28	29	18	264	26.40	1.496	31.316
5	19	15	11	12	14	12	12	18	10	14	137	13.70	1.262	18.284
6	40	34	41	26	28	32	24	35	16	22	298	29.80	1.558	36.168
7	20	21	23	21	30	12	20	18	21	13	199	19.90	1.376	23.777
16	17	11	13	19	25	18	14	21	17	25	180	18.00	1.341	21.938
51	25	27	24	27	22	18	14	25	26	23	231	23.10	1.435	27.230
56	10	13	10	18	14	13	12	20	11	12	133	13.30	1.255	17.977
57	24	28	26	18	20	24	18	20	24	20	222	22.20	1.418	26.211
68	50	47	41	40	38	36	44	41	42	40	419	41.90	1.781	60.389
89	14	11	12	14	13	11	16	15	14	11	131	13.10	1.251	17.825
94	40	37	41	35	31	45	40	40	47	37	393	39.30	1.733	54.090
97	32	40	41	40	39	44	47	35	41	42	401	40.10	1.748	55.955
101	20	22	19	10	14	11	12	17	18	13	156	15.60	1.297	19.817
111	40	39	44	46	36	40	34	35	45	40	399	39.90	1.744	55.483
134	21	24	23	16	23	18	14	13	11	20	183	18.30	1.347	22.219

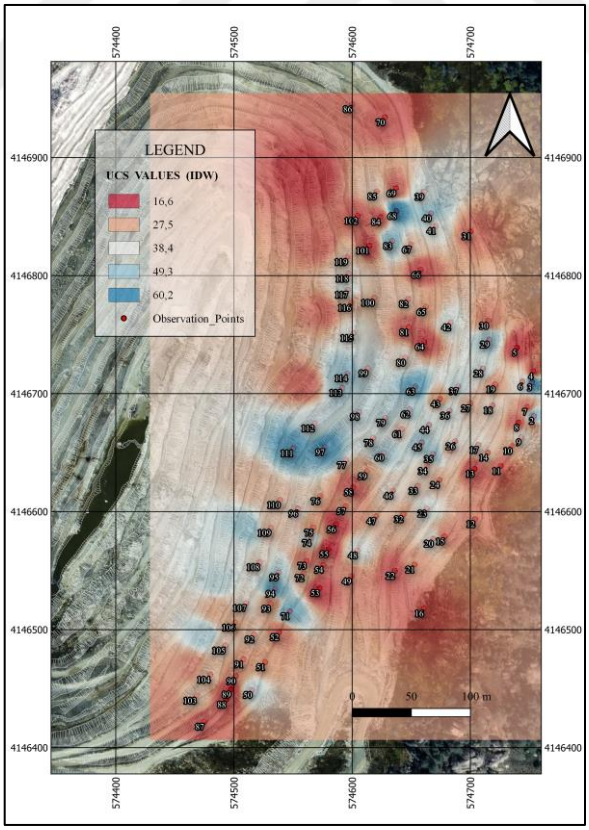

Figure 4.13 Thematic map of UCS Values created using the IDW method

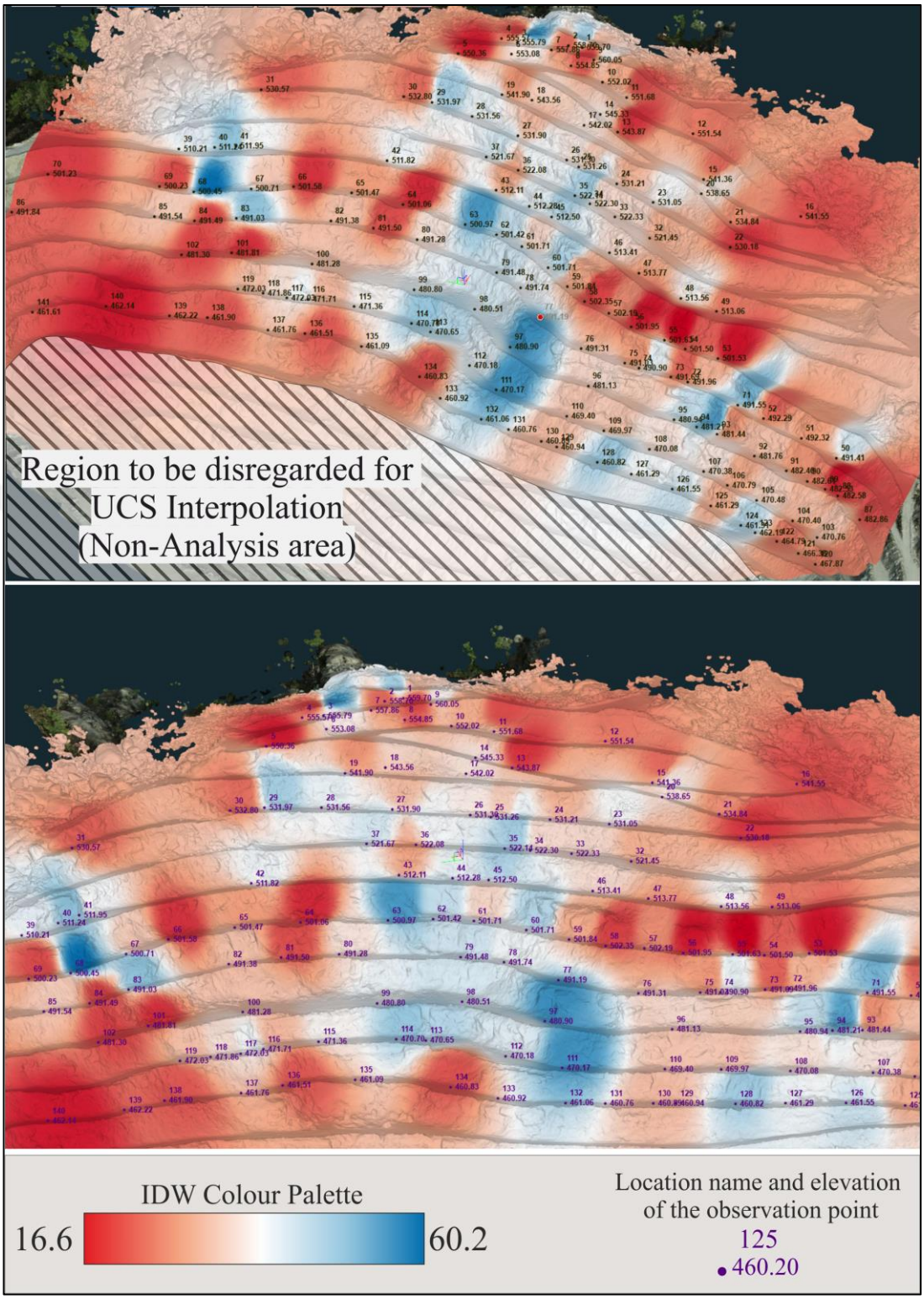

Figure 4.14 Overlaying the thematic map of the interpolated UCS values on the 3D model

4.9 Ground-Water

Groundwater level, a clear groundwater level could not be recorded, however, according to the information received from the authorized engineer in the enterprise;

In deep water drillings, groundwater was detected at -80 m levels in extremely cracked fault zones that hold water. Although it is not considered as a groundwater level, there is water accumulating in the cracks. Crack waters are observed at -2/-3 m depth in rainy periods.

4.10 Drillhole Data and Inclinometer Surveying

There is an inclonometer well located in the eastern part of the open pit and a 52 meters deep sounding drilled from the same point. The data of this inclonometer set up for motion monitoring are survey regularly (Figure 4.15).

Figure 4.15 The inclinometer hole located at 540 elevation in an open pit and its survey (Personal archive, 2021)

In this study, the readings (measurements) obtained from the inclinometer well and the drillings made from this point were examined and evaluated. The inclinometer well is located at 540 elevation and at the stage where the stress crack is located (Figure 4.16).

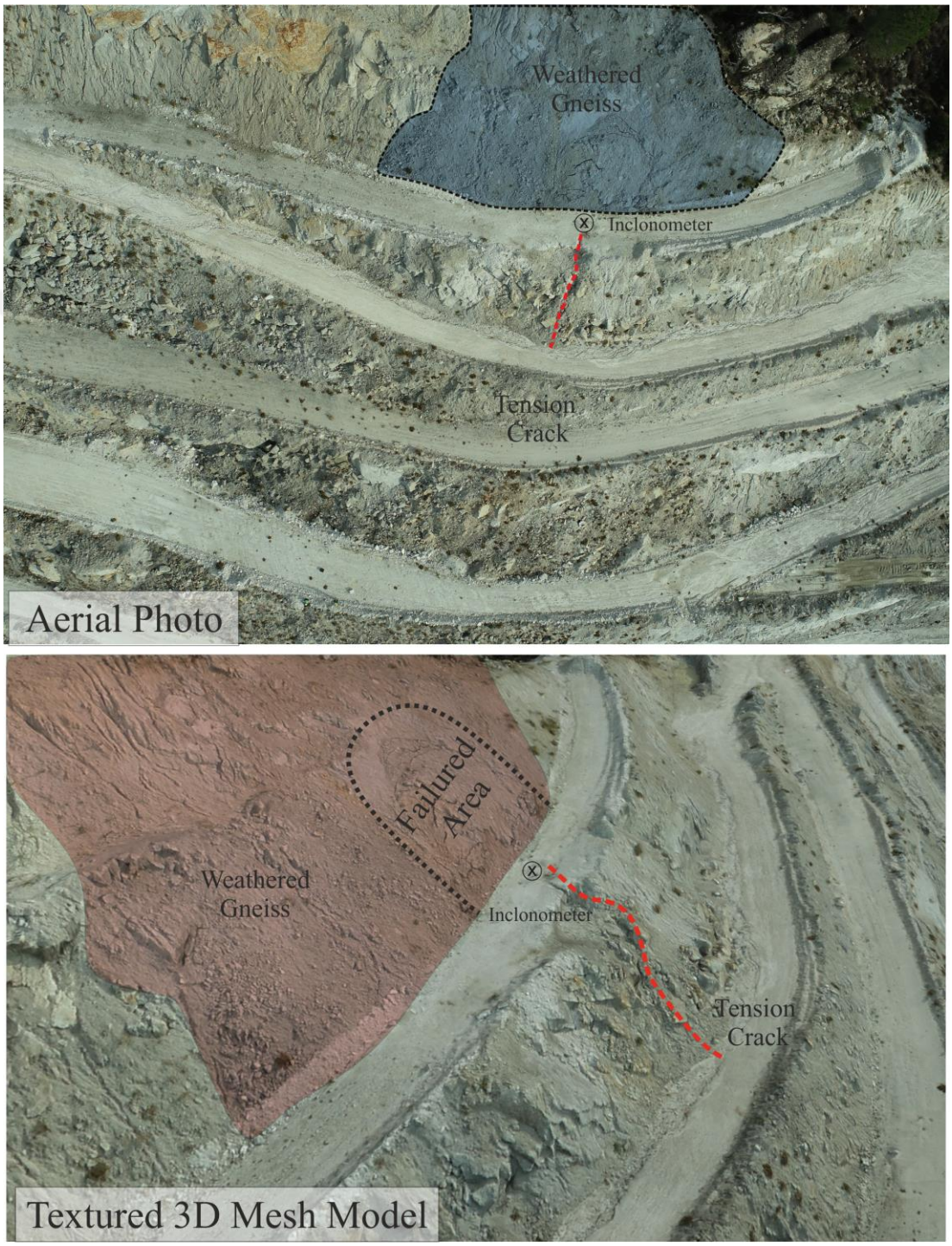

Figure 4.16 Stress crack and failed zone located in front of the inclinometer well

When the inclinometer records were examined, it was observed that between 14.12.2020 and 29.01.2021, there was a 10mm displacement between 28.5 and 30 meters (Figure 4.17).

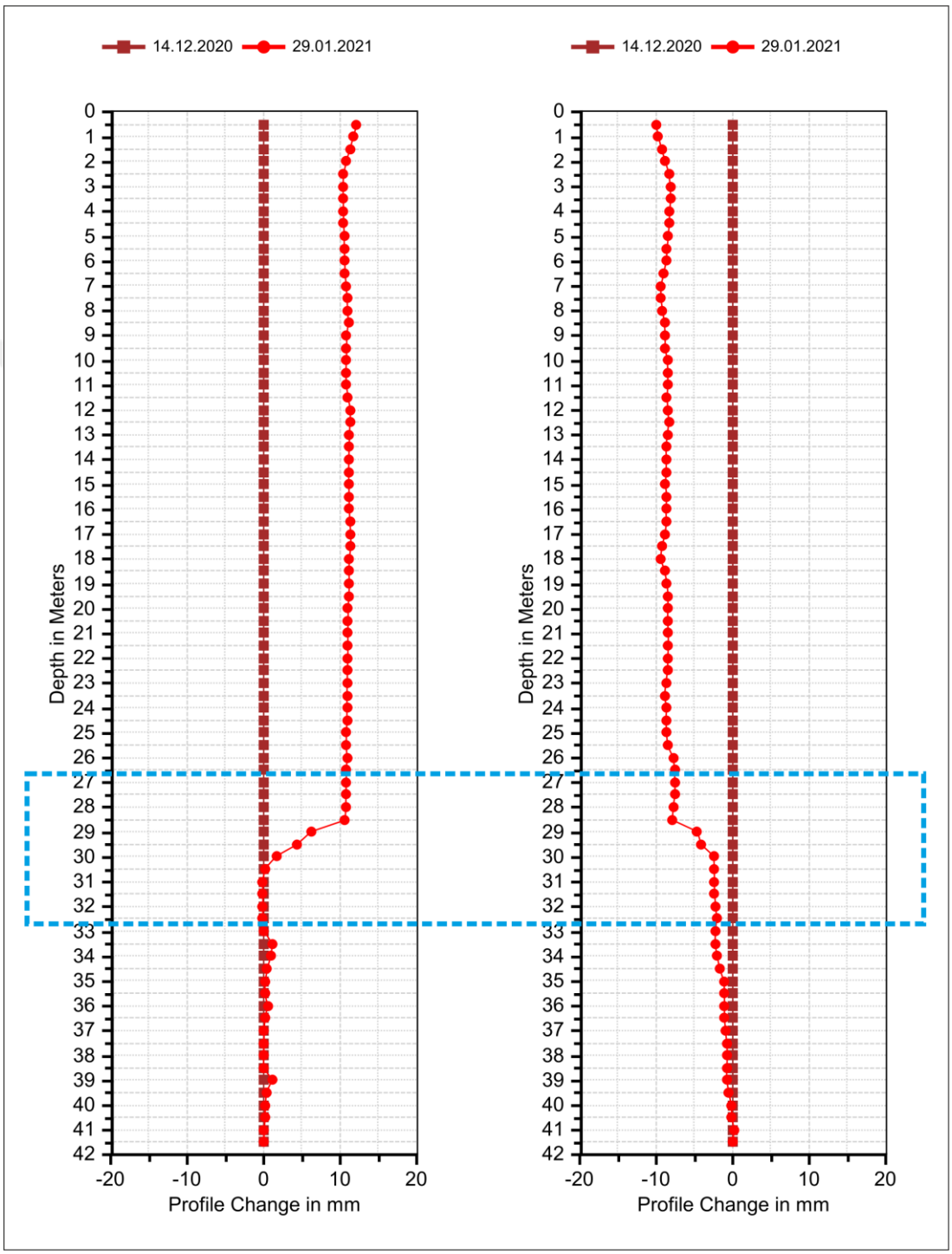

Figure 4.17 Anomaly observed between 14.12.2020 and 29.01.2021 between approximately 28 and 31 meters

When the drilling made from this well is examined, it is seen that the core losses increase and the CR% values decrease by approximately 30% and the RQD% values become zero in the maneuvers corresponding to this interval (Table 4). Thus, it has been concluded that the inclinometer data is consistent with the drilling result.

Table 4.2 Consistency of open pit drilling with geotechnical log results and anomaly range in inclinometer (indicated in red)

From	To	Length	RQD%	CR%
0	2.5	2.5	0.00	100.00
2.5	5.3	2.8	0.00	100.00
5.3	8.2	2.9	0.00	100.00
8.2	10.6	2.4	33.33	100.00
10.6	13.7	3.1	16.13	100.00
13.7	16.8	3.1	45.16	96.77
16.8	19.8	3	11.67	96.67
19.8	22.7	2.9	13.79	82.76
22.7	25.6	2.9	17.24	79.31
25.6	28.5	2.9	20.69	100.00
28.5	**31.4**	**2.9**	**0.00**	**69.31**
31.4	**34.3**	**2.9**	**3.45**	**68.97**
34.3	37.2	2.9	18.97	98.28
37.2	40.1	2.9	55.17	100.00
40.1	43	2.9	79.31	100.00
43	45.9	2.9	82.76	100.00
45.9	48.8	2.9	37.93	100.00
48.8	51.7	2.9	17.24	100.00

The reason for this change observed between 28-30 meters is thought to be a failure along the sliding circle. This anomaly, which is thought to be a sliding circle, could not show its effect very clearly on the surface. So; It can be considered as a continuous sliding failure in the lower stages (stages below 540 elevation), heel swelling due to the sliding circle, and/or failure to follow the traces of stress cracks in stages above 540 elevation.

Only a stress crack at 510 was observed in the same direction as the stress crack at 540 elevation. In addition, since the groundwater level was not high enough to affect the rock mass, and activities such as production and excavation were stopped, the

negative effects of vibration waves developed due to blasting did not have a negative effect on the development of this sliding circle. It is interpreted that this possible sliding circle may develop between these two stress cracks as shown in Figure 4.18.

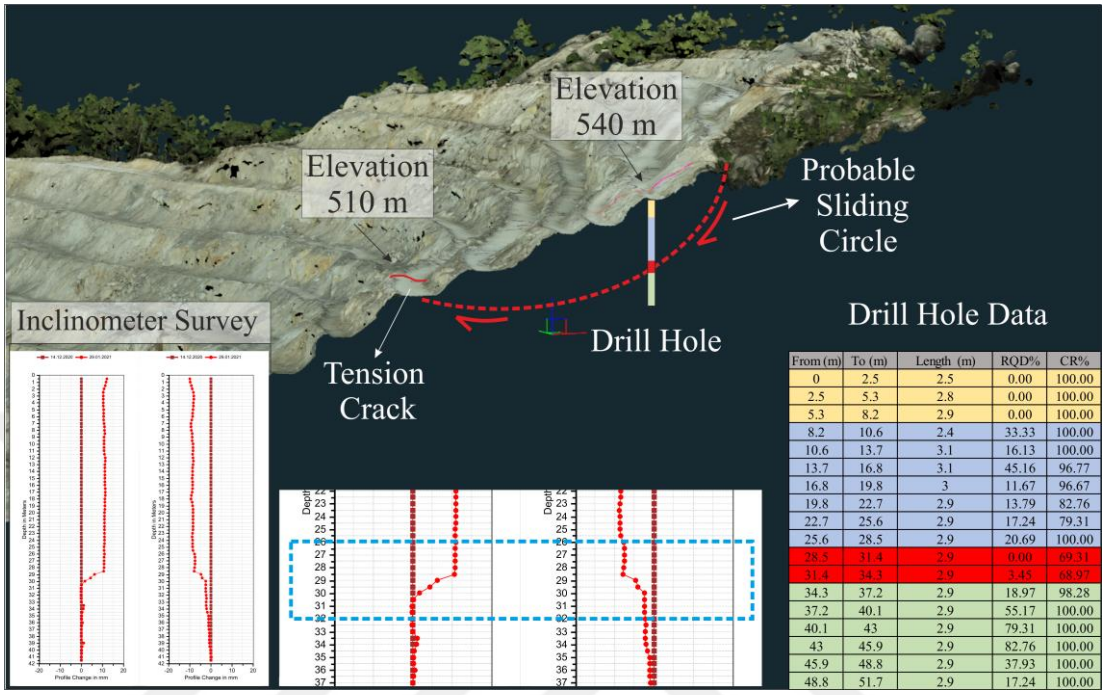

From (m)	To (m)	Length (m)	RQD%	CR%
0	2.5	2.5	0.00	100.00
2.5	5.3	2.8	0.00	100.00
5.3	8.2	2.9	0.00	100.00
8.2	10.6	2.4	33.33	100.00
10.6	13.7	3.1	16.13	100.00
13.7	16.8	3.1	45.16	96.77
16.8	19.8	3	11.67	96.67
19.8	22.7	2.9	13.79	82.76
22.7	25.6	2.9	17.24	79.31
25.6	28.5	2.9	20.69	100.00
28.5	31.4	2.9	0.00	69.31
31.4	34.3	2.9	3.45	68.97
34.3	37.2	2.9	18.97	98.28
37.2	40.1	2.9	55.17	100.00
40.1	43	2.9	79.31	100.00
43	45.9	2.9	82.76	100.00
45.9	48.8	2.9	37.93	100.00
48.8	51.7	2.9	17.24	100.00

Figure 4.18 The probable sliding circle drawn between the stress cracks observed between the 540th and 512th elevation, based on the drilling and inclinometer data

If we examine this sliding circle with other parameters; It has been observed that it is under many environmental and geomechanical effects. As seen in the thematic map created with the UCS values presented in Figures 4.13 and 4.14, the possible sliding circle drawn shows a projection in the region where the UCS values are low, including the observation points 21, 22 48, 49, 53, 54 and 55 (Figure 4.19). The low results in the Schmidt hammer tests performed at these observation points indicate that circular slippage may occur along the relevant line in this region. At the same time, as seen in the weathering zones map (Figure 5.1) shown under the main title of "Weather and Alteration", which will be presented in the next section, the projection of the probable sliding circle passes through the zone containing the weathering and debris material zone. In this zone, which contains weathered and debris materials, the material (geomechanical and geotechnical) properties of the rock mass have low values (weak), and there are slopes made of material that lost its rock feature and turned into soil in some regions (Example; Figure 5.2). The physical weathering of the rock mass under

various influences is explained in detail in the next section. However, the old stream beds, which are also included in the maps in Figures 2.2, 5.1 and 6.7, constitute the main element that supports this physical weathering mechanism. When the old stream beds continued their activities, the waters coming along the stream bed softened the geological units (metamorphic units) (changed the material properties by reducing their strength) and played a role in reducing the strength parameters. Accordingly, the cohesion value (c) decreased along the stress (tension) cracks, leading to circular shear failure.

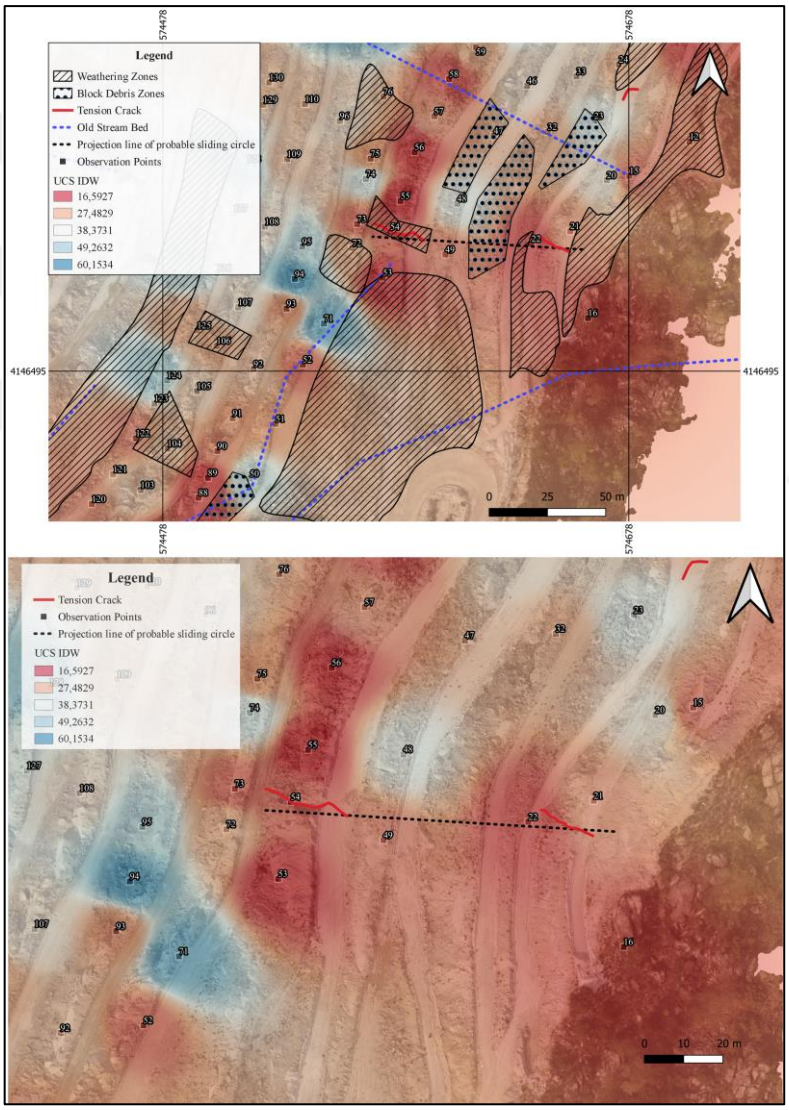

Figure 4.19 The relationship of the possible sliding circle with the UCS values and other parameters; (A) The projection line of the probable sliding circle is located near weathering zone, block debris zone and the impact area of old stream beds (B) Plain view of the relationship of the projection with the UCS values and stress cracks

Afterwards, this 10mm displacement observed in the inclinometer data and surface failure in the slope located on the upper part of the stress crack in the drilling location were determined. Geometry distortion (topographic change) due to this failure deformation was detected both by superimposing all the Digital Elevation Models obtained from the UAV flights during the study period and in the topographic cross section taken from the point cloud of the first and last day (4.20). If we examine the geological unit in this slope where failure has taken place, it can be defined as a weathered gneiss mass that has lost its rock feature, is accepted as a continuous material and has undergone ground structure. Therefore, the cohesion (c) value of this material decreased and disappeared with the effect of environmental factors and geomechanical properties. Depending on the decreasing cohesion value, failure occurred by undergoing a displacement of about 40 cm in the horizontal distance. This event has been accepted as one of the parameters that prepare the environment for slope failures (slidings) in this open pit (generally in the eastern part).

Figure 4.20 The probable sliding circle drawn between the stress cracks observed between the 540th and 512th elevation, based on the drilling and inclinometer data

CHAPTER FIVE

WEATHERING AND ALTERATION

In this section, the weathering and alteration of the slopes at the observation points will be discussed. In the observations made at 141 points, these observations were recorded as weathering points due to the weathering of the slopes at 27 points and some of them losing their rock characteristics. (Fig. 5.1).

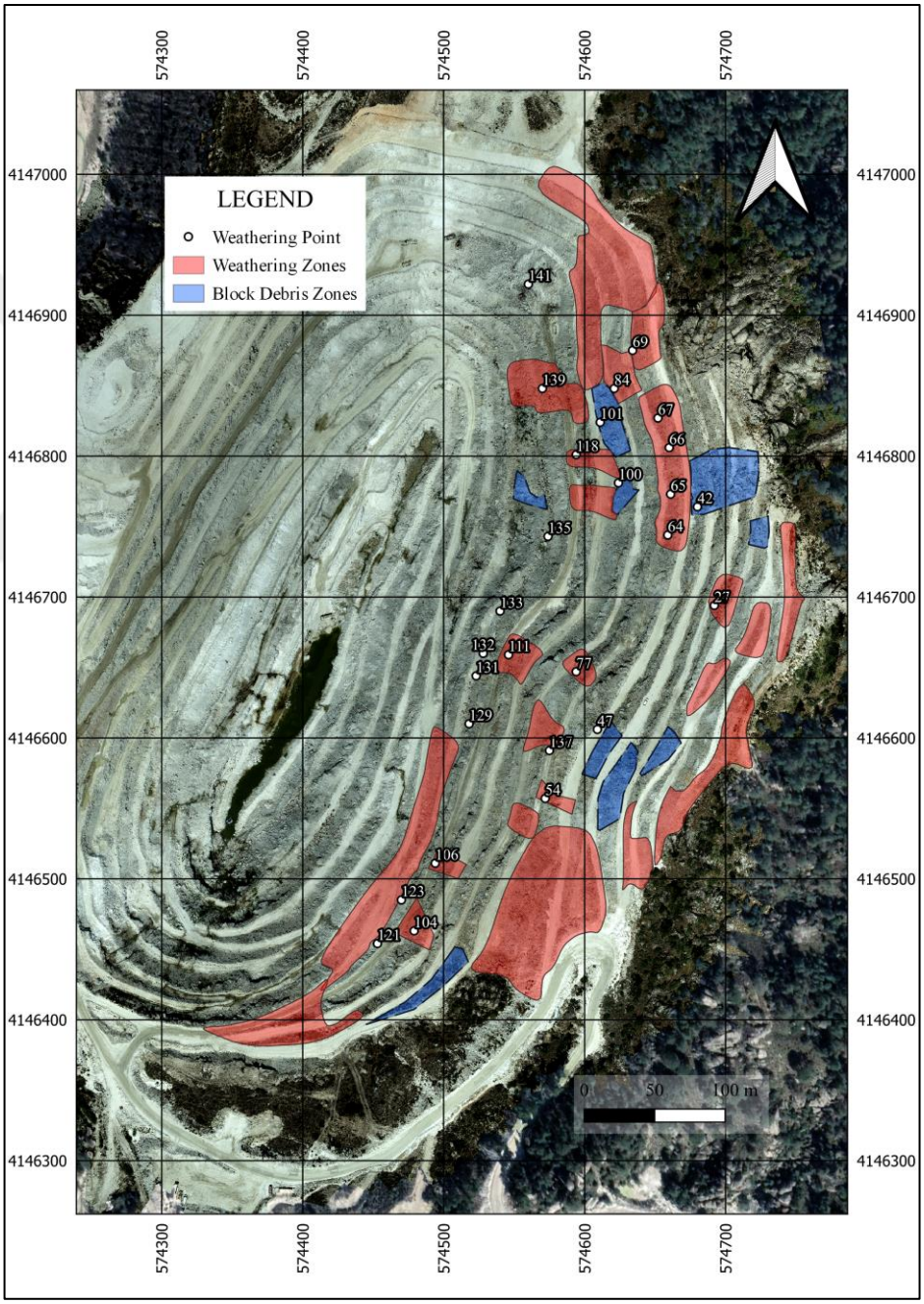

Figure 5.1 Map of the study area showing the weathering zones and block debris

5.1 Weathering Status

Weathering can be defined as changes in the surface or interior of rocks by exposure to physical or chemical effects. There are serious changes in the strength of the rock mass, which has been weathered under the influence of various environmental factors, and this change may result in instability problems. These environmental factors; are various parameters such as wind, water condition, load lift. In this open pit, the strength of the rock mass decreased due to these environmental factors, causing stability problems. As shown in Figure 2.2, the fact that the enterprise is located in many stream bed regions and that it receives excessive precipitation in winter due to the climate effect has reduced the strength of these rocks and adversely affected them. Likewise, due to the excavations made due to production and the corrections made in the stages during the slope design stage, as a result of the pressure release, the rocks underwent physical weathering and decreased in their mechanical properties and lost their rock properties (Figure 5.2). Due to these environmental effects, the dominant weathering status in the quarry was determined as MW and MW-HW. The impact areas of these observed weathering states were determined and the map in Figure 18 is shown. Due to the decreasing rock strength due to weathering, block debris and slidings of different sizes can be seen clearly in the quarry (Figure 5.3).

Figure 5.2 The weathering and loss of rock feature observed on the slope at the 111th Observation Point (Personal archive, 2021)

Figure 5.3 Block debris due to weathering seen at observation points 47 and 101(Personal archive, 2021)

5.2 Alteration

Mentioned in the previous sub-title that the strength of the weathered rock mass will decrease and it may cause instability problems. In the previous title, the results of physical weathering were mentioned in general. In this sub-title, the subject of alteration, which is a type of chemical weathering, will be explained. It is not known that weathering can reduce the strength of the rock in general, as well as increase the strength in the chemical weathering process such as alteration. As the effects of physical weathering can be clearly seen in this open pit, alterations due to chemical weathering processes can easily be seen.

As a result of the meeting of hydrothermal fluids with the rock mass, which developed due to faulting, oxidation occurred on the rock surface and it was observed that the strength of the rock increased at these points. The fact that the UCS values obtained from the Schmidt hammer experiments in these regions were also high, formed a supporting element for this phenomenon. In addition, the presence of a structural element such as the Yarenalan Fault in the study area also supports the faulting event. The presence of hydrothermal fluids released due to faulting is supported by the dendritic structure formed in the rock wall in the image in Figure 5.4.

Figure 5.4 Dendritic traces formed by the hydrothermal fluid located in the alteration zone and exposed due to faulting (Personal archive, 2021)

Some of the rock slopes that have oxidized surface and rusted orange tones in the slopes observed in the study area are shown in Figure 5.5. These alteration zones caused by hydrothermal fluids and the appearance of the rocks with this orange surface, which were determined during the observations, are given in Figure 5.6.

Figure 5.5 Rock slopes with oxidized surfaces (Personal archive, 2021)

Figure 5.6 Oxide zones seen from angled aerial photographs (Personal archive, 2021)

Mentioned that alteration, which is a result of chemical weathering, can increase rock strength. It was determined that the results of the Schmidt experiment performed

at these points (oxide zones at observation points) and the UCS values obtained from these values were higher than the slopes at other points (Table 5.1).

Table 5.1 The results of the Schmidt hammer test on the altered slopes at the observation locations

Location	Rebound Number										Sum	Mean	**UCS (MPa)**
24	22	28	31	20	24	22	25	28	28	20	248	24.8	**29.26**
25	30	27	24	33	25	21	31	30	27	26	274	27.4	**32.67**
26	28	25	30	31	38	31	34	28	22	33	300	30	**36.47**
30	13	19	20	27	24	11	21	27	19	21	202	20.2	**24.08**
34	39	32	25	23	30	24	26	27	34	28	288	28.8	**34.66**
44	28	37	31	31	24	38	34	38	28	33	322	32.2	**40.03**
60	39	41	46	26	32	39	43	24	28	35	353	35.3	**45.65**
63	37	38	42	42	38	37	45	38	41	38	396	39.6	**54.78**
68	50	47	41	40	38	36	44	41	42	40	419	41.9	**60.38**
78	28	35	33	35	36	22	30	35	33	29	316	31.6	**39.03**
82	24	26	30	26	31	28	27	25	21	27	265	26.5	**31.44**
83	39	33	29	45	37	40	42	37	40	29	371	37.1	**49.27**
95	35	30	40	44	45	25	27	35	30	32	343	34.3	**43.76**
109	34	35	34	35	22	24	20	19	21	26	270	27	**32.12**
114	35	41	40	39	35	39	38	22	34	44	367	36.7	**48.44**
115	30	30	38	30	31	40	31	28	25	25	308	30.8	**37.73**
119	28	23	30	20	20	35	20	32	33	21	262	26.2	**31.05**
124	31	34	38	35	42	35	34	37	30	34	350	35	**45.08**
125	24	21	18	19	22	30	28	33	22	30	247	24.7	**29.13**
126	37	40	41	34	22	45	20	33	35	33	340	34	**43.21**
127	26	38	32	20	35	33	42	29	37	27	319	31.9	**39.53**
130	20	21	34	24	28	25	30	31	22	24	259	25.9	**30.65**

CHAPTER SIX

SLOPE STABILITY ASSESSMENTS

6.1 Kinematic Analysis

There are different methods used to evaluate rock slope stability. Slope stability is generally evaluated with rock mass classification systems such as kinematic analysis, limit equilibrium analysis, numerical analysis and Slope Mass Rating (SMR) (Hoek & Bray (1981)., Hoek, (1999)., Ulusay Et al., (2001)., Pantelidis, (2009)., Alejano. Et al, (2011). Parameters such as the material properties of a rock slope, environmental conditions, bench height, slope angle and orientation of discontinuities play an important role in slope instability. For this reason, in order to evaluate the stability of a rock slope, it is necessary to examine the structural conditions of the oriented discontinuities in the rock slope in terms of whether they cause slope instability. This form of analysis takes into account the internal friction angle (ϕ), which is one of the shear strength parameters of the rock material, as well as geometric relationships. This procedure is known as kinematic analysis and is a purely geometric approach that does not take into account any stress or force acting on the rock slope (Park & West, 2001).

This method, which is also preferred in open pit mine slopes where discontinuity-controlled failures occur, is frequently used (Kıncal, (2021), Obregon et al., (2019), Bawa et al., (2017), Francioni et al., (2015). Kinematic analysis is widely used to potentially analyze various types of structurally controlled rock slope failures, and a conventional kinematic analysis is performed using the stereographic projection method. In the stereographic projection method, the measured orientations of the discontinuities are plotted on a stereonet and their stability is evaluated according to the orientation of the discontinuities and their friction angles (Park, Hyuck-Jin., et all 2015). Almost all stability analyzes of discontinuous rock slopes include kinematic checks prior to additional limit equilibrium analyzes to identify potentially unstable slopes (Aksoy, H., & Ercanoglu, M. (2007). The danger of this failure potential is investigated with Limit-Equilibrium analyzes Limit equilibrium analyzes take into account the shear strength developed along the failure plane, pore water pressure and external forces such as maximum horizontal ground acceleration (Kentli & Topal, 2004; Gürocak et al., 2008). Although limit equilibrium analysis is a simple method

that is widely used to evaluate the stability of slopes, limit equilibrium analyzes are sometimes insufficient when slopes are unstable by complex mechanisms such as excavation disturbance and discontinuity orientations (Eberhardt, 2003).

Within the scope of this thesis study, within the framework of observations made at 141 points, kinematic analysis was made for each slope where discontinuity measurements could be made (to the extent the conditions allowed). Due to the weathering conditions described in the previous sections, kinematic analysis technique was applied to determine the mass movements in 119 of the slopes located at 141 points (Table 6.1). Obtaining the necessary parameters (orientation of discontinuities and slope) in these kinematic analyzes were obtained with the help of both the traditional method and the photogrammetric method.

Photogrammetry technique and its details will be explained in detail in another chapter in this section. The internal friction angle, which is another parameter required for the kinematic analysis, was taken from as $\phi=23^{o}$ (Koca et al., 2020) working in the same open pit area. As indicated in Table 3.2, according to the results of this kinematic analysis made due to the high inclination angles of the main discontinuity sets, it was seen that the most dominant failure type was the toppling type failure with a rate of 45%. The types and percentage distribution of all these kinematic analysis results are given in the circular graph in Figure 6.1.

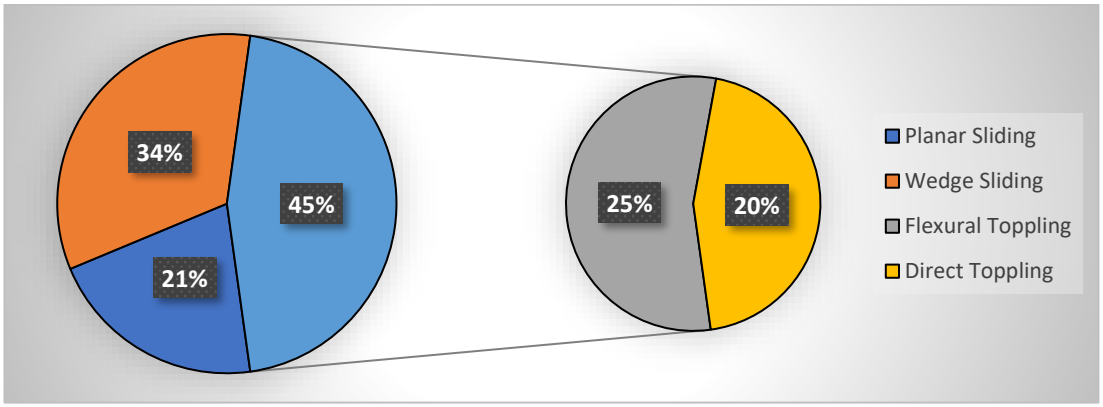

Figure 6.1 Presentation of kinematic analysis results in pie chart format

Table 6.1 Kinematic analysis results (-: Discontinuity measurement could not be taken for various reasons., K. Stable: Kinematically stable slopes., P: Planar Failure., W: Wedge Failure., FT: Flexural Toppling., DT: Direct Toppling)

Location	Failure Types	Location	Failure Types	Location	Failure Types	Location	Failure Types
1	FT	**36**	P/W	**71**	P	**106**	-
2	K. Stable	**37**	W	**72**	-	**107**	W-FT-DT
3	FT	**38**	W	**73**	W/FT/DT	**108**	P-W-FT-DT
4	K. Stable	**39**	P/FT/DT/W	**74**	P/W	**109**	P-W-FT-DT
5	FT	**40**	K. Stable	**75**	P/W/FT/DT	**110**	P-W-FT-DT
6	FT	**41**	W/FT	**76**	FT	**111**	-
7	K. Stable	**42**	-	**77**	-	**112**	P-W-FT-DT
8	P/W	**43**	W/FT/DT	**78**	P/W/FT/DT	**113**	DT
9	P	**44**	W/P	**79**	P/W/FT/DT	**114**	-
10	FT	**45**	K. Stable	**80**	FT	**115**	P-W-DT
12	K. Stable	**47**	-	**82**	W/FT/DT	**117**	W
13	FT	**48**	W	**83**	W/FT/DT	**118**	-
17	-	**52**	W	**87**	FT	**122**	W-DT
18	W/DT	**53**	W/FT	**88**	P-W-FT-DT	**123**	-
19	K. Stable	**54**	-	**89**	W-FT	**124**	K. Stable
20	W	**55**	FT/W/P/DT	**90**	P-W-FT-DT	**125**	W-FT
22	K. Stable	**57**	FT/W/P/DT	**92**	P-W-FT-DT	**127**	P-W-FT-DT
23	K. Stable	**58**	FT/DT	**93**	P-W	**128**	K. Stable
24	K. Stable	**59**	W/DT	**94**	P-W-FT-DT	**129**	-
25	P/W	**60**	W/FT/DT	**95**	P-W-FT-DT	**130**	P-W-DT
26	K. Stable	**61**	FT/P/W	**96**	P-W-FT-DT	**131**	-
27	-	**62**	FT	**97**	W	**132**	-
28	W/DT/FT	**63**	W/FT/DT	**98**	W-FT-DT	**133**	-
32	W	**67**	-	**102**	P-W-FT-DT	**137**	-
33	W/P	**68**	W	**103**	W	**138**	P-W
34	P/W	**69**	-	**104**	-	**139**	-
35	K. Stable	**70**	W/DT	**105**	P-W-FT-DT	**140**	P-W-DFT-DT
						141	-

6.1.2 Planar Sliding Failure

Planar sliding failure is a type of failure that occurs when a plane of discontinuity whose direction is approximately parallel to the slope surface slides down the slope along this plane. In order to this sliding failure to occur or to pose a potential hazard, certain geometric conditions must be met. These conditions are according to Hoek & Bray (1981) and Norrich & Wyllie (1996);

1. The angle of inclination of the plane of discontinuity must be smaller than the angle of inclination of the slope, that is, the plane of discontinuity must intersect the slope ($\alpha_{discontinuity} < \alpha_{slope}$).

2. The angle of inclination of the plane of discontinuity must be greater than the internal friction of the rock material ($\alpha_{discontinuity} > \phi$).

3. The direction of the slope and the direction of the discontinuity plane must be approximately parallel to each other or approximately ± 200 different from each other.

Planar sliding failures in the study area are examined under two sub-titles. These; They are planar slidings caused by foliation planes inclined out of slope and planar slidings caused by structural discontinuity planes formed due to tectonic movements. Foliation planes caused 12 of the 45 planar sliding failures in the 21% slice and the remaining 33 were caused by other joint sets. The distribution of these factors that cause planar sliding in the study area is given in the thematic map created on the orthophoto in Figure 6.2.

6.1.2.1 Planar Slidings Caused by Foliation Planes

These foliation planes, which are found in leucocratic gneisses (light colored/felsic) in the study area and offer variable orientation depending on the deformation, have created a stability problem in the quarry by causing planar slidings. These structural elements constitute an issue that should not be ignored in terms of slope instability due to the fact that these rock slopes excavated in the gneiss unit have foliation planes and local lineation and the weakness zones they have are high. The kinematic analysis of planar shear failure along foliation planes inclined out of slope is given in Figure 6.3.

Not all of these foliation planes, which have an average 45/320 orientation, cause shear failures. The mean orientation of the foliation planes causing the sliding was determined as 39/290. At the same time, the orientation of 12 slopes, which have slidings caused by foliation planes, was determined as 51/292 on average. The angular distribution graph of these foliation planes, which cause planar slidings, depending on the inclination angle/inclination direction is presented in the graph in Figure 6.4.

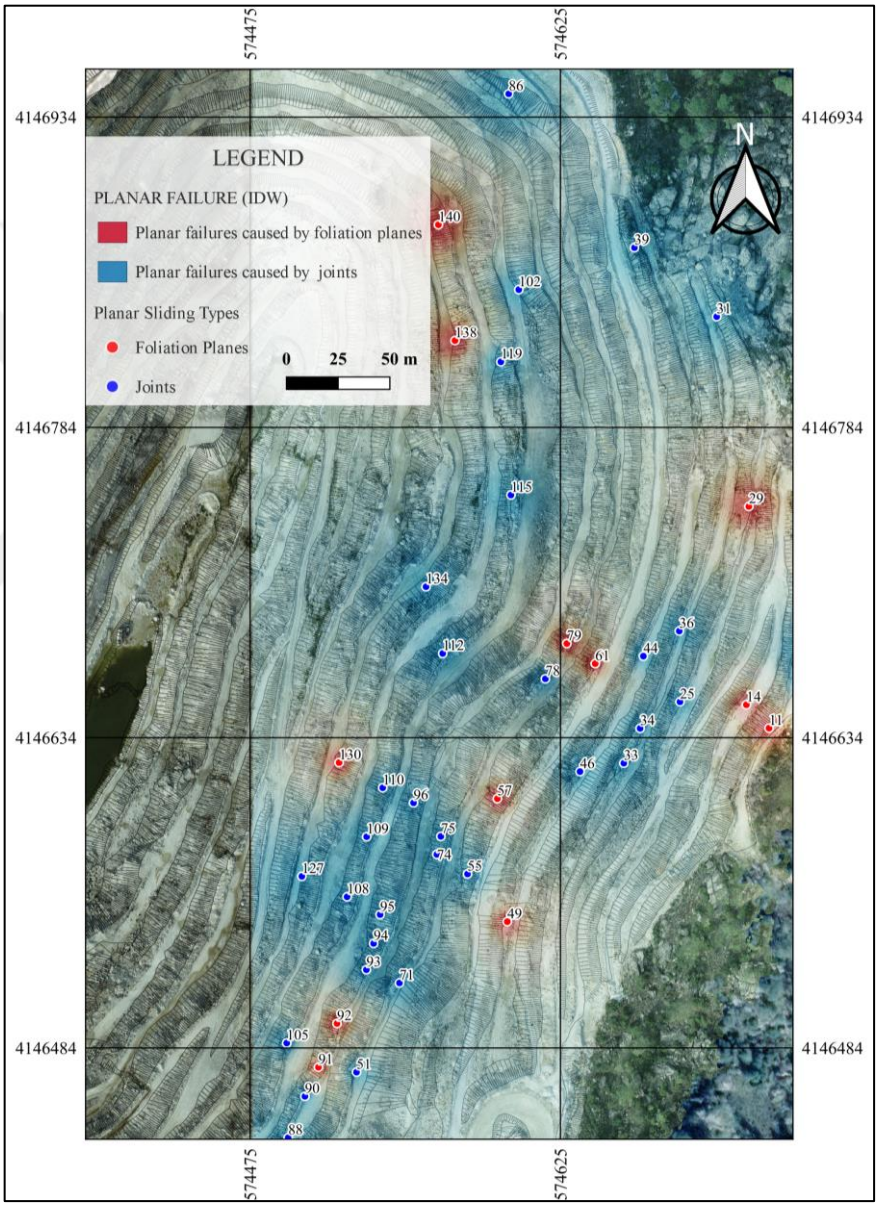

Figure 6.2 Thematic map of planar sliding failures determined by the kinematic analysis technique in the study area and the factors caused by these failures

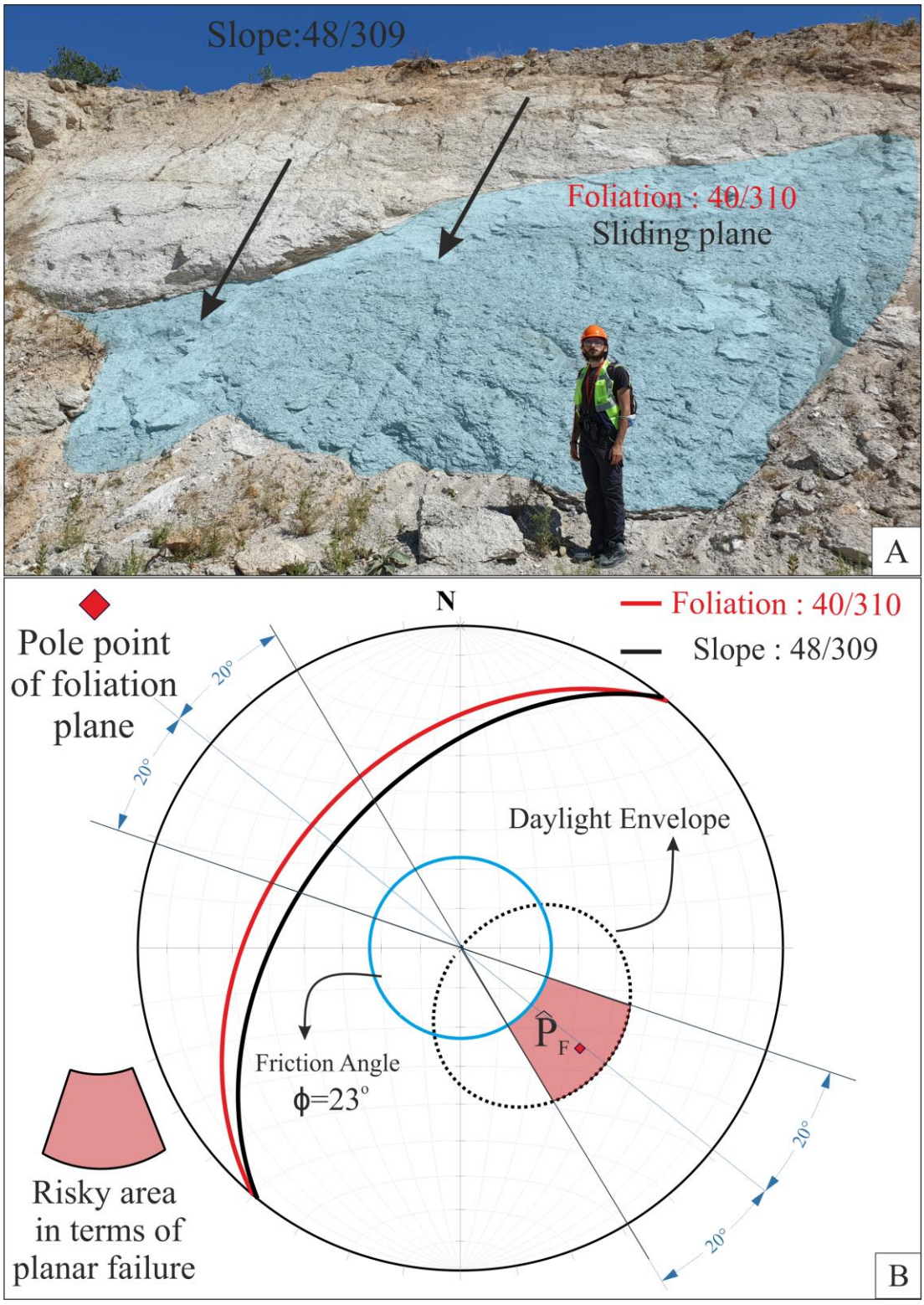

Figure 6.3 Planar sliding failure caused by foliation planes; (A) Field view, (B) Kinematic analysis (Lower hemisphere)

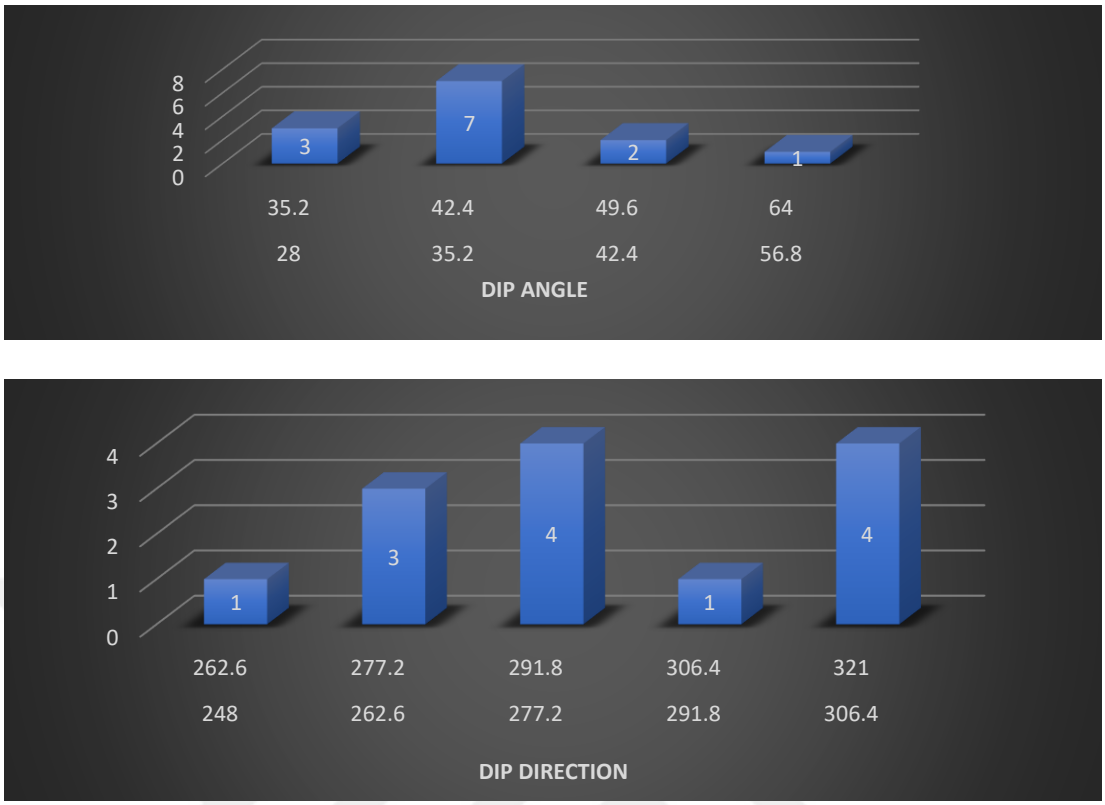

Figure 6.4 Graph showing the angular distribution of the orientation of foliation planes causing planar sliding

6.1.2.2 Planar Sliding Caused by Discontinuities (Joints)

In this subsection, the planes of discontinuity (joints) that cause planar shear failure will be discussed. In the kinematic analyzes made with the discontinuities taken in the eastern part of the study area, a total of 45 planar sliding potentials were determined. 33 of these 45 planar sliding were caused by discontinuity planes formed due to tectonism (Figure 6.5). The mean orientation of these discontinuity planes, which cause planar slidings, was determined as 41/285. Due to the presence of high-angle discontinuities in the study area and the low inclination angles of these discontinuities that cause planar sliding, it was observed that these discontinuity planes with the determined average orientation are not in the main discontinuity sets specified in Table 2. The graph containing the angular distributions of these discontinuities is presented in Figure 6.6. In addition, the average orientation of the slopes where the slidings caused by these joints are found to be 55/286. The field view of these planar slidings caused by the joints and their kinematic analysis using the lower hemisphere projection are given in Figure 6.5.

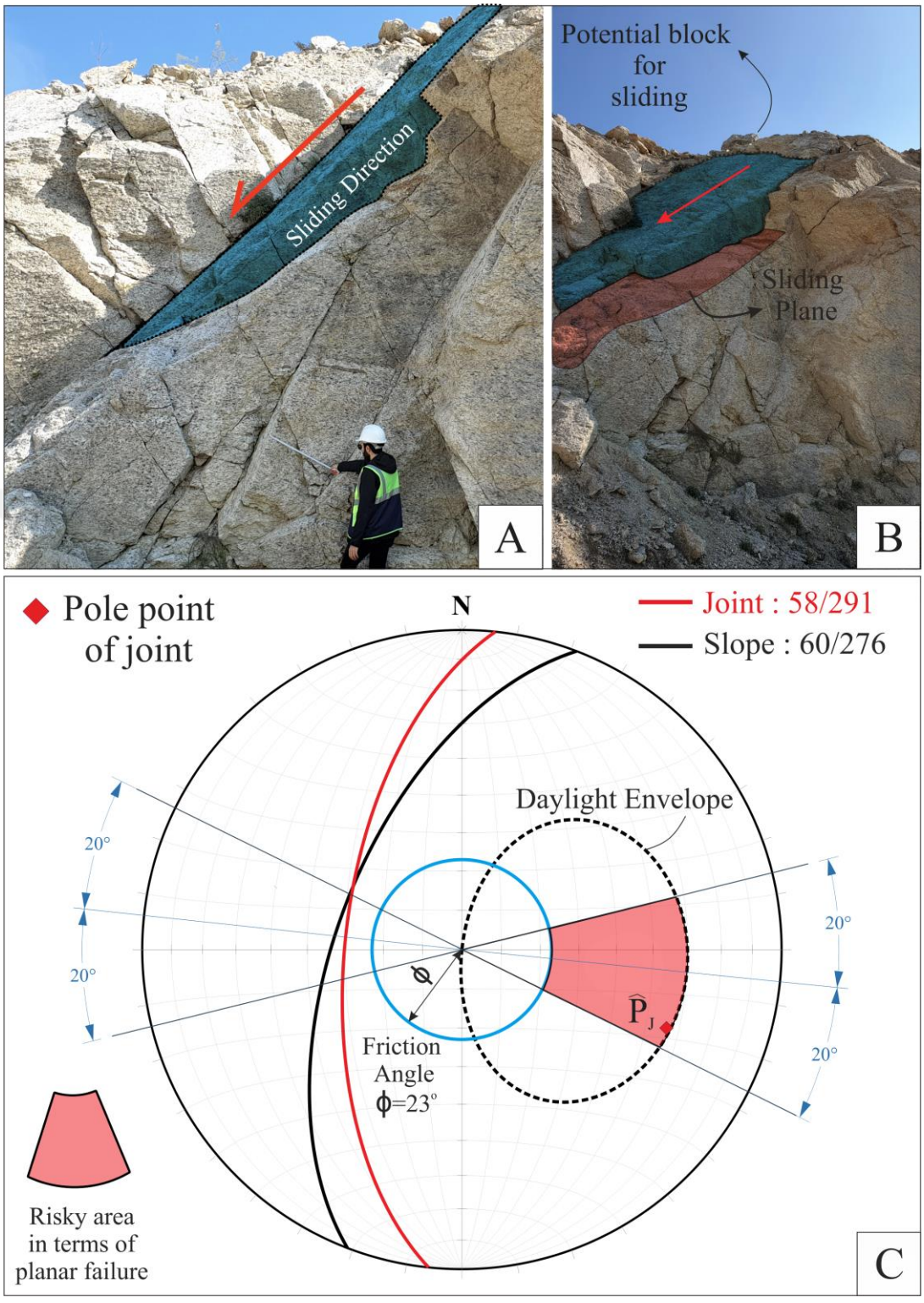

Figure 6.5 Planar sliding failure caused by joints; (A) The view of the sliding in the field and the direction of the sliding, (B) The block and sliding plane that is likely to sliding, (C) Kinematic analysis of the planar failure

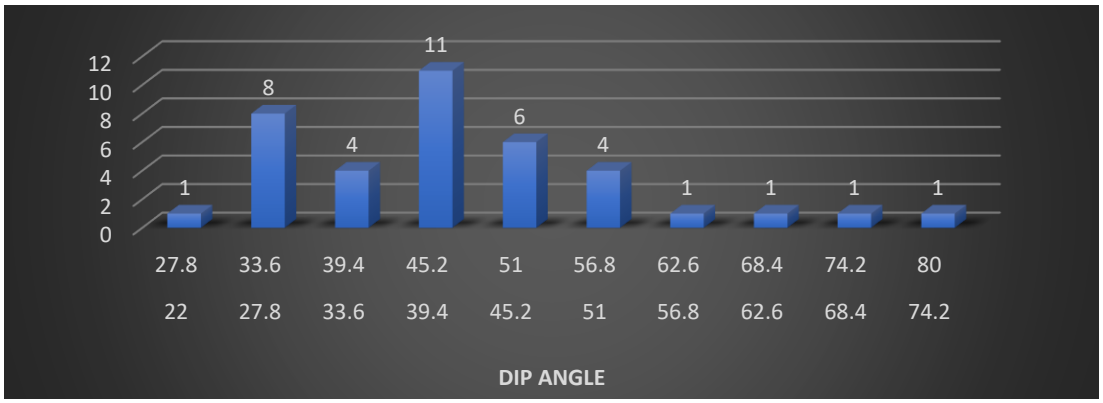

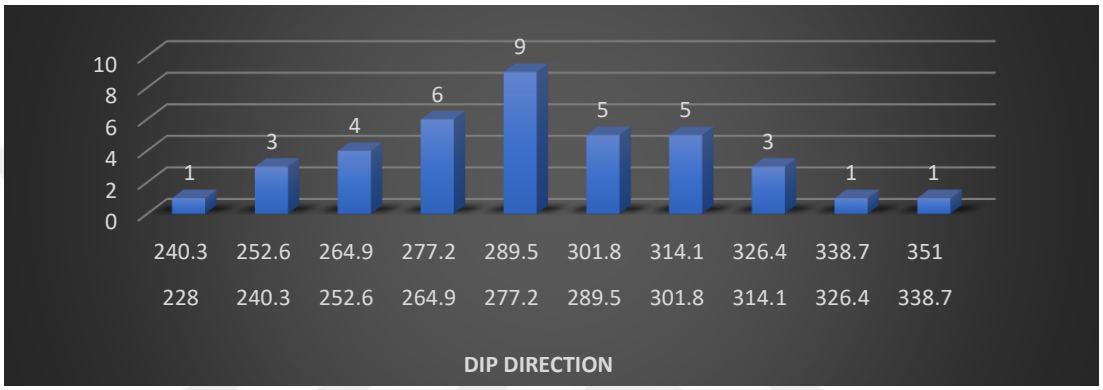

Figure 6.6 Graph showing the angular distribution of the orientation of discontinuity planes (joints) causing planar sliding

6.1.3 Wedge Type Sliding Failure

Wedge sliding is characterized as a special type of planar sliding. In fact, 39 of the slopes with 72 wedge failure potential also have planar sliding potential. This type of sliding is a type of failure that occurs with the sliding of the wedge block along the cross-section line formed by two intersecting discontinuity planes on the slope. As with planar shear, certain geometric conditions must be met for this type of failure to pose a potential hazard. These conditions are;

1. The slope angle of the slope must be greater than the dip angle of the line of intersection of the planes forming the wedge ($\alpha_{slope} > \psi_{intersection}$).

2. The plunge angle of the intersection line of the wedge must be greater than the average of the internal friction angles of the planes forming the wedge ($\psi_{intersection} > \phi$).

According to the kinematic analysis results of discontinuity measurements taken in the eastern part of the open pit, a total of 72 wedge-type sliding failures were

determined. These wedge-type mass movements determined by the kinematic analysis technique, as well as the analytical technique, were calculated with the help of the formula given in Equation 1 (Wyllie & Mah., 2004). According to the result of this factor of safety (FS) calculated by analytical method, 14 of 72 wedge-type sliding were determined as stable (Fs>1) and 58 as unstable (Fs<1). The thematic presentation of these identified areas is shown on the map in Figure 6.7. As seen in this map, old stream beds limited the stability of wedge failures. In other words, wedge-type failures on the lines of old stream beds are generally stable.

$$FS = K.\frac{tan\phi}{tan\psi i}, \qquad FS = \frac{\sin\beta}{\sin\varepsilon/2} . \frac{tan\phi}{tan\psi i} \tag{6.1}$$

Here, β: angle (degrees) between the linear element passed through the midpoint of the poles of the wedge-forming planes and the point where the low-inclined plane intersects the outer circle of the stereonet, ε/2: half of the angle (degrees) between the poles of the wedge-forming planes, ϕ: internal friction angle (degrees), ψi: plunge angle of the wedge (degrees).

Some of the K Factor and safety coefficient (FS) results calculated by analytical method on these 72 wedge failures are given in Table 6.2. The entire data set is presented in Appendix 3.

Table 6.2 K factor and FoS calculated using Equation 1

Location	K Factor	FoS	Status
8	2.60	1.771	Stable
18	0.18	0.170	Unstable
20	1.07	0.702	Unstable
30	3.82	3.187	Stable
32	2.83	1.854	Stable
37	0.26	0.230	Unstable
68	0.684	0.334	Unstable
73	0.07	0.065	Unstable
74	0.28	0.124	Unstable
81	1.61	0.879	Unstable
85	0.11	0.075	Unstable
97	3.54	1.506	Stable
108	1.43	0.702	Unstable
119	0.93	0.357	Unstable

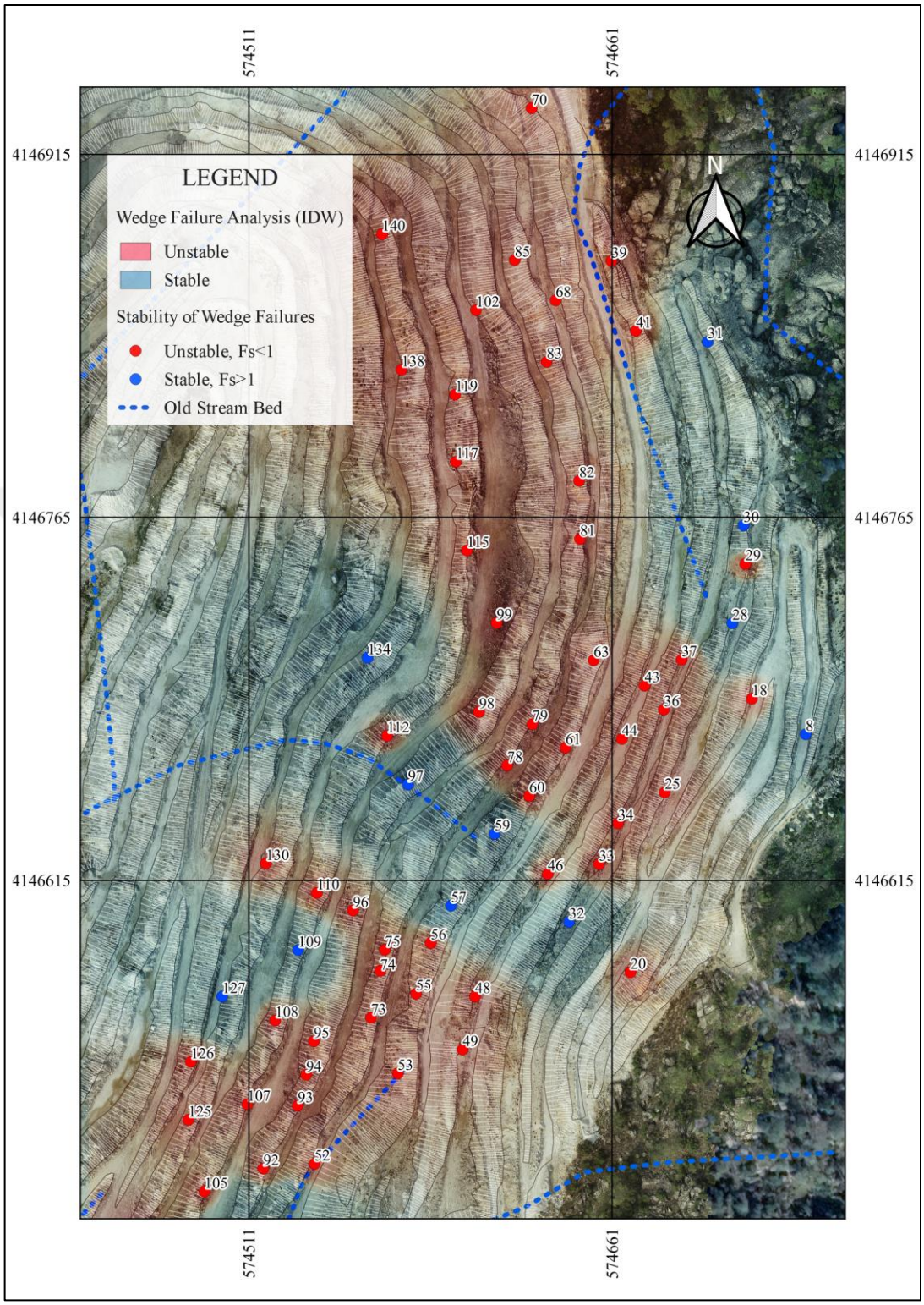

Figure 6.7 The safety factor calculated using the analytical method of wedge-type failures, their stability and their relationship with old stream beds

The field view and kinematic analysis of an example of 74 wedge-type failures seen in the study area are given in Figure 6.8.

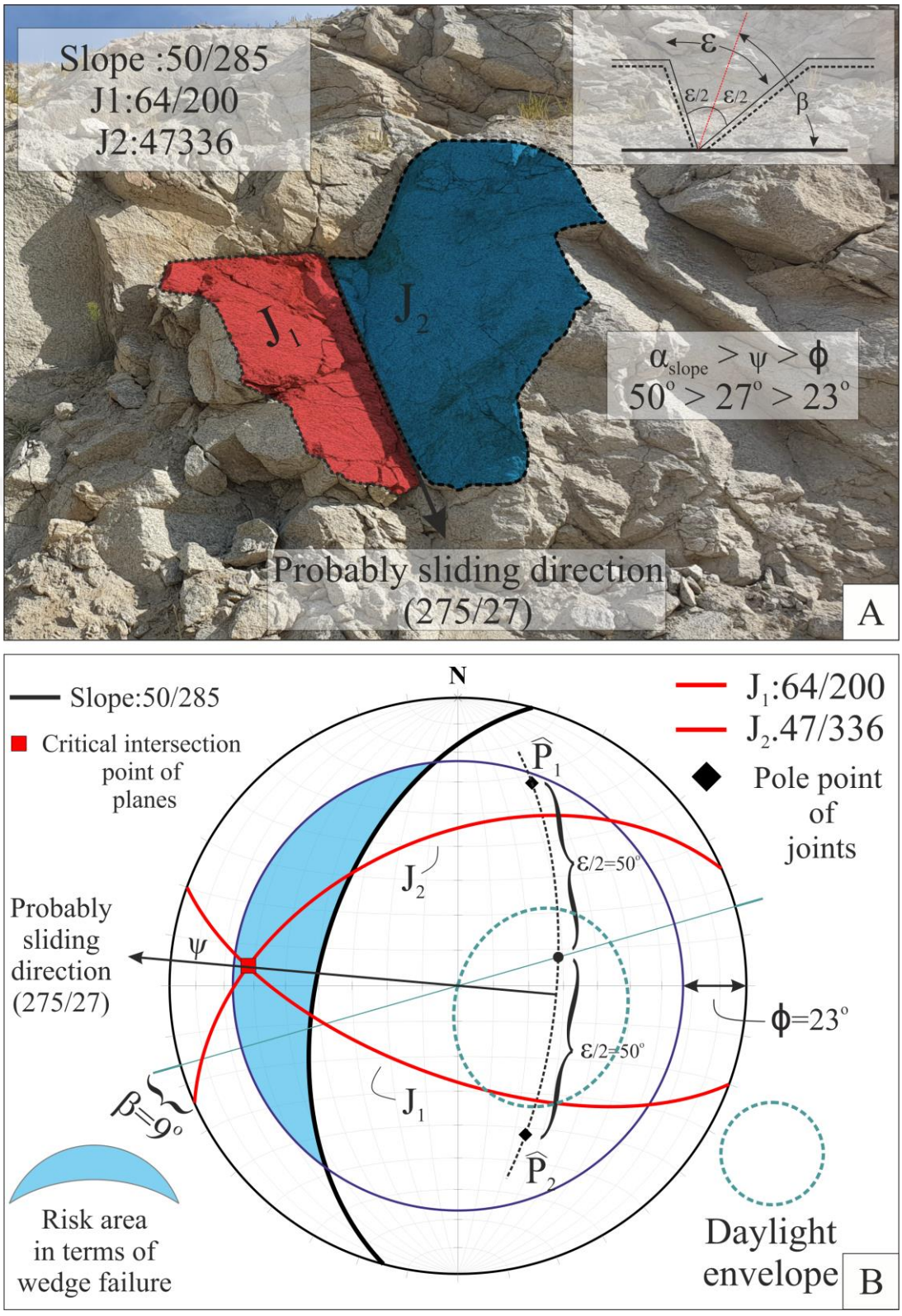

Figure 6.8 Wedge type sliding failure, (A) View of planes forming the wedge in the field, (B) Kinematic analysis of wedge type sliding failure

Analytical analysis of wedge-type shear failure using Equation 1 with the values shown on the stereographic projection in Figure 6.8 is given below;

$$FS= \frac{\sin\beta}{\sin\varepsilon/2} \cdot \frac{tan\phi}{tan\psi i},\ FS = K.\frac{tan\phi}{tan\psi i} \quad (6.1)$$

$$FS= \frac{\mathbf{sin9}}{\mathbf{sin50}} \cdot \frac{tan23}{tan27},\ FS= \frac{\mathbf{0.15}}{\mathbf{0.76}} \cdot \frac{0.42}{0.50} \quad (6.2)$$

$$Fs=0.170$$

According to this solution, the factor of safety (Fs) was calculated as 0.170. When this factor is taken into account, this slope is not safe in terms of wedge-type sliding failure, since Fs<1.

Wedge type sliding failures determined by kinematic analysis technique in the benched slopes in the eastern part of the open pit were examined within the framework of angular relations as in other sliding types. The divergence and direction of the intersection point of these planes forming 72 wedges were determined as 268/51. Likewise, the average orientation of the slopes where wedge failures occur was determined as 51/286. The result of the kinematic analysis using all these planes forming the wedges and the average slope angle is given in Figure 6.9.

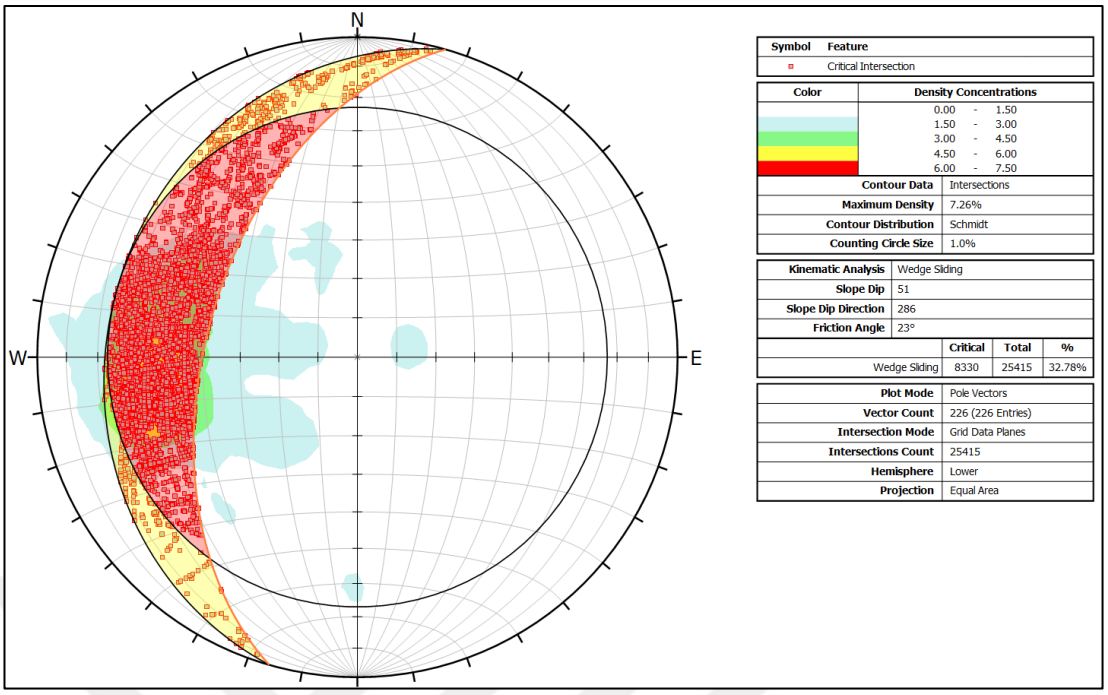

Figure 6.9 Kinematic analysis of wedge type sliding using all planes forming the wedge and mean slope orientation

6.1.4 Toppling Type Failure

Similar to planar and wedge sliding failure, the first step in the analysis of toppling failures is kinematic analysis, which is one of the important elements of structural geology to determine potential toppling conditions. (Wyllie & Mah, 2004). Toppling failure can be defined as a mass movement formed by high-angle discontinuity planes inclined into the slope (Goodman & Bray 1976). As indicated in Table 2, the discontinuity angles in the clustering analysis made with discontinuity measurements taken in the study area are mostly high angles, and the toppling failures with a 45% slice determined by the kinematic analysis technique (a total of 98, 54 flexural and 44 direct toppling) has proven to be too much. Some of the images of these slopes, which usually contain high angle discontinuity planes, are also seen in the oblique angle aerial photograph given in Figure 6.10. In this section, toppling failures will be presented in two subheadings. These; It is a flexural toppling mechanism in which one discontinuity plane is sufficient for toppling to occur, and a direct toppling (blocky toppling) mechanism in which two discontinuity planes that intersect each other perpendicularly and/or vertically are required for toppling to occur. The thematic map showing the

types of rollover failures observed in the study area and their distribution in the field is presented in Figure 6.11.

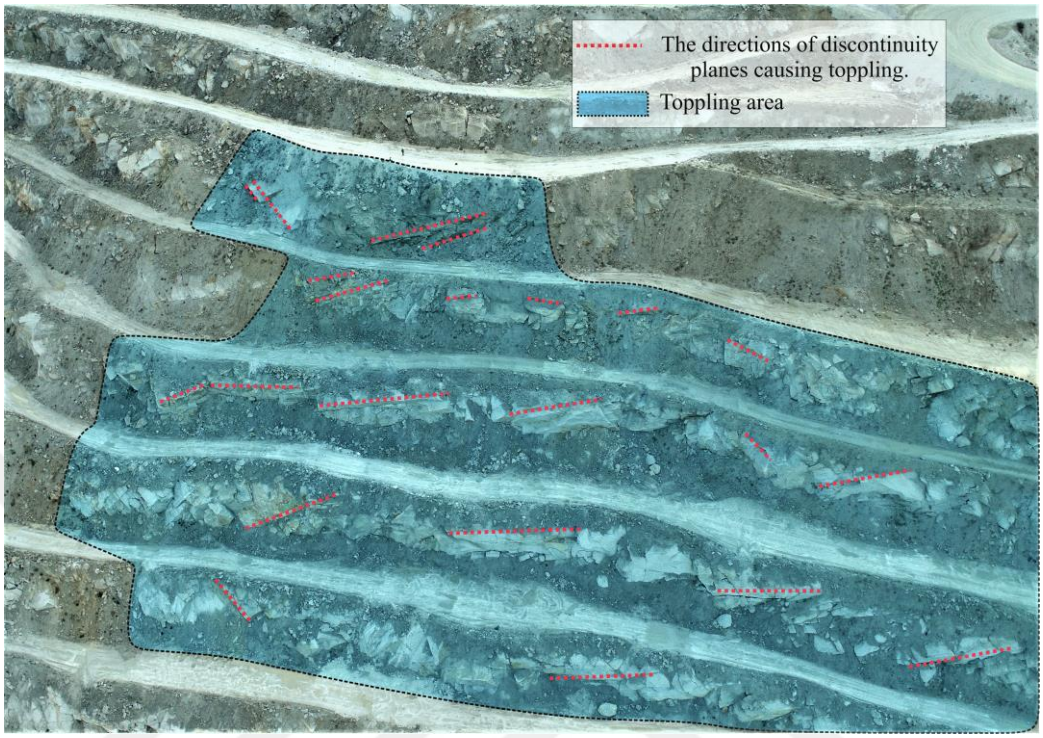

Figure 6.10 Generally the directions of high persistence and high angle discontinuity planes that caused toppling failures (Personal archive, 2021)

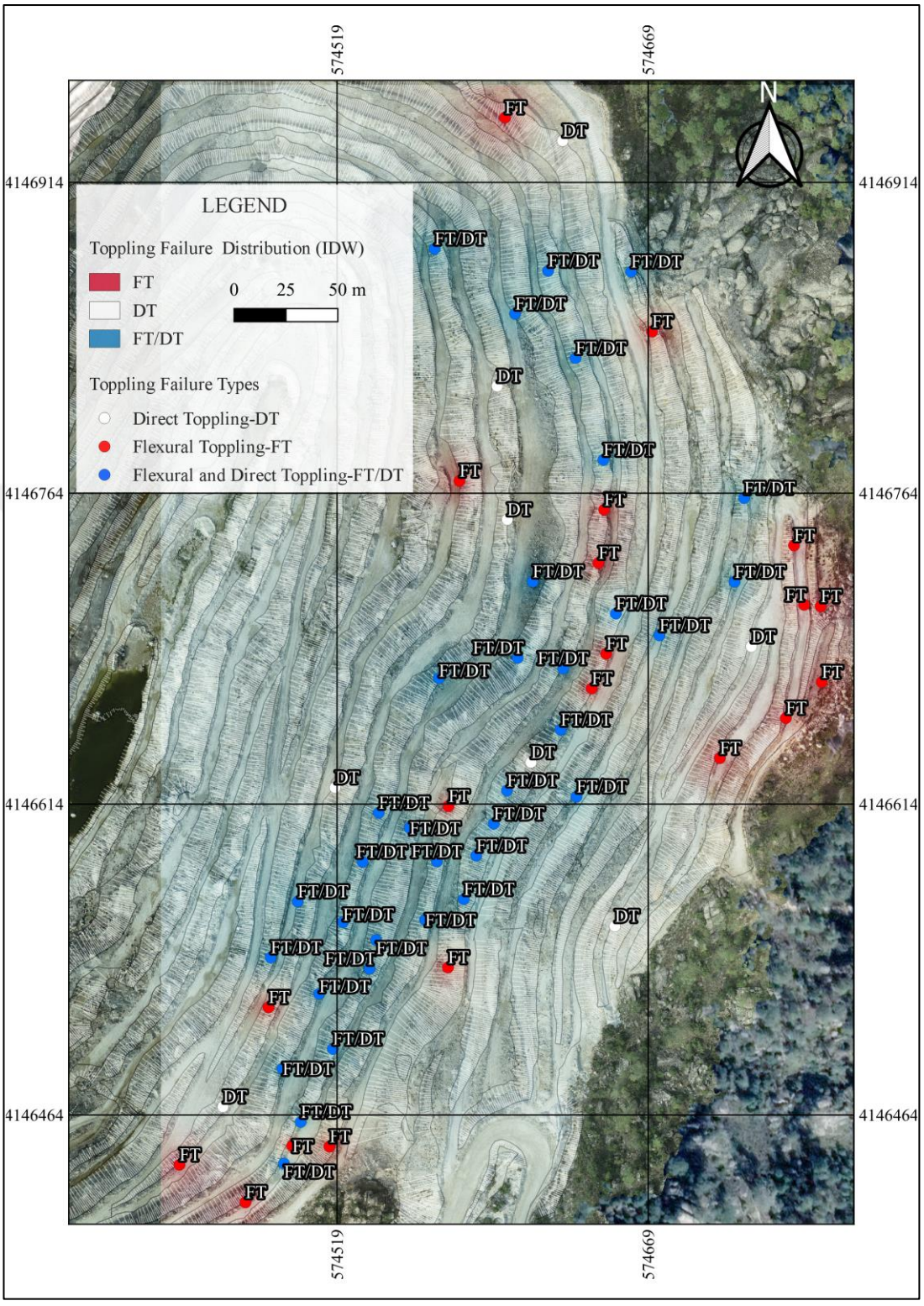

Figure 6.11 Distribution of types of toppling failure in the working area

6.1.4.1 Flexural Toppling

In this sub-title, flexural toppling is mentioned. In this toppling type, as in other sliding failures, the orientation of the discontinuities and the internal friction angle of the discontinuity plane are handled. Some geometric conditions must meet for this toppling -type failure, caused by high angled discontinuity planes inclined into the slope, to pose a potential hazard. These are;

1. There should be a difference of ±20o between the direction of the slope surface and the direction of the discontinuity planes.

2. The pole of the high-angle discontinuity causing the rollover must be within the dangerous area for the rollover failure on the stereonet.

3. $(90 - \alpha) \leq \beta - \phi$ equality must be satisfied (Bostancı et al., 2018).

The toppling mechanism formed by the high angle discontinuity planes inclined into the slope and the kinematic analysis of this failure type using the lower hemisphere projection are given in Figure 6.12. It has been determined that flexural toppling type toppling failure can occur in this slope, which is analyzed using stereographic projection technique. It is also seen that this toppling failures also satisfies Equation 6.3 below.

$$(90 - \alpha) \leq \beta - \phi \tag{6.3}$$

Here, α: dip angle of the discontinuity (degrees), β: dip angle of the slope (degrees), ϕ: internal friction angle of the discontinuity (degrees).

- For J_1;
  - α=72, β=60, ϕ=23
    - (90-72) ≤ 60-23
    - (18) ≤ 27
- For J_2;
  - α=81, β=60, ϕ=23
    - (90-81) ≤ 60-23
    - 09 ≤ 27

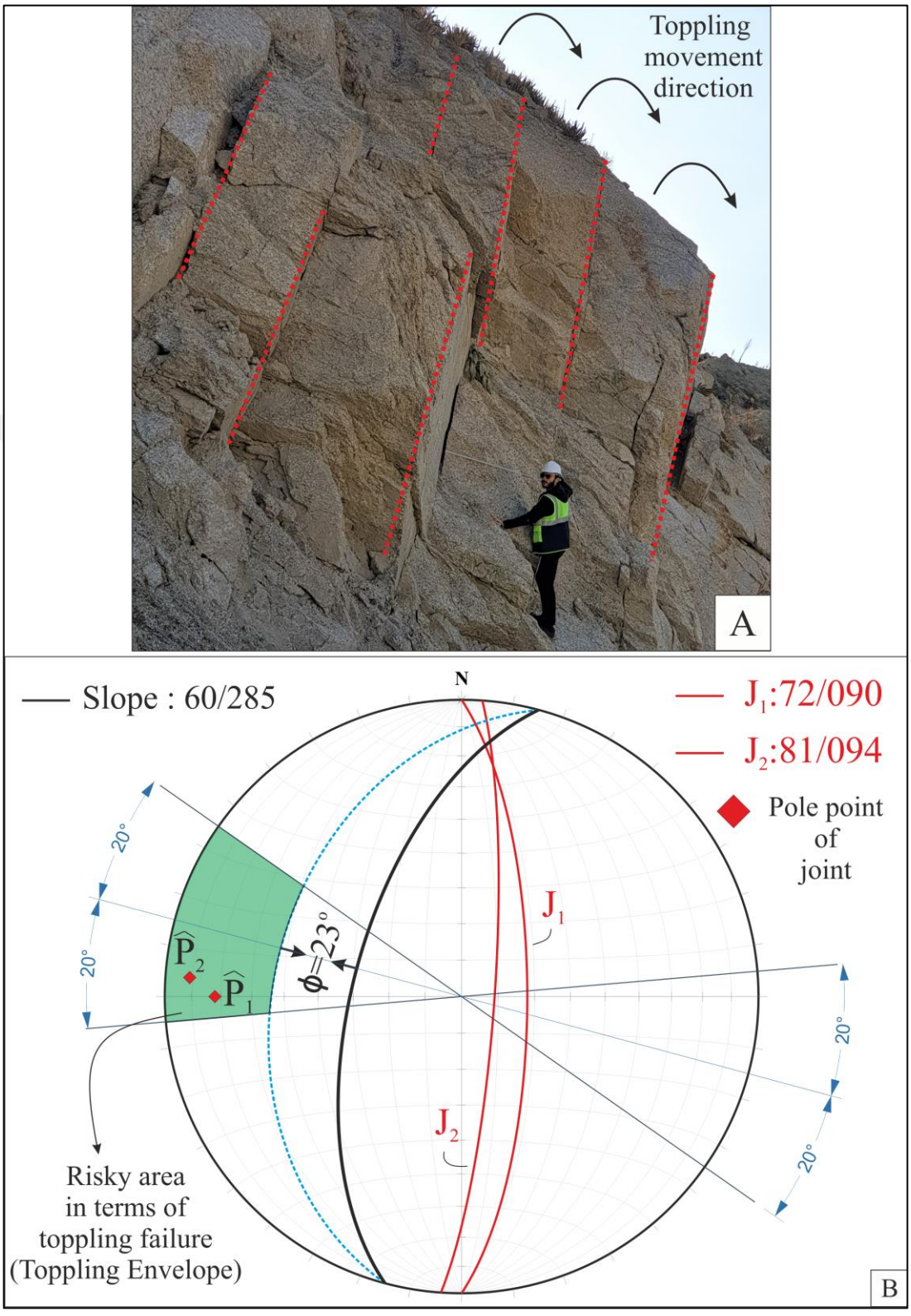

Figure 6.12 Flexural toppling failure; (A) High angle discontinuities and possible toppling blocks in the field view, (B) Kinematic analysis of flexural toppling failure

6.1.4.2 Direct Toppling

Direct toppling type failure is also called block toppling. The existence of a single discontinuity plane is not sufficient for a block type toppling failure to occur. Two sets of discontinuities intersecting each other perpendicularly and/or vertically are required for such a toppling to occur (Hudson & Harrison, 1997). An example of this type of failure in the study area, which poses a potential hazard with the presence of high-angle discontinuity planes containing mostly orthogonal joint sets, is given in Figure 6.13.

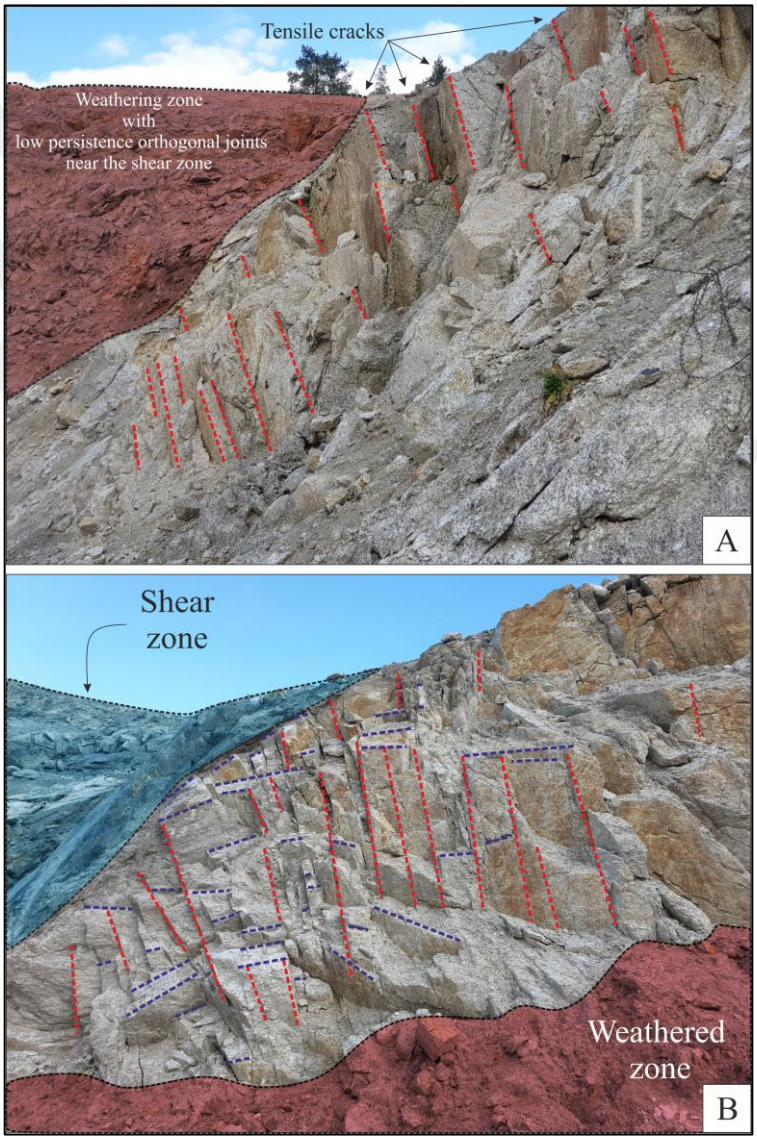

Figure 6.13 Direct toppling field view; (A) High angle discontinuity planes, (B) Sets of discontinuities perpendicular to each other (front view of A)

The kinematic analysis of the block toppling type failure caused by the presence of orthogonal joint sets is given in Figure 6.14.

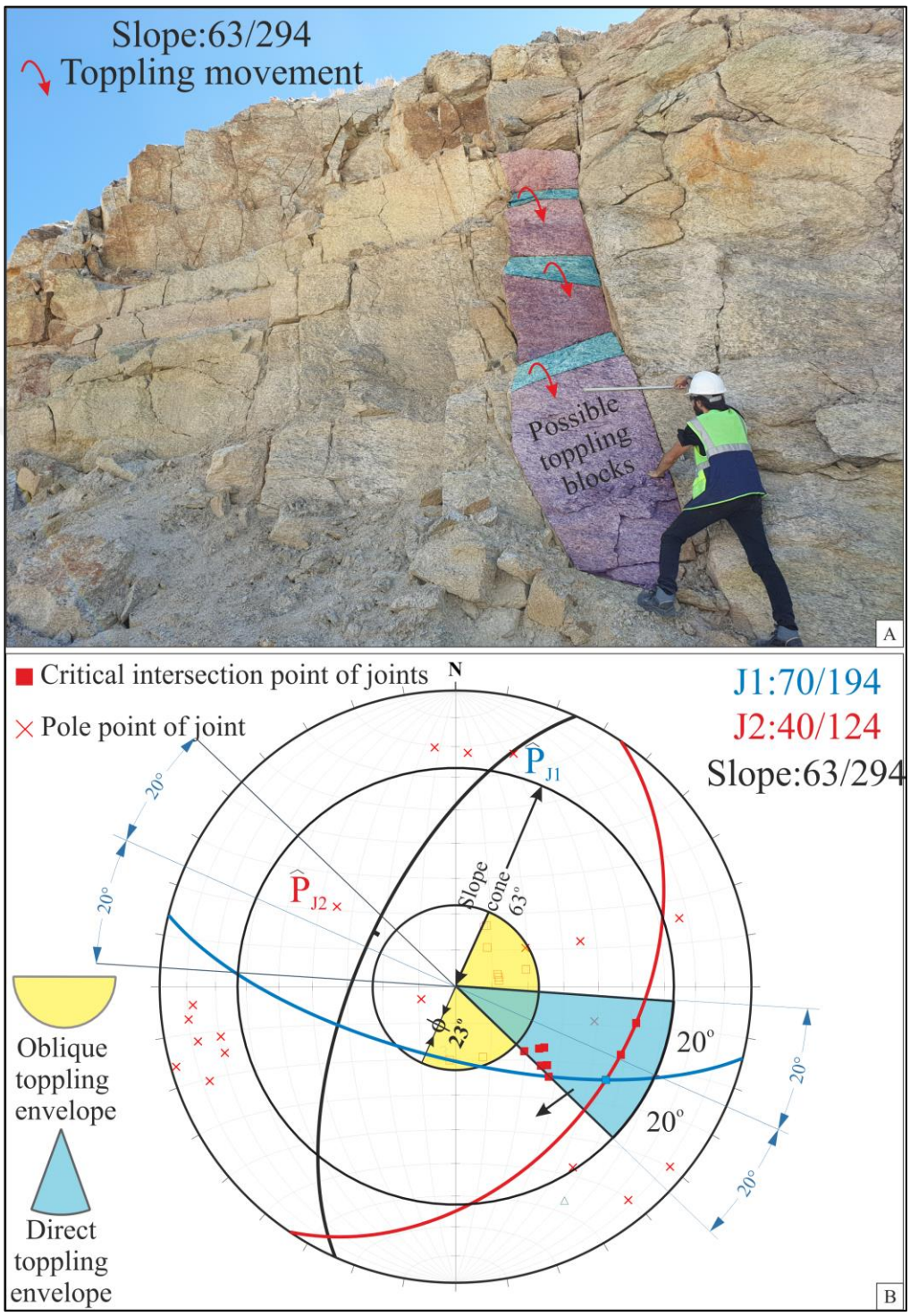

Figure 6.14 Direct toppling type failure; (A) Blocks formed by sets of joints perpendicular to each other, (B) Kinematic analysis of direct (block) toppling type failure

In the kinematic analysis given in Figure 6.14; Areas highlighted in yellow and light blue attract attention. There are two different failures envelopes on a stereographic projection. In the kinematic analysis of this failure type, an equal angle polar stereonet network can also be used instead of the equal area lower hemisphere Schmidt network.

The kinematic analysis is performed by considering the intersection points of the discontinuity sets that cross each other in the area highlighted in blue (it is the primary critical region for Direct toppling). The intersection points falling in this area represent the risk of toppling blocks. The outer boundary of this area, highlighted in blue, is given by a circle equal to the slope angle (Slope cone). This circle defines an upper limit for toppling -type failure and ensures that the angle between the slope surface and the toppling blocks is always less than or equal to 90o. The boundary of the other envelope in the blue region is the friction cone of the base planes. This cone has no direct relationship with the critical intersection points. However, it is used to define a sliding or non-sliding release mode for base planes. In other words, in the kinematic analysis, the internal friction angle has no effect on the direct topping failure.

In the center of the street, the inner friction circle is limited and the yellow highlighted area is defined as a toppling envelope for oblique toppling. For this region, kinematic analysis is performed with the intersection points, as in the direct toppling failure. Within the scope of this thesis, only flexural toppling and direct toppling issues were mentioned and kinematic analysis of these toppling types was made.

When the angular relationships of the discontinuities (both flexural and direct toppling) that cause toppling failures are examined, the average orientation of these discontinuity planes is determined as 75/093. It was seen that this determined mean discontinuity orientation belongs to the Set 1 system specified in Table 2. In the kinematic analysis, the average orientation of the slopes where these toppling failures (both flexural and direct toppling) were determined was determined as 50/285. The angular distributions of these discontinuities are presented in the graph in Figure 6.15.

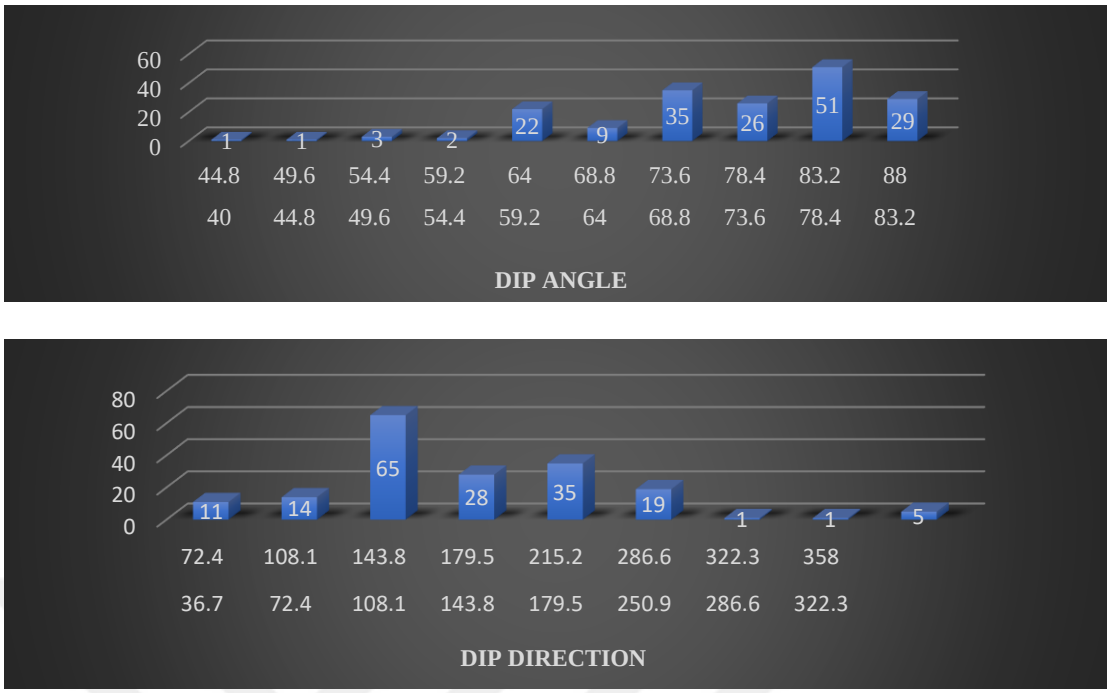

Figure 6.15 Angular scatter plot of discontinuity planes that cause toppling failures

CHAPTER SEVEN

REMOTE SENSING

Remote sensing; It can be defined as the technique of examining, evaluating and recording the earth, the objects on the earth and earth resources without physical connection. In this section, the remote sensing study conducted within the scope of the thesis is mentioned. Although there are many branches of remote sensing, unmanned aerial vehicle and photogrammetry technique will be mentioned under this main title and sub-titles.

7.1. UAV Survey

Before carrying out geological observations and field studies in the study area, a specially produced unmanned aerial vehicle was used for mapping with rotary wing RTK (Real Time Kinematic) system. With this UAV used, aerial photographs were taken with a camera angle of -90 degrees (Nadir) at the borders of the work area from a height of 100 meters with a 70-80% overlap. The flight plan of this measurement made in the study area is given in Figure 7.1 and the flight parameter details are given in table 7.1.

Figure 7.1 Flight plan of the worksite in the GS RTK app on the Phantom 4 RTK's onboard display controller.

Table 7.1 Parameters and details used in measurements made with the Phantom 4 RTK

UAV Type	Rotary Wing (Drone)
Flight Plan	Autonomus
Camera Resolution	20 Mgpx
Overlapping*	%70-%80
Flight Height (AGL)**	100 m
Camera Angle	-90 Degree (Nadir)
Flight Mode	2D Photogrammetry
Position System	RTK
Solution	Fixed

**: Horizontal and Vertical Overlap, respectively.*

***: Above Ground Level*

The fact that the system is equipped with RTK ensures that the coordinates at the midpoints of the aerial photographs are more accurate and precise. By using 3D Survey photogrammetry software with these aerial photographs; dense point cloud, textured mesh model, digital elevation model and orthophoto were created. These data were used throughout the study. The production of these data is explained in detail under the heading Photogrammetry.

7.1.1 Photogrammetry and Process

If we explain the term photogrammetry in general; It can be defined as the method of measuring objects over photographs (terrestrial or aerial photogrammetry) and the metric interpretation of the data in the image. As a technical term; It is the measurement of two- or three-dimensional objects through photographs. In this study, many data types were obtained from aerial photographs obtained with coordinates. In this study, these data were produced by SfM photogrammetry technique. SfM; It is a photogrammetry technique that produces a new type of data with a stereo image technique, which aims to create 3D images and various models in images taken in 2D, called Strain from Motion (Çelik, 2020). The use of 3D Survey software to create the data types described above and the process steps are given below.

1. Uploading Photos

2. Alignment Photos

3. Balancing (Orientation / Bundle Adjustment)

4. Sparse Point Cloud

5. Density Cloud

6. Textured Mesh Model (3D Grid Model)

7. Orthophoto (Classic / Traditional or True Orthophoto)

8. Export Options

While the UAV with RTK is measuring in the air (horizontal and vertical overlay photo taking stage), it is connected to the internet with the M2M type data sim card modem in the remote. This internet connection receives location correction information by connecting to fixed GNSS stations in "TUSAGA ACTIVE CORS" center. These received location (coordinate) corrections are instantly transferred to the UAV using a 2.4GHz connection with Ocu-Sync technology. Thus, the drone writes these coordinates in EXIF format with high accuracy and precision to the midpoints of the aerial photographs during the measurement. Afterwards, EXIF information is read from the photos transferred to the 3D Survey program and it aligns (merges) the photos taken with overlay. After the photos are transferred, it is important to choose the coordinate system where the project will be resolved. The modem in the control connected to the TUSAGA CORS system receives the correction information over the 3-degree ITRF 96 (International Terrestrial Reference Frame, GRS 1980 Ellipsoid) coordinate system. Therefore, in order not to increase the margin of error due to transformations between coordinate systems and not to cause irregularities, the coordinate system to which the project will be resolved should be chosen accordingly. While the project is being resolved; (for this study) TUREF/TM27 (EPSG Code:5253) was chosen. TUREF system; (Turkish National Reference Frame, GRS 1980 Ellipsoid). After these processes, the previously determined Ground Control Point in the field is included in the balancing process phase in order to increase the accuracy and precision of the solution. The coordinates of these GCPs are taken from the GNSS receiver in the above-mentioned system, and after several different readings are taken, the averages of these coordinates are taken and evaluated as a control point. The margins of error of these GCPs are given in Table 7.2.

Table 7.2 Accuracy of established Ground Control Points

GCPs	Accuracy
GCP -1	0.003 m
GCP -2	0.011 m
GCP -3	0.029 m
GCP -4	0.027 m
GCP -5	0.023 m
GCP -6	0.009 m
GCP -7	0.019 m

The sparse point cloud that occurs after the balancing process is completed shows that the operations made up to this step are error-free. Then, the step of creating a dense point cloud is started, and in this step, the density of this point cloud is selected according to the purpose of the study (Low, Very Low, Medium, High and Very High).

After the point cloud is formed, data in raster or vector data types containing geographic information such as digital elevation model, textured mesh model, contour and orthophoto are created. The characteristics of these data produced for this study are presented in Table 7.3 and their images are presented with different figure numbers below.

Table 7.3 Details of data generated during and/or after the photogrammetric process

Coordinate System	TUREF/TM27 (EPSG :5253)
Number of Photos	365 images
Flight Area	18.6 ha (186.000 m^2)
Number of Point (Point Cloud)	144.786.888 points
Grid Cell Size (DEM)*	0.15 m
Number of Triangle (Textured Mesh Model)	7.000.000 triangles
Resolution (Orthophoto)	20061x26379 pixels
GSD**	2.7 cm (for AGL:100 m)

*Digital Elevation Model

**Ground Sampling Distance; It shows the area that a pixel on the orthophoto represents on the earth. The higher the GSD value, the higher the resolution.

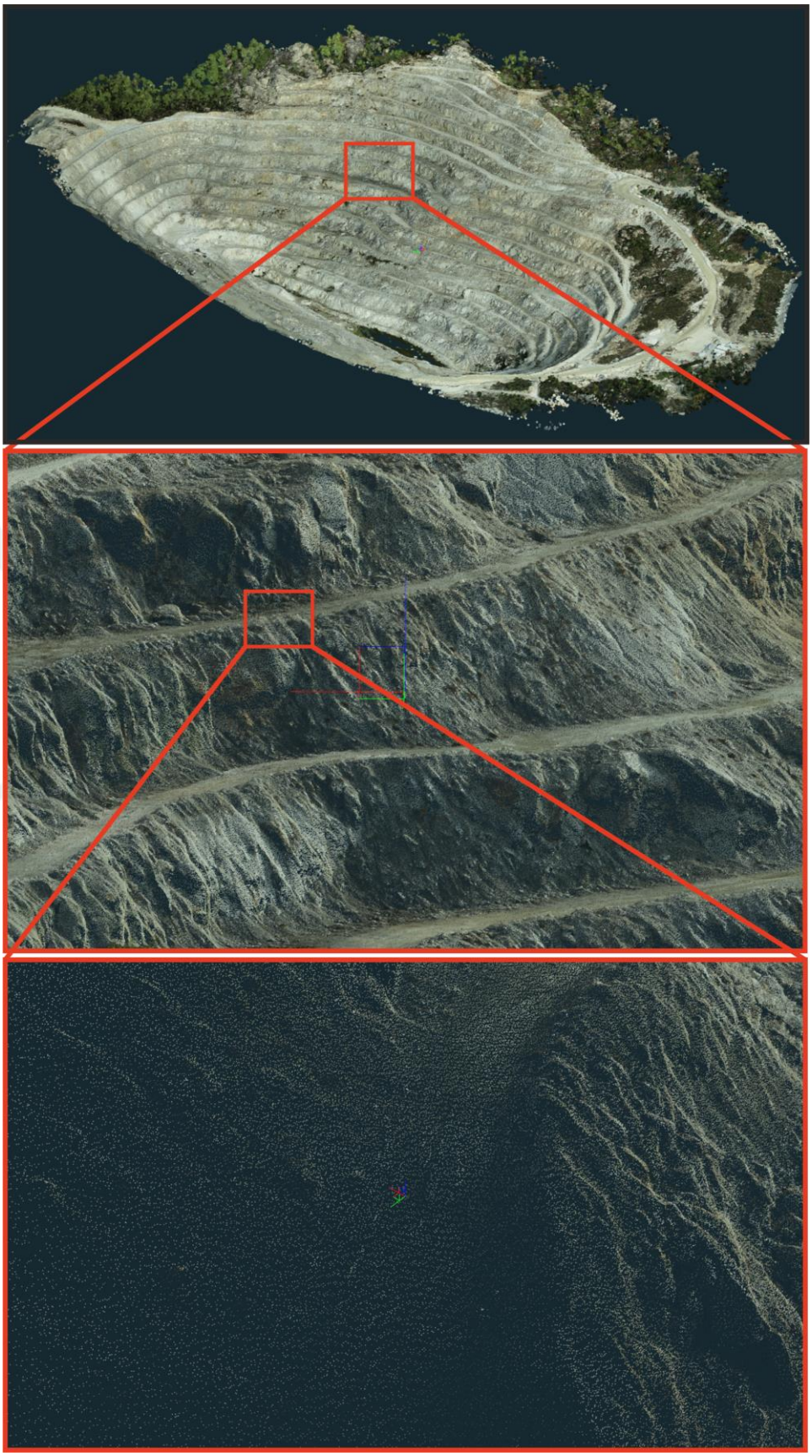

Figure 7.2 The "Dense Point Cloud" data model with 144,786,888 points and its detailing

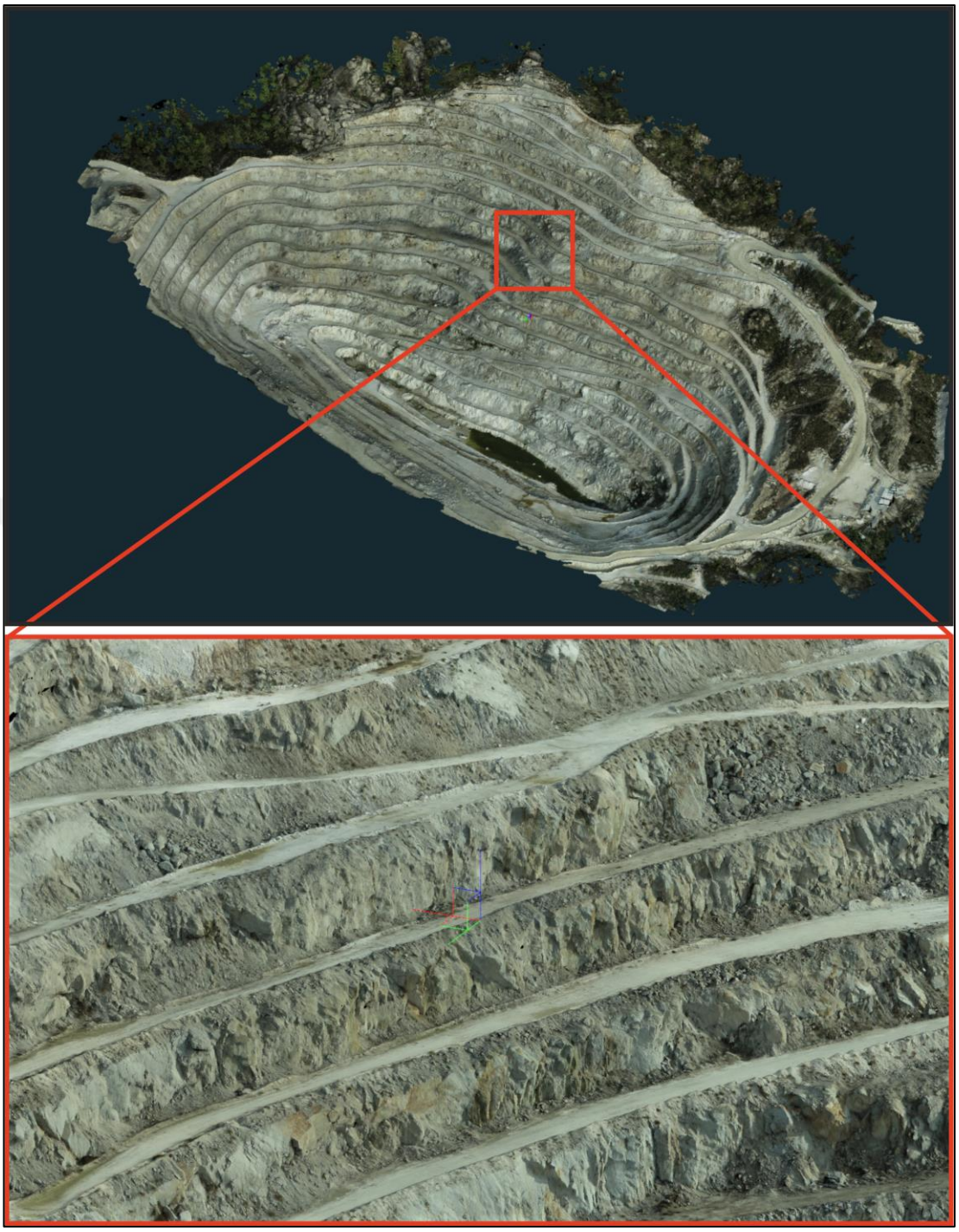

Figure 7.3 Textured mesh model created with 7,000,000 triangles and details from close-up view

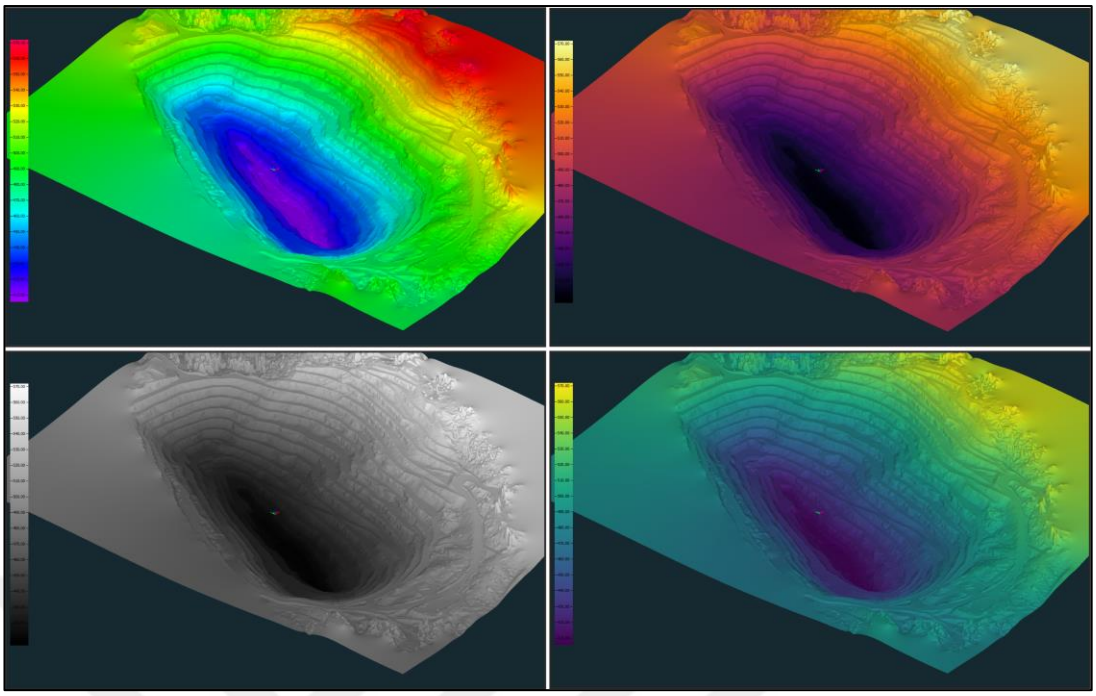

Figure 7.4 Digital elevation models (DEM) presented with different color palettes

After all these stages using 3D Survey photogrammetry software, the true orthophoto created by calculating from the 3D textured grid (mesh) model was transferred to the QGIS program. True orthophoto; It can be defined as the correct orthophoto created by using DSM (Digital Surface Model) by removing the irregularities and irregularities caused by the camera angles in the aerial photographs taken while the UAV is flying in the air. It is seen that this true orthophoto which is mentioned with the Google Satellite Hybrid image opened as a base in the QGIS program, overlaps exactly. These models and data types, whose location accuracy is proven with GCPs, are also shown as evidence of this overlap, which is described in the map shown in Figure 43.

It should be kept in mind that the image may appear as if it is not fully seated on the substrate due to the scarcity of overlaying aerial photographs at the boundaries of the formed orthophoto. However, high overlapping rates, correct reading of GCPs and participation in the process, and continuous "FIXED" verification of the UAV during flight also support position accuracy. In Figure 7.5, the edges of the orthophoto are zoomed in and this accuracy is seen in the close view.

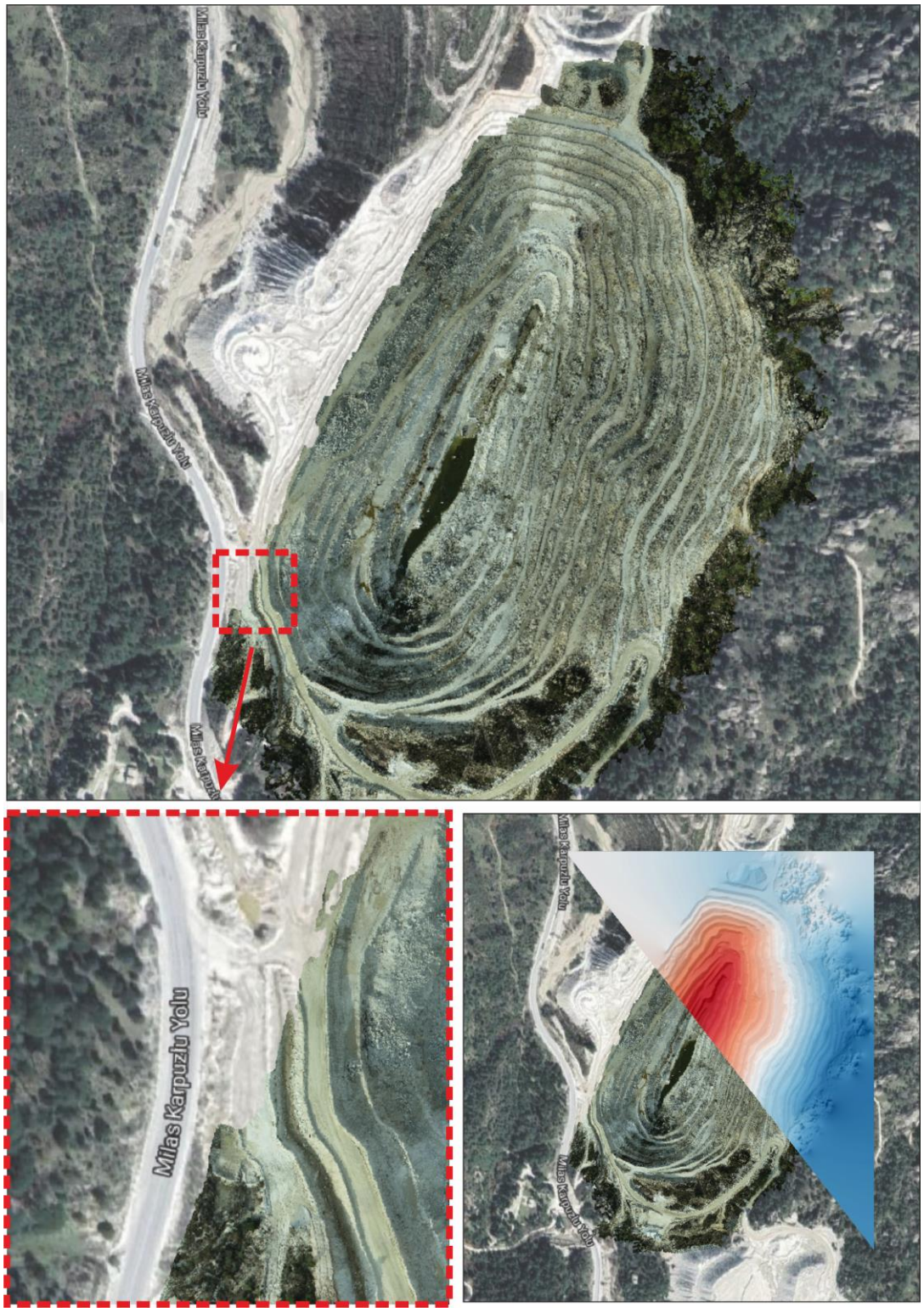

Figure 7.5 Proof of true orthophoto and digital elevation model fit on Google Satellite Hybrid image and positional accuracy

7.1.2 Kinematic Analysis

By addressing all these, the main subject of the study will be explained in this title and in the sub-titles under this title. In line with the purpose and scope of this study, the dense point cloud produced in 3D Survey photogrammetry software was then transferred to Cloud Compare v2, an open-source point cloud processing and imaging software. As explained in the title “5.1 Kinematic Analysis”, in order to perform kinematic analysis, the orientation of the slopes and discontinuity planes on which the kinematic analysis will be performed must be known. As explained in the previous sections, the production was interrupted due to the instabilities that occurred before in the field where the study was carried out. Therefore, the eastern part of this open pit, where activities such as production, blasting and excavation are suspended, is still considered as a potential hazard area.

In the first stage of the study, it was aimed to measure the slope angles and the orientation of the discontinuity planes at all 140 points determined as observation points. However, due to the absence of a discontinuity plane parallel to the slope surface and the slope geometry deteriorated due to blasting and weathering, the slope angles could not be measured accurately and accurately. It is planned to obtain these angles in a different way in order to save time spent both when the site is dangerous and when measuring slope angles.

As a solution to this situation; Since dip angle/dip direction information is provided by the “Compass” plugin of the desired surface in Cloud Compare program, it is aimed to use this method. In order to both prove the accuracy (sensitivity) and test the usability of the method of obtaining slope orientations by measuring through this program, measurements were made at some observation points with both the Brunton type geologist compass and the "Compass" plugin in the Cloud Compare program. The results of these measurements are given in Table 7.4.

Table 7.4 Comparison of slope orientations measured with Brunton type geologist compass and Cloud Compare program Compass plugin

Measurements in Field	Cloud Compare Compass Plugin
48/285	49/287
56/273	56/275
48/279	50/280
59/296	60/295
55/290	57/290
40/299	40/300
45/296	45/295
42/270	40/273
60/285	60/287

Based on the results given in Table 7.4, all slope orientations have been made with the Compass plugin in the Cloud Compare program to save time by shortening the working time and to avoid being in the dangerous area.

Just as in measuring slope orientations, some problems were encountered in measuring discontinuity planes. Since MW-HW and/or HW type weathering is effective throughout the open pit, the orientation of the discontinuity planes on the slope tops and/or in the regions close to the slope top could not be measured due to the talus (clastic rock pile/deposit) formed at the bottom of the slopes. As a solution to this situation, the Cloud Compare program was applied as in the slopes. And in the same way, the Compass plug-in was tested on the slope numbered 11, and kinematic analysis was performed again. This test and the kinematic analyzes made using the said plugin are given in other subheadings under this title.

7.1.2.1 Planar Sliding Failure

In this chapter; The kinematic analysis of the slope (planar sliding caused by the foliation planes at the observation point 11) was performed using the Compass plug-in in Cloud Compare software, with the kinematic analysis described under the heading “5.1.2 Planar Sliding Failure”. The orientation of the slope and discontinuity plane, taken in the field with a Brunton type geologist compass, was measured as 48/309 and 40/310, respectively. When kinematic analysis was performed with the Dips V7.016 (2019) software with these discontinuity orientations, it was determined that planar sliding failure could occur and pose a potential hazard. In these

measurements made with the Compass attachment on the same slope and on the same discontinuity plane, these measurements are respectively; It was measured as 47/309 and 41/309. With these measurements, it was determined that there is a dangerous slope in terms of planar sliding failure in the kinematic analysis performed with the Dips V 7.016 (2019) software.

By looking at these results, which are very close to each other, it was concluded that the compass add-on was successful in measuring the discontinuity planes. Screenshots of these orientations measured with the Compass plugin and the kinematic analysis using Dips V 7.016 (2019) software are given in Figure 7.6.

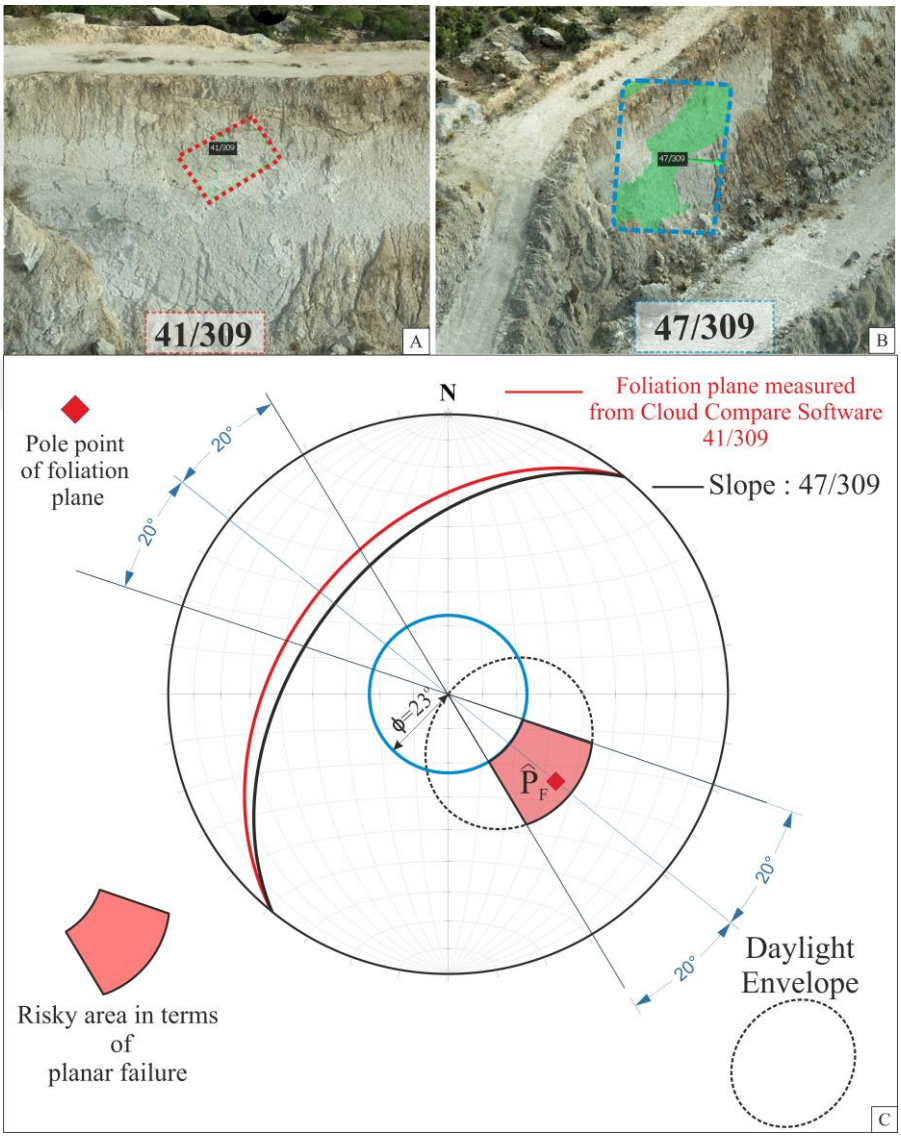

Figure 7.6 Planar sliding failure by remote sensing; (A) Foliation plane orientation, (B) Slope orientation (C) Kinematic analysis of planar sliding

7.1.2.2 Wedge Type Sliding Failure

Under this heading, the orientation of two discontinuity planes located very close to the top of the slope (approximately 8 m above the ground (berm) and intersecting could not be measured with the conventional method (Brunton type geologist compass). The orientation of the slope and intersecting discontinuity planes at this observation point, where a large wedge block formation is observed, was obtained with the "Compass" plug-in in Cloud Compare software. These obtained orientations were analyzed using Dips V 7.016 (2019) software and it was determined that they pose a potential danger in terms of wedge-type sliding failure. In addition, the K factor and the factor of safety (FoS) in this wedge failure were calculated and stated in Equation 7.1. The images and kinematic analysis of the software on the screen of these measurements are given in Figure 7.7.

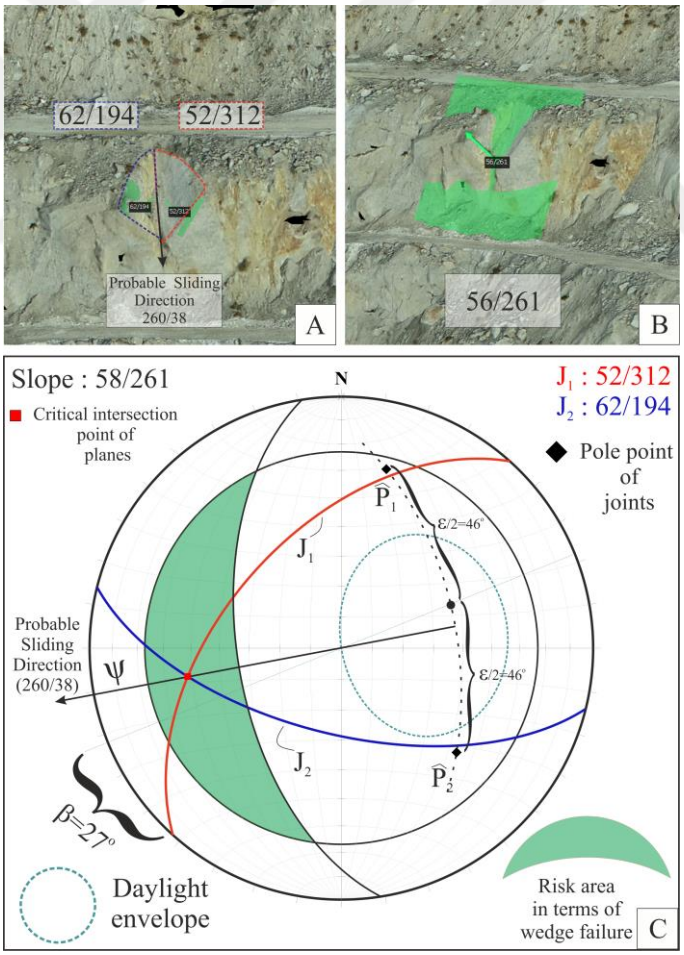

Figure 7.7 Wedge sliding failure with remote sensing; (A) Orientation of planes in the wedge block, (B) Orientation of the slope, (C) Kinematic analysis of wedge-type sliding

$$FS = \frac{\sin\beta}{\sin\varepsilon/2} \cdot \frac{tan\phi}{tan\psi i} \quad FS = K.\frac{tan\phi}{tan\psi i} \tag{7.1}$$

Fs=0.340

According to this solution, the factor of safety (Fs) was calculated as 0.340. When this factor is taken into account, this slope is not safe in terms of wedge-type sliding failure, since Fs<1.

7.1.2.3 Toppling Type Failure

It has been mentioned in the previous sections that toppling type failure occurs along discontinuity planes inclined into the slope. As a result of the kinematic analysis, the result of the highest number of toppling failures in the study area was given in the relevant section. As indicated in Figure 6.10, in most of the toppling regions highlighted by the blue area, high-angle discontinuity planes inclined into the slope are located close to the slope crests, just as described in the heading "7.1.2.2 Wedge Type Sliding Failure". In such a case, the measurement of these planes was carried out with the Compass add-on in terms of occupational safety and continuity of work. The discontinuity orientations and the kinematic analysis of toppling failure obtained by the Compass plugin are given in Figure 7.8.

As seen in the image given in Figure 7.8, the orientation of these discontinuities in the region close to the toppling region is quite similar to the orientation of the discontinuity planes in the toppling failure indicated in Figure 6.12.

It should only be noted that the planes of discontinuity required to analyze toppling-type failures slope into the slope. In this analysis, it can be considered lucky for us that there are easily visible (recognizable) discontinuity planes in the point cloud. In general, discontinuity planes inclined into the slope may go unnoticed and thus the orientation of the discontinuity planes may not be obtained.

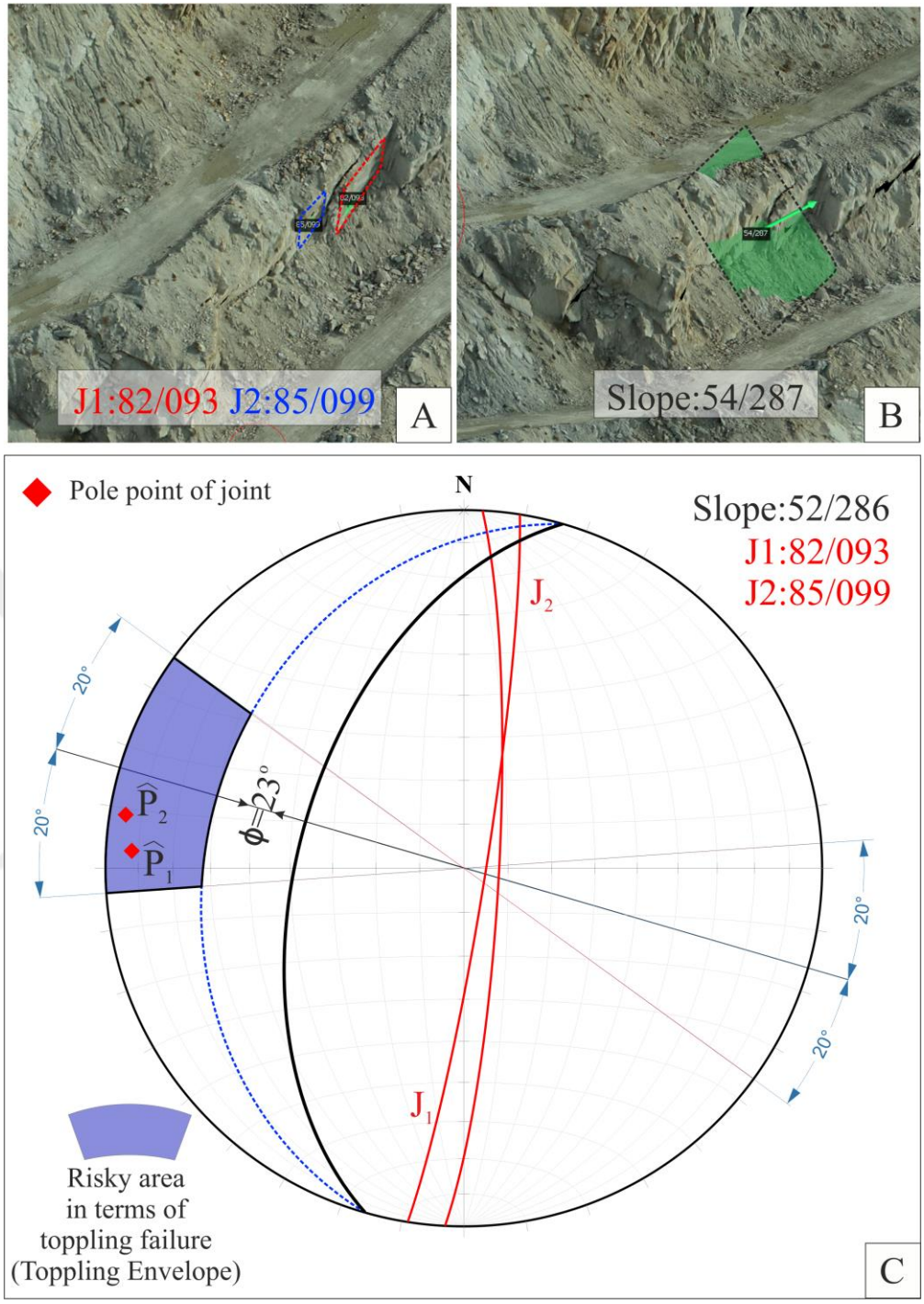

Figure 7.8 Toppling type failure (Flexural Toppling) with remote sensing; (A) Orientation of planes, (B) Orientation of the slope, (C) Kinematic analysis of flexural toppling type failure

7.2 GIS Applications

Under this title, there are analysis and interpretations of this study in the QGis program, which was mentioned in the previous title/sub-titles and thematic maps were

created in other sections. These mass movements, which are mentioned in Chapters X to x and determined by the kinematic analysis technique, are one of the main subjects of this study. In the eastern part of the open pit (problem side) there are many joint sets. These discontinuity planes, which have been formed due to various reasons such as tectonism, controlled blasting and load removal and have many different orientations, control many mass movements in the eastern part of the quarry. According to the results of the kinematic analysis made with the data obtained as a result of the geological/geotechnical observations made at 140 points, there is more than one mass movement in a slope.

That is, while only planar sliding failure was detected in some of the slopes at some observation points, in some slopes both planar sliding failure and direct toppling and wedge type sliding failure were detected. In this case, a special thematic map was prepared in the QGis program according to the number of mass movements determined, regardless of the type of mass movement detected in each slope.

This thematic map can be defined as a very satisfying and understandable display technique called the "HeatMap" technique, which is used to determine the concentration of the input point data with different color scales. This heat technique; It works based on a statistical-based algorithm called Kernel Density Estimation. The HeatMap technique is a study conducted in this study to determine the regions where the mass movements determined by the kinematic analysis technique in the eastern part of the open pit are concentrated (frequent) according to the number of mass movements determined at the observation points.

Figure 7.9 Concentrations of mass movements detected in the eastern part of Open Pit, produced using the heat map (Kernel Density) technique

CHAPTER EIGHT

ASSESSMENTS

If we evaluate the field studies and observations made in the summer period (Dry Period) in the study area; It has been determined that the eastern part of the Open Pit (the region where production is stopped) will be exposed to potential mass movements in large numbers. The weakening of the rock mass due to the moderate/medium-high degree of weathering of the geological rock units in the study area has prepared the environment for failures (slidings). Apart from weathering, as shown in Figure 3.1, the deformation of the surrounding geological units by the Karadere Shear Zone, which is located approximately parallel to the albite zone, where different mining operations are located, is one of the stability problems of this open pit. It is thought that the Yarenalan Fault, which is a high-angle normal fault with a slope of approximately 70 degrees in the study area, has a great effect on the formation of discontinuities in the open pit. In the kinematic analysis section, which is explained under the title of "Chapter Six", it is mentioned that the most dominant mass movements determined by the kinematic analysis technique in the open pit are the toppling type failures. It is a definite fact that these toppling type failures can occur along high-angle discontinuity planes, considering their geometrical relationship. That's why; The Yarenalan Fault with a high dip angle (approximately 70-80 degrees) is thought to play a role in the formation of high-angle discontinuity planes that cause toppling failure. It has been determined that the faults located close to the study area as in the map in Figure 3.1 and relatively far away as shown in Figure 3.3 are the structural elements that are primarily effective in the formation of the discontinuity planes and/or the increase in the number of these discontinuities. The traces of the deformations created by these structural factors are mentioned throughout this thesis. In Figure 7.9, a cross section was taken to test the stability in the regions where mass movements are concentrated, created by the heat map method. These cross-sections were used as a digital elevation model obtained by processing aerial photographs as described in the chapter in Chapter 7. After the 8 Digital Elevation Models created were superimposed, cross-sections were taken from the regions concentrated in the Heat Map and the topographical change that changed due to failure was tried to be observed Before taking sections from these regions, the accuracy and reality of this process was tried to be tested by

taking sections in the region (north of the study area) where the grading studies were carried out for the production activities of this quarry, which is located outside the study area in the same enterprise (Figure 7.10).As a result of the cross-sections taken in the production area, a difference was observed and the same method was applied for the regions in the heat map (Figure 7.11).

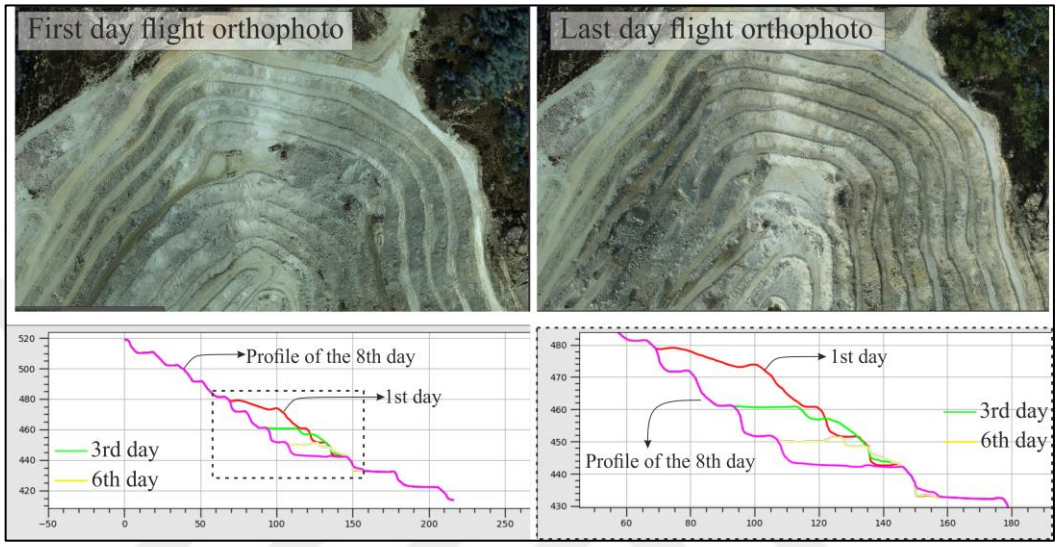

Figure 7.10 The difference seen in the region where the production and excavation activities continue, according to the topographic cross-sections taken from the DEM obtained from the flights on the first and last day

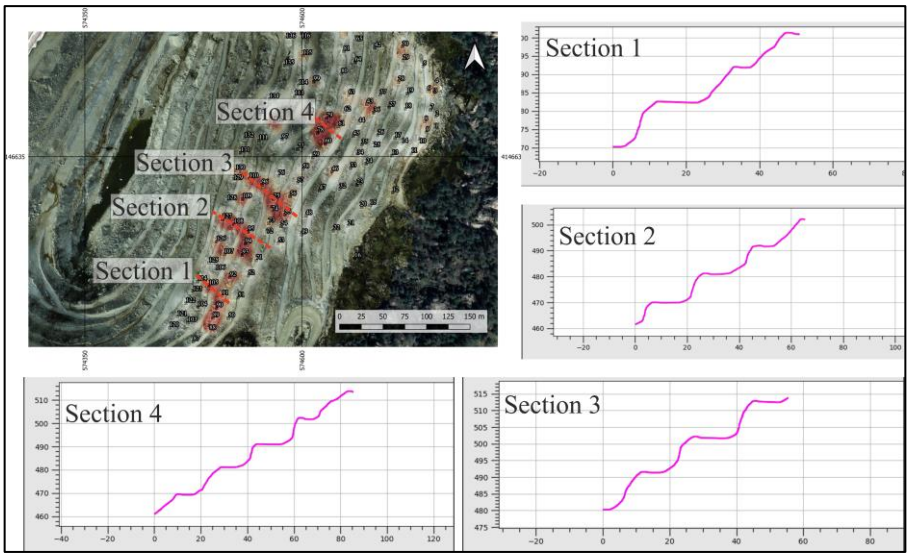

Figure 7.11 Topographical cross-sections taken from the regions where mass movements are concentrated by means of the Digital Elevation Model

As can be seen from a total of 4 cross-sections taken; No topographic changes (slopes) were observed in these regions due to failures (slidings).As the reason why the slope geometry did not change due to the slides despite the mass movements, which are numerous in these regions; Since the effect of water on failures is known, that is, the increase in the groundwater level during the rainy period and the saturation of the slopes, accelerating the failures (slidings) were mentioned in the relevant sections of this thesis. Since the study was carried out in the dry period, instability could not be determined from this point of view, since the groundwater level was low and did not affect the slides. Another factor is that, due to the cessation of production in this region where failures occurred, controlled blasting was not carried out and the lack of vibration (wave) caused by these blasting stopped slope failures in a controlled manner. Considering all these parameters, no significant (topographic change) change due to the slope geometry due to failures (slidings) was observed during the study period in the eastern part of the Open Albite Quarry (the problem area) and the slopes were considered stable in this respect.

If we take an overview of remote sensing studies; It can be said that this study constitutes another main subject of this study. The data obtained after the photogrammetric process of accurately and precisely positioned aerial photographs has proven that time can be saved in this study. It has been shown that remote sensing studies can be used to measure slope orientations in open pits with irregular slope geometry for various reasons and/or not to spend much time in dangerous areas where there are slidings such as slope failures, as used in this study. It has been considered as a very satisfactory way of reference in terms of study sustainability, not only in obtaining slope orientations, but also in obtaining the orientations of discontinuity planes in hard-to-reach places such as the slope top. On the other hand, these data (Digital Elevation Model, Textured Mesh Model and True Orthophoto) showed that its usability can be very useful for both visual evaluations and other analyzes.

CHAPTER NINE

CONCLUSIONS AND RECOMMENDATIONS

In this study, kinematic analysis technique was used for stability analysis in the eastern part of the Open Pit. Geological observations and analyzes made at 141 points showed that; The eastern part of the quarry predominantly faces potential toppling failures. Apart from toppling failures, wedge type sliding failures were determined as another dominant failure type. These discontinuities, which offer many different orientations at varying intervals in the study area, have been found to be effective in the formation of wedge blocks. The types of discontinuities that cause planar sliding failures are evaluated in two separate classes. These are included in the evaluation as foliation planes and joint sets of tectonic origin. Due to the metamorphic origin of the geological units in the study area, foliation planes played a major role in the occurrence of these planar slidings. At the same time, tectonic origin joint sets formed by the structural factors that are thought to control the open pit (the effects of which are seen) in and around the study area have been accepted as one of the other factors that make up this planar sliding mechanism. The dominant hazardous area in the eastern part of this open pit was determined by kinematic analysis, which is considered as the first step of slope stability assessments and is a type of analysis for determining potential mass movements in the field. While trying to create this area, only the orientation of the discontinuities and only the internal friction angle from the geomechanical properties of the rock material (shear stress) were used. In order to better examine these potential mass movements, to determine the effect of these mass movements on the open quarry and the damage it may cause, other parameters need to be included in the process. These parameters, in the context of environmental conditions; within the framework of weathering, alteration, groundwater condition and geomechanical (geotechnical) features; It should be calculated by adding the engineering properties of the rock material. The density map produced according to the results of the kinematic analysis made in the first step for stability evaluations in the eastern part of the open pit helped to narrow the study area of influence. Other types of stability methods have been proposed for stability assessments at these identified points. These methods, on the other hand, can be defined as a method that is generally referred to as numerical analysis and takes into account many parameters. In regions where mass

movements are concentrated, on a bench scale; (each stage separately) Limit-Equilibrium Analysis and in general slope scale; (along a line that includes many different stages) numerical modeling and analysis with the Finite Element Method, it is suggested to obtain a numerical result and calculate the safety factor.

If we look at the results within the framework of remote sensing in this study, it has been seen that the use of photogrammetry technique is very useful and effective. The efficiency of the work has been increased with raster and vector geographic data that are produced (produced) as a result of photogrammetric processes. The fact that the created datasets have an accelerating effect on the progress of the study has been proven. Namely; Thanks to the dense point cloud data created, some data that could not be obtained in the field were obtained. In the work of measuring the discontinuity trends at the observation points within the scope of the thesis in the study area, even if the observation point is not located, measurements were made in areas that are difficult to reach or dangerous, thanks to the plugin in the Cloud Compare program. In this way, the research efficiency (research diameter) has increased and the areas that cannot be measured are not bypassed. Apart from the point cloud data, the topographic change (distortion of the land geometry) due to the failures in the land was examined with the Digital Elevation Model with 0.15 m grid cell size. As a result of the investigations, no significant geometry changes or deterioration was observed. The reason of this; can be shown as keeping the working time and interval short. It is certain that if this study is carried out for shorter periods but for longer periods (summer and winter periods), different results will be obtained. In other words, invisible and/or unnoticeable changes can be examined with transverse topographic sections taken from digital elevation models obtained by drone flights in the field with short periods over a longer period of time. In case of a difference, detailed geological examination and geotechnical analysis can be applied to that region. The results can be compared with other methods and solutions offered by the company for monitoring, and studies can be initiated to use them more effectively. Apart from these, other data produced were used for purposes such as visualization. For example, these data types, which serve different purposes such as the textured mesh model to visually examine the work area in detail, and the use of orthophotos for the map base, contributed to the study in all respects. If we draw a summary conclusion from all these told; Based on the above-mentioned explanations

in the study area (to implement these explanations), it has been suggested to fly using UAVs at regular intervals.

REFERENCES

3D Survey, *Photogrammetry Software v2.11.3. Modri Planet d. o. o., Student Licence,* (2020). /3dsurvey.si [Computer Software]

Aksoy, H., & Ercanoglu, M. (2007). Fuzzified kinematic analysis of discontinuity-controlled rock slope instabilities. *Engineering Geology*, *89*(3-4), 206–219.

Barton, N., & Choubey, V., (1977). The shear strength of rock joints in theory and practice. *Rock Mechanisc, 10,* 1-54.

Bawa, H., Yendaw, J., Kansake, B., & Bansah, K. (2017). Rock mass characterization for open pit slope design using kinematic analysis. *51st US Rock Mechanics/Geomechanics Symposium* At: San Francisco, California, USA.

Candan, O., Çetinkaplan, M., Oberhansli, R., Rimmele, G., & Akal, C., (2005). Alpine high-pressure/ low temperature metamorphism of Afyon Zone and implication for metamorphic evolution of western Anatolia, Turkey. *Lithos, 84,* 102-124.

Cloud Compare, *v2.11.2, 3D Point Cloud Viewing and Processing Software,* (2020). /danielgm.net/cc. [Computer Software]

Çelik, M., Yakar, İ., Hamal, S., Oğuz, G., & Kanun, E. (2020). Sfm tekniği ile oluşturulan 3D modellerin kültürel mirasin belgelenmesi çalişmalarinda kullanilmasi: gözne kalesi örneği. *Türkiye İnsansız Hava Araçları Dergisi*, *2* (1), 22-27.

Dips V 7.016, (2019). Graphical and Statistical Analysis of Orientation Data, RocScience Inc.

Eberhardt, E.D., (2003). Rock slope stability analysis– utilization of advanced numerical techniques. *Earth and Ocean sciences at UBC,*1-41.

Francioni, M., Salvini, R., Stead, D., Giovannini, R., Riccucci, S., Vanneschi, C., & Gullì, D. (2015). An integrated remote sensing-GIS approach for the analysis of an open pit in the Carrara marble district, Italy: Slope stability assessment through kinematic and numerical methods. *Computers and Geotechnics*, (67), 46–63.

Goodman, R. E., & Bray, J. (1976) Toppling of rock slopes. ASCE, *Proc. Specialty Conf. on Rock Eng. for Foundations and Slopes, Boulde*r, (CO, 2), 201-34.

Gürocak, Z., Alemdag, S., & Zaman, M. M., (2008). Rock slope stability and excavatability assessment of rocks at the Kapıkaya Dam site, Turkey. *Engineering Geology*, (96), 17–27.

Hoek, E., (1999). Putting numbers to geology – an engineer's viewpoint. *Quarterly Journal of Engineering Geology*, (32), 1-19.

Hoek, E., & Bray, J.W., (1981). *Rock Slope Engineering*. (3rd Edition). London: Institute of Mining and Metallurgy.

Hudson, J.A., & Harrison, J.P., (1997). *Engineering Rock Mechanics - An Introduction to the Principles* (2nd Edition). London: Pergamon Press.

Kadakçı, Koca. T., & Koca, M. Y., (2014). Açık ocak albit işletmesindeki kaya şevlerinin sonlu elemanlar yöntemi kullanilarak duraylilik değerlendirmesi. *Jeoloji Mühendisliği Dergisi*, *38* (1), 1-18.

Karagöz, S., & Koca, M. Y., (2016). Alipaşa açık ocak albit madeninde meydana gelen heyelanin gps kullanilarak izlenmesi ve oluşum nedenleri. *Jeoloji Mühendisliği Dergisi*, *40* (1), 27-52.

Kentli, B., & Topal, T., (2004). Assessment of rock slope stability for a segment of the Ankara–Pozantı motorway, Turkey. *Engineering Geology*, (74), 73–90.

Kıncal, C. (2021). Fault-controlling safe slope design procedure in an open-pit mine case study: Tunçbilek-Kütahya (Turkey) coal field. *Arabian Journal Geoscience* (14), 91.

Koca, M. Y., Kıncal, C., & Kadakçı, Koca. T., (2020). Slope stability evaluation report of the eastern slopes of sarıkısık open pit albite mine. Dokuz Eylul University, Izmir.

MTA Emre, Ö., Duman, T.Y., Özalp, S., Elmacı, H., Olgun, Ş., & Şaroğlu, F. (2013). Açıklamalı Türkiye Diri Fay Haritası. Ölçek 1:1.250.000, *Maden Tetkik ve Arama Genel Müdürlüğü, Özel Yayın Serisi-30*, Ankara-Türkiye. ISBN: 978-605-5310-56-1

Norrich, N., & Wyllie, D., (1996) Rock slope stability analysis. In: Landslides: investigation and mitigation, Transportation Research Board Special Report, *National Research Council*, Washington, 391–425.

Obregon, C., & Mitri, H. (2019). Probabilistic approach for open pit bench slope stability analysis – A mine case study. *International Journal of Mining Science and Technology*. *29*(4), 629-640.

Pantalidis, L., (2009). Rock slope stability assessment through rock mass classification systems. *International Journal of Rock Mechanics and Mining Sciences*, (46), 315–325.

Park, H., & West, T.R., (2001). Development of a probabilistic approach for rock wedge failure. *Engineering Geology* (59), 233–251.

Park, H.-J., Lee, J.-H., Kim, K.-M., & Um, J.-G. (2015). Assessment of rock slope stability using GIS-based probabilistic kinematic analysis. *Engineering Geology*, (203), 56–69.

QuantumGIS, *Open-Source Codes Geographic Information Systems Software, QGIS V 3.10.13,* (2020) *./*qgis.org. [Computer Software]

Şengör, A.M.C., (1987). Cross-faults and differential stretching of hanging walls in regions of low-angle normal faulting: examples from western Turkey. In: Coward, M.P., Dewey, J.F. & Hancock, P.L. (Eds), Continental Extensional Tectonics. *Geological Society of London*, Special Publication (28), 575–589.

Tanyaş, H., (2011). alipaşa (Çine-Aydın) *işletmesinde süreksizlik denetimli şev duraysizliklarinin kinematik, analitik ve sayisal çözümleme teknikleriyle incelenmesi*, Yüksek Lisans Tezi. Hacettepe Üniversitesi, Ankara.

Ulusay, R., Gökçeoğlu, C., Sönmez, H., & Tuncay, E., (2001). Causes, mechanism and environmental impacts of instabilities at Himmetoğlu coal mine and possible remedial measures. *Environmental Geology, 40* (6), 769–786.

Uygun, A., & Gümüşçü, A., (2000). Geology and origin of the albite deposite of the çine submassif, southern menderes massif (SW-Turkey). *Bulletin of the Mineral Research and Exploration,* (122), 23-30.

Wyllie, D.C., & Mah, C.W., (2004). *Rock slope engineering civil and mining*. (4th edition). New York: *Spon Press*.

APPENDICES

APPENDIX-1: UCS Values

Table 1A.1 Values from discontinuity surfaces

Location	Rebound Value										Total	Average
1	24	25	28	27	24	33	28	28	29	18	264	26.4
2	23	40	34	32	34	39	38	34	45	44	363	36.3
3	48	56	30	32	25	51	48	34	28	52	404	40.4
4	25	20	12	16	18	19	20	14	12	15	171	17.1
5	19	15	11	12	14	12	12	18	10	14	137	13.7
6	40	34	41	26	28	32	24	35	16	22	298	29.8
7	18	19	14	22	32	19	24	19	21	11	199	19.9
8	12	10	14	34	16	28	11	13	10	23	171	17.1
9	38	35	28	37	27	32	25	28	30	23	303	30.3
10	27	28	24	24	28	18	18	11	32	34	244	24.4
11	11	21	15	25	23	26	14	18	15	10	178	17.8
12	22	17	24	10	22	15	14	30	40	15	209	20.9
13	19	10	15	20	16	11	22	18	11	15	157	15.7
14	15	31	22	21	28	26	15	44	30	34	266	26.6
15	20	21	23	21	30	12	20	18	21	13	199	19.9
16	17	11	13	19	25	18	14	21	17	25	180	18
17	15	28	35	28	25	36	18	26	46	40	297	29.7
18	30	22	34	24	21	18	40	32	34	28	283	28.3
19	19	28	22	20	15	24	18	30	34	15	225	22.5
20	15	26	29	48	40	40	19	38	30	15	300	30
21	23	28	24	20	22	15	30	28	15	18	223	22.3
22	18	21	12	11	24	13	20	18	13	11	161	16.1
23	29	31	38	28	40	29	25	30	30	33	313	31.3
24	22	28	31	20	24	22	25	28	28	20	248	24.8
25	30	27	24	33	25	21	31	30	27	26	274	27.4
26	28	25	30	31	38	31	34	28	22	33	300	30
27	24	22	32	27	23	24	30	27	24	25	258	25.8
28	34	30	31	33	40	37	31	27	28	32	323	32.3
29	38	40	34	39	36	28	27	42	37	39	360	36
30	13	19	20	27	24	11	21	27	19	21	202	20.2
31	12	16	21	24	16	19	22	21	18	23	192	19.2
32	28	22	24	21	26	20	23	25	28	31	248	24.8
33	24	28	23	22	44	32	29	32	22	30	286	28.6
34	39	32	25	23	30	24	26	27	34	28	288	28.8
35	28	42	27	42	41	27	28	44	44	38	361	36.1
36	22	20	33	26	42	29	23	48	39	36	318	31.8
37	25	39	30	26	38	44	29	41	32	29	333	33.3

Table 1A.1 Continues

39	31	42	26	30	28	36	25	38	25	43	324	32.4
40	29	31	44	48	39	34	34	45	39	27	370	37
41	33	32	30	33	32	31	28	34	29	31	313	31.3
42	32	33	28	37	31	28	27	41	33	27	317	31.7
43	34	20	25	16	18	24	22	20	29	26	234	23.4
44	28	37	31	31	24	38	34	38	28	33	322	32.2
45	40	46	32	30	35	35	34	31	36	39	358	35.8
46	23	26	29	31	35	25	24	28	36	34	291	29.1
48	28	34	24	40	31	27	25	40	28	33	310	31
49	20	22	19	21	18	19	21	24	20	25	209	20.9
50	34	35	31	39	28	30	38	33	36	29	333	33.3
51	25	27	24	27	22	18	14	25	26	23	231	23.1
52	24	18	19	17	19	21	16	19	20	21	194	19.4
53	12	11	14	11	14	13	12	14	14	16	131	13.1
54	12	20	16	15	24	20	23	19	25	17	191	19.1
55	14	11	10	10	12	10	12	12	13	10	114	11.4
56	10	13	10	18	14	13	12	20	11	12	133	13.3
57	24	28	26	18	20	24	18	20	24	20	222	22.2
58	18	14	16	18	14	16	14	17	18	25	170	17
59	16	26	18	44	22	18	20	16	36	28	244	24.4
60	39	41	46	26	32	39	43	24	28	35	353	35.3
61	30	31	36	33	22	23	26	30	32	21	284	28.4
62	41	28	31	27	28	34	50	24	40	41	344	34.4
63	37	38	42	42	38	37	45	38	41	38	396	39.6
64	17	16	14	20	11	17	16	11	16	13	151	15.1
65	20	25	18	15	18	27	29	25	33	21	231	23.1
66	14	18	12	12	20	21	21	13	14	14	159	15.9
67	30	40	24	33	27	40	18	21	16	24	273	27.3
68	50	47	41	40	38	36	44	41	42	40	419	41.9
69	12	21	18	16	25	19	12	22	17	15	177	17.7
70	20	19	12	17	12	14	21	18	16	18	167	16.7
71	37	33	30	48	35	30	43	37	41	47	381	38.1
72	36	24	30	26	24	24	26	21	20	20	251	25.1
73	17	19	21	22	12	24	16	25	17	20	193	19.3
74	30	37	29	27	30	37	35	27	38	33	323	32.3
75	19	27	25	22	19	20	28	27	22	18	227	22.7
78	28	35	33	35	36	22	30	35	33	29	316	31.6
79	29	31	27	36	41	44	27	30	33	41	339	33.9
80	33	29	28	31	27	34	22	25	34	32	295	29.5
81	26	19	18	12	17	20	16	16	14	21	179	17.9
82	24	26	30	26	31	28	27	25	21	27	265	26.5

Table 1A.1 Continues

83	39	33	29	45	37	40	42	37	40	29	371	37.1
84	18	17	22	12	20	17	19	18	13	16	172	17.2
85	22	24	31	24	30	20	33	28	30	33	275	27.5
86	12	20	28	17	23	21	20	22	15	17	195	19.5
87	12	24	20	18	24	21	13	17	15	15	179	17.9
88	20	19	14	20	16	14	12	11	20	17	163	16.3
89	14	11	12	14	13	11	16	15	14	11	131	13.1
90	28	25	20	18	16	14	23	27	20	25	216	21.6
91	27	25	17	32	17	26	20	19	20	23	226	22.6
92	21	27	25	30	31	20	20	29	30	32	265	26.5
93	22	19	26	28	20	24	24	19	21	20	223	22.3
94	40	37	41	35	31	45	40	40	47	37	393	39.3
95	35	30	40	44	45	25	27	35	30	32	343	34.3
96	28	34	26	20	29	27	31	30	32	31	288	28.8
97	32	40	41	40	39	44	47	35	41	42	401	40.1
98	27	30	25	32	34	41	40	37	38	28	332	33.2
99	40	39	38	35	28	27	30	27	33	25	322	32.2
100	30	25	24	22	27	23	29	31	32	25	268	26.8
101	20	22	19	10	14	11	12	17	18	13	156	15.6
102	15	20	17	19	18	15	19	17	14	16	170	17
103	22	30	25	28	32	31	22	26	28	26	270	27
104	26	24	30	27	24	20	27	26	30	27	261	26.1
105	23	31	21	25	28	29	33	29	35	25	279	27.9
106	20	22	25	27	26	22	29	22	24	27	244	24.4
107	29	25	38	26	21	35	28	37	27	29	295	29.5
108	32	28	29	30	27	35	33	28	29	22	293	29.3
109	34	35	34	35	22	24	20	19	21	26	270	27
110	24	28	30	22	23	25	24	37	27	29	269	26.9
111	40	39	44	46	36	40	34	35	45	40	399	39.9
112	34	40	38	29	31	27	25	36	30	37	327	32.7
113	37	30	40	35	36	42	28	32	36	35	351	35.1
114	35	41	40	39	35	39	38	22	34	44	367	36.7
115	30	30	38	30	31	40	31	28	25	25	308	30.8
116	24	26	28	27	22	28	30	25	22	24	256	25.6
117	34	30	32	27	23	35	40	43	27	25	316	31.6
118	30	27	29	20	35	23	32	34	27	35	292	29.2
119	28	23	30	20	20	35	20	32	33	21	262	26.2

APPENDIX-2: Wedge Factor

Table 2A.1 Wedge and Factor of Safety Values of Wedge Sliding

Location	Wedge F.	FS	ß	ε/2	Ø	Ψ	X	Y
8	2.607824	1.771499	75	21.74	23	32	574741	4146675
18	0.187286	0.170484	10	68	23	25	574718.7	4146690
20	1.074889	0.702584	35	32.25	23	33	574668.6	4146577
25	0.213897	0.15726	9	47	23	30	574682.7	4146651
28	1.640516	1.072297	59	31.5	23	33	574710.6	4146721
29	1.148532	0.602041	45	38	23	39	574716	4146746
30	3.826102	3.187444	82	15	23	27	574715.3	4146762
31	1.304242	1.135085	39	28.85	23	26	574700.5	4146838
32	2.836955	1.85433	76	20	23	33	574643.2	4146598
33	0.185483	0.154522	9	57.5	23	27	574655.6	4146622
34	1.359377	0.484178	50	34.3	23	50	574663.5	4146639
36	1.030027	0.521059	39	37.66	23	40	574682.4	4146686
37	0.264311	0.23003	13	58.33	23	26	574689.7	4146706
38	2.292869	2.087174	66	23.48	23	25	574571.6	4147002
39	0.732884	0.234424	33	48	23	53	574660.7	4146871
41	0.255974	0.173884	12	54.315	23	32	574670.9	4146842
43	0.742964	0.326575	32	45.5	23	44	574674.4	4146695
44	2.764511	0.572337	71	20	23	64	574665	4146673
46	0.966677	0.682904	35	36.395	23	31	574634.4	4146618
48	0.059274	0.043579	3	62	23	30	574604.4	4146567
49	0.648871	0.379096	26	42.5	23	36	574599.3	4146545
51	4.355485	3.335312	59	11.35	23	29	574526.4	4146472
52	0.7528	0.408998	30	41.62	23	38	574538.1	4146498
53	0.53555	0.393743	20	39.69	23	30	574572.5	4146535
55	0.047719	0.045495	2	47	23	24	574580.1	4146568
56	0.333001	0.303128	12	38.635	23	25	574586.1	4146589
57	1.320967	1.259392	35	25.735	23	24	574594.5	4146605
59	2.213089	1.341603	56	22	23	35	574612.5	4146634
60	0.52521	0.306849	22	45.5	23	36	574626.8	4146650
61	1.392379	0.301145	53	35	23	63	574641.8	4146670
63	0.201294	0.136739	9	51	23	32	574653.4	4146706
68	0.684732	0.334356	28	43.285	23	41	574637.7	4146855
70	0.036494	0.026831	2	73	23	30	574627.7	4146934
73	0.075781	0.065952	4	67	23	26	574561.4	4146558
74	0.282234	0.124058	14	59	23	44	574565.2	4146578
75	1.466357	0.388939	53	33	23	58	574567.2	4146586
78	1.521522	0.602263	50	30.23	23	47	574617.7	4146662
79	1.580093	0.67071	50	29	23	45	574628.1	4146680

Table 2A.1 Continues

81	1.619052	0.879636	77	37	23	38	574647.8	4146756
82	0.057746	0.03027	3	65	23	39	574647.4	4146780
83	0.646311	0.475176	24	39	23	30	574634	4146829
85	0.111237	0.075563	6	70	23	32	574620.8	4146871
88	0.407655	0.199059	19	53	23	41	574493.4	4146441
89	0.217431	0.228436	10	53	23	22	574497.4	4146449
90	0.757137	0.289377	33	46	23	48	574501.5	4146461
91	9.421431	4.766014	80	6	23	40	574508	4146475
92	0.336491	0.069664	16	55	23	64	574517	4146496
93	0.235853	0.148425	11	54	23	34	574531.2	4146522
94	0.201294	0.160697	9	51	23	28	574534.7	4146535
95	0.315807	0.263092	14	50	23	27	574537.8	4146549
96	0.093507	0.085119	4	48.245	23	25	574554	4146603
97	3.548676	1.506323	102	16	23	45	574576.7	4146655
98	0.389868	0.177465	20	61.315	23	43	574606.1	4146685
99	0.610904	0.259314	27	48	23	45	574613.3	4146721
102	1.036356	0.563055	37	35.5	23	38	574604.8	4146851
103	0.529774	0.29842	22	45	23	37	574468.4	4146444
105	1.361166	0.520236	47	32.5	23	48	574492.7	4146486
107	0.123257	0.112199	5	45	23	25	574510.3	4146522
108	1.43868	0.702511	46	30	23	41	574521.8	4146557
109	2.710904	1.277994	68	20	23	42	574531.3	4146586
110	0.568689	0.258864	25	48	23	43	574539.1	4146610
112	1.067885	0.929383	29	27	23	26	574568.1	4146675
115	0.43227	0.159503	21	56	23	49	574601	4146751
117	0.375934	0.183569	19	60	23	41	574596.5	4146788
119	0.935423	0.357517	38	41.16	23	48	574596.2	4146816
122	2.07484	0.912009	64	25.67	23	44	574464	4146468
125	0.784267	0.241867	35	47	23	54	574486	4146516
126	0.218162	0.092604	11	61	23	45	574487	4146540
127	2.231323	2.231323	78	26	23	23	574500	4146567
130	0.575212	0.312515	24	45	23	38	574518	4146622
134	1.889733	1.508613	53	25	23	28	574560	4146707
138	1.414214	0.690564	45	30	23	41	574574	4146826
140	0.092178	0.05008	5	71	23	38	574566	4146882